Monocrystalline Halide Perovskite Nanostructures

for Optoelectronic Applications

Cover image: Collage of Persian miniature illustrations and optical image of $CH_3NH_3PbBr_3$ single crystals. Designed by Taraneh Khorram.

Ph.D. Thesis, University of Amsterdam, April 2018
Monocrystalline Halide Perovskite Nanostructures for Optoelectronic Applications
Parisa Khoram

ISBN: 978-94-92323-18-7

A digital version of this thesis can be downloaded from http://www.amolf.nl

Monocrystalline Halide Perovskite Nanostructures

for Optoelectronic Applications

ACADEMISCH PROEFSCHRIFT

ter verkrijging van de graad van doctor
aan de Universiteit van Amsterdam
op gezag van de Rector Magnificus
prof. dr. ir. K.I.J. Maex
ten overstaan van een door het College voor Promoties ingestelde commissie,
in het openbaar te verdedigen in de Agnietenkapel
op woensdag 25 april 2018, te 12.00 uur

door

Parisa Khoram

geboren te Mashhad, Iran

Promotiecommissie

Promotor:	prof. dr. E. C. Garnett	Universiteit van Amsterdam
Copromotor:	prof. dr. A. Polman	Universiteit van Amsterdam

Overige leden:	prof. dr. D. Cahen	Weizmann Institute of Science
	prof. dr. M. A. Loi	Rijksuniversiteit Groningen
	prof. dr. J. N. H. Reek	Universiteit van Amsterdam
	prof. dr. W. C. Sinke	Universiteit van Amsterdam
	prof. dr. T. Gregorkiewicz	Universiteit van Amsterdam

Faculteit der Natuurwetenschappen, Wiskunde en Informatica

The work described in this thesis was performed at
AMOLF, Science Park 104, 1098 XG Amsterdam, The Netherlands.

This work is part of the research programme of the Netherlands Organisation for Scientific Research (NWO). It is also funded by the European Research Council (ERC).

There was the door to which I found no key
There was the veil through which I might not see:
Some little talk awhile of me and thee
There was - and then no more of thee and me

Omar Khayyam (1048-1131),
Persian philosopher, mathematician and poet

Contents

1

Introduction

The social and technological development of today's modern society is not imaginable without optoelectronic devices- the electronic devices that convert, emit, detect or control light. Our every day lives are surrounded by light emitting diodes (LEDs), laser-based telecommunication systems, high mobility transistors, and photovoltaics. The ambitious goal of controlling the ever growing energy consumption while proceeding with high-technology life is only possible with developing new designs and materials for low-cost and efficient optoelectronics. The incorporation of nanotechnology and nanomaterials into these devices opens up additional and unique opportunities for approaching highly efficient devices.
Less than a decade ago, halide perovskites were only a class of ionic crystals among many others, with interesting properties, but not much speculation about their applications. Their initial success in delivering high efficiencies in solar cells brought them to the forefront of optoelectronics research recently. Besides the promise for a new generation of efficient photovoltaics and light emitting devices, their complex system has intrigued the curiosity of many scientists. Studying perovskites in their fundamental details can also potentially initiate the discovery of devices with new designs and applications. In this thesis we attempt to contribute to unravelling the unknown aspects of halide perovskites towards their optoelectronic application by fabricating and characterizing mono-crystalline perovskite nanostructures. We start this chapter by giving a historical background and introducing the chemical structure of perovskites. Afterwards we discuss the special optical properties that their ionic nature bring to them. We explain then the charge carrier generation and

recombinstion in halide perovskites and continue with reviewing the advances of perovskites in optoelectronics. Next we go through perovskite nanostructures and single crystals and their incorporation into devices. Subsequently we finish this chapter by providing an outline of the following chapters in this thesis.

1.1 Brief history and crystal structure of perovskites

In 1839, Gustav Rose discovered $CaTiO_3$ mineral in Ural mountains of Russia and named it Perovskite after the mineralogist Lev Perovski [1]. This discovery opened up a new category of materials all with the same crystal structure as $CaTiO_3$, known as the perovskite structure [2]. These materials with the stoichiometric formula of ABX_3 all consist of three ions: A and B cations and X anions. The perovskite structure can be represented in many different ways. Figure 1.1a shows a usual ball-and-stick model showing the unit cell of the perovskite, where A atom is in the center of a cubic unit with B atoms in the 8 corners and X atoms in the middle of each edge. Another common way to show the unit cell of the perovskite structure is with X anions octahedrally coordinated around the B cation, with A cations in the corners of the unit cell as shown in Figure 1.1b. Sometimes the 3-dimensional structure is pictured with corner-sharing BX_6 octahedra network with A ions sitting in cuboctrahedral cavities. The nature of A cations including its polarity, charge and size,[3] and also their interaction with the inorganic framework [4] defines the tilting and rotating of the BX_6 in the lattice and creates cubic, tetragonal or orthorhombic phases(Figure 1.1c-d). A certain perovskite goes through phase transition by external parameters such as temperature, pressure and magnetic and electric fields which control these tilts and rotations. A wide range of ions (elements and compounds) can mix and form perovskite structures, as long as the charge balancing is maintained and the sizes of ions can preserve the perovskite structure. Goldschmidt tolerance factor [5] and the octahedral factor [6] are commonly used to predict the probable formation and crystal structure of perovskites based on the ionic radii and the ideal distances between ions. Goldschmidt factor (t) is given by the equation below:

$$t = \frac{r_A + r_X}{\sqrt{2}(r_B + r_X)} \tag{1.1}$$

where r_i is the ionic radius of A, B or X. The octahedral factor μ is given by the ionic radii of B and X in BX_6 octahedra as follow [7]:

$$\mu = \frac{r_B}{r_X} \tag{1.2}$$

The t and μ values should lie between $0.75 - 1.0$ and $0.42 - 0.8$ respectively for the

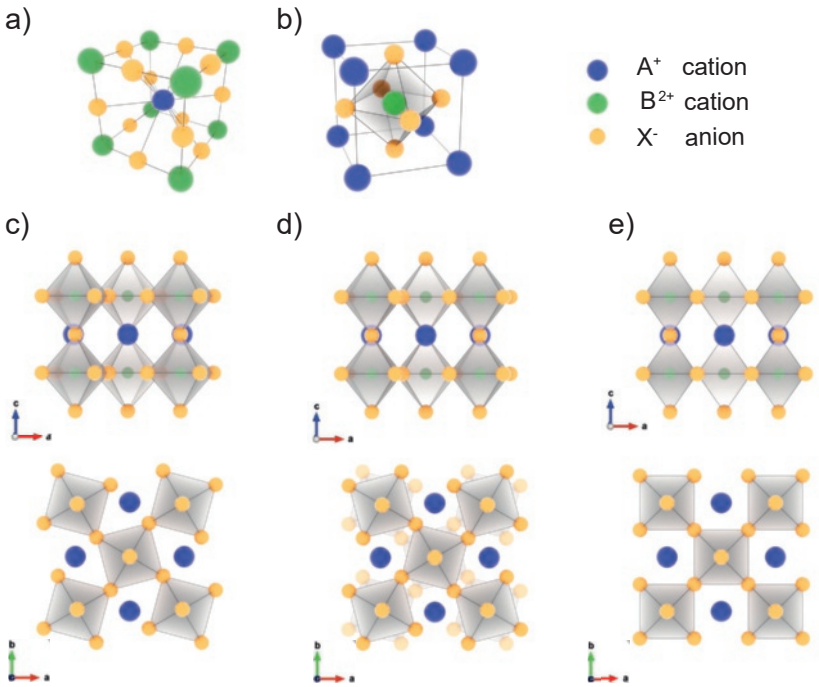

Figure 1.1: Schematic of various representation of perovskite crystal structure. **a)** The unit cell of perovskite structure, where A atom is in the center of the unit cell with B atoms in 8 corners and X atoms in the middle of edges **b)** The perovskite unit cell with BX_6 octahedron in the center and A atoms in the corners of the unit cell. **c)**, **d)** and **e)** show corner-sharing BX_6 octahedra networks of perovskite structures with orthorhombic, tetragonal and cubic structure, respectively. With increasing the temperature the phase transition occurs from orthorhombic to tetragonal and cubic. The middle row is the ac-plane and the bottom row is the ab-plane.

formation of oxide perovskite structures [7].

Nowadays, the term *perovskite* is not only attributed to $CaTiO_3$, but is a general name for any ABX_3 material with perovskite structure. Many other minerals such as $SrTiO_3$ and $LaCoO_3$ are in the same category [8]. Halide perovskites are similar to oxide perovskite but the oxygen is substituted with a halogen, such as chlorine, bromine or iodine and the valence of the cations is adjusted to maintain charge neutrality. This class of perovskites was first studied at the end of the nineteenth century by Wells [9]. When a halogen replaces oxygen in the X site, the oxidation state of A and B cations must sum to 3, therefore monovalent A and divalent B ions are required. Both tolerance factor and octahedral factor can also be used to predict the formation of ABX_3 halide perovskites with 96% predicting accuracy [10]. The octahedral factor has a lower limit, and both factors have to be satisfied but they

are not sufficient for the formation of perovskite structure [7, 10].
Almost a hundred years after the early demonstration of inorganic halide perovskites, Weber replaced the A ion with an organic cation and introduced methylammonium lead halides with the chemical formula $CH_3NH_3PbX_3$ (X=Cl, I or Br) as the first hybrid halide perovskites [11, 12]. To predict the perovskite formation with the geometrical factors , the effective radius of the organic cation is considered as a rigid sphere model. For the formation of halide perovskites $0.81 < t < 1.1$ and $0.44 < \mu < 0.90$ should be satisfied. Studies showed that the cubic structure of hybrid halide perovskite is realized when $0.85 < t < 1.0$ [13]. $CH_3NH_3PbI_3$ as the most common hybrid perovskites used in optoelectronics has a lower t of 0.83 and therefore the less symmetric tetragonal crystal structure at room temperature. When iodide is replaced with the smaller bromide or chloride ions, the t factor falls in the right range for a cubic structure. In general, all $CH_3NH_3PbX_3$ perovskites have a cubic structure at higher temperature, and transform to tetragonal and orthorhombic structures subsequently by lowering the temperature.
Due to the larger ionic radii of halide ions in comparison to the oxides, only a limited range of divalent cations can maintain the perovskite structure in this system including the alkaline earths, rare earth and group 14 elements such as Pb^{2+} and Sn^{2+} ions. The charge distribution of the A cation also plays an important role in stabilizing the hybrid halide perovskite structure. In addition to methylammonium, formamidinium ($H_2NCHNH_2{}^+$) and mixtures of organic and inorgaic cations ($CH_3NH_3{}^+$,$H_2NCHNH_2{}^+$ and Cs^+) are among those which form stable and efficient hybrid perovskite systems for optoelectronics [14].
The fabrication and semiconducting properties of layered and 3-D halide perovskites were first studied in the 1990s by Mitzi et al [15–18]. However, not much attention was paid to the application of materials in optoelectronic devices until recently. In 2009, Miyasaka's group [19] applied hybrid halide nanocrystals as visible-light sensitizers in a liquid electrolyte based dye sensitized solar cell (DSSC). In this early demonstration the efficiency was as low as 4%, although this was just the starting point of the rapid development of halide perovskites-based devices. Within only 8 years, the PCE of perovskite solar cells has increased to values comparable to those of silicon solar cells, the most common photovoltaic technology [20]. Although halide perovskites were considered primarily to replace the dye molecules and organic absorbers in DSSCs, nowadays perovskite solar cells stand out as an independent type of solar cell with a planar thin film architecture.
The rapidly increasing PCE of perovskite solar cells drew the attention of numerous research groups worldwide to halide perovskites as the active component of other optoelectronic devices as well during the last 8 years. In addition to tremendous efforts in increasing the device performance [21–27], many research groups used

this class of material for scientific explorations and focused on unraveling the intrinsic properties and understanding the working mechanisms of halide perovskite in devices and their interaction with light. [14, 28–32].The evolution of perovskite solar cells and optoelectronics is discussed in detail in Section 1.4.

1.2 The ionic nature of halide perovskites

Perovskites are ionic solids and their chemical bonds are formed based on electrostatic forces between the oppositely charged ions. This characteristic makes halide perovskites fundamentally different than conventional inorganic semiconductors with covalent bonds. In covalent solids, such as those formed from elements of group 14 like Si and Ge, the shared electrons construct the bonds which keep the counterparts of the solid together. The interactions of electrons with each other and the neighboring atoms in the solid, defines many physical properties of the solid such as hardness, melting and boiling points, solubility, and conductivity [33]. We should note that often the bonds in solids have a complex nature of mixed binding types, for instance TiO_2 has ionic/metallic bonds. But it is common to ignore this in discussion of the solid structures for simplicity and only consider the dominant bond type [34]. Here we also take this assumption for the further discussion of bonds and their effect on electronic structure in halide perovskites.
Electrons in solids have discrete ranges of energies, similar to electrons in isolated atoms with specific available orbitals. When atoms are brought together to form solids, the electrons feel the nuclei and electrons of neighboring atoms as well, which cause the overall wave functions of electrons to be altered. In formation of ionic solids electrons are exchanged between positive and negative ions in order to make the outer orbital of ions full with the electronic structure of inert gases. For example in the simplest and well-known case of NaCl, Na with electron configuration of $[Ne]3s^1$ gives away its valance electron to the Cl with electron configuration of $[Ne]3s^2 3p^5$. This way Na^+ and Cl^- ions with electron configuration of inert gases (Ne and Ar) are formed and the coulombic attraction of ions hold them together in the lattice [33]. In most ionic structures, electrons are tightly bound to each atom and are not free to contribute to the current flow. In fact, ionic solids are mostly insulators. In the band structure of ionic solids which comes from the participation of valance electrons, the energy difference between the valance band and conduction band is usually as high as 3 eV or more. Surprisingly that is not the case in the electronic structure of halide perovskite solids. In the halide perovskites, as the most relevant perovskites for optoelectronics, the valance band maxima (VBM) form as the result of σ-antibonding of the metal outer s orbitals (Pb $6s$ or Sn $5s$) with halide outer p orbitals. Conduction band minima (CBM) mostly comes from the σ-antibonding of metallic ion p orbitals (Pb $6p$ or Sn $5p$) with a small contribution

of halide outer p orbitals ($5p$ for I, $4p$ for Br and $3p$ for Cl). The formation of CBM bands dominantly from metallic p orbitals gives halide perovskites a unique dual ionic and covalent nature. The energy gap of such electronic configuration is less than 3 eV, classifying halide perovskites as semiconducting materials.[35, 36]
The electronic band structure of halide perovskites gives them distinct characteristics from conventional semiconductors and brings them special properties. Density functional theory (DFT) calculations of $CH_3NH_3PbI_3$ and mixed halide perovskites [37], along with earlier first-principle pseudopotential calculations of the electronic band structure of $CH_3NH_3PbX_3$ and $CsPbX_3$ [36] indicate that the band structure near the VBM and CBM is mainly formed from the $[PbX_6]^{-4}$ inorganic framework, with organic cations playing a minor role. These findings were consistent with later experimental evidence of the band structure from UV-Vis spectroscopy in halide perovskites [38]. Filip et al [39] showed by DFT calculations that the the bonding and antibondig bands of the A cation are located away from the band edges, as shown in Figure 1.2a. They indicated that removing the cation while compensating the charges by a positive background, and keeping the arrangement of octahedral network (bond length and tilt) the same, does not change the band structure around the band edge significantly.
Formation of the band gap from the contribution of the different ions in perovskite semiconductors gives an interesting feature to these materials: the possibility to tune the optical properties via changing the ionic components. The energy and structure of perovskites' band gap can be tuned by substitution of different ions in each A,B and X sites and even making a combination of different ions with varied ratios in each site. Since the early development of hybrid perovskite photovoltaics, many researchers mixed halide ions (Cl, Br, and I) to obtain a range of band gap energies from 3.11 eV in ultra-violet (from $CH_3NH_3PbCl_3$) to 2.23 eV in visible ($CH_3NH_3PbBr_3$) and 1.55 eV in infrared ($CH_3NH_3PbI_3$) [41–48] (see Figure 1.2a). The increase of band gap with reducing the halide ionic size has been used as a general trend also in other halide perovskites, such as $CsPbX_3$ [49–51], $CH_3NH_3SnX_3$ [52, 53] and H_2NCHNH_2 PbX_3 [54].
Substitution of the metallic ions has an anomalous effect on the band gap. When Pb and Sn are mixed on the B sites, the band gap of the compound does not lie between the energies of the pure $APbX_3$ and $ASnX_3$ [55]. This effect enables broadening the range of band gaps that halide perovskite can achieve.
Considering the band gap structure of perovskites arises mainly from the $[BX_6]^{-4}$ octahedra network, it may seem that A^+ cations have only a stabilizing role and their effect on electronic structure is negligible. If that was the case, replacing smaller Cs^+ with $CH_3NH_3^+$ would make the band gap just slightly higher, because of the increase in the lattice constant [56]. However, the optical experiments show the band gap decreases from 1.73 eV to 1.55 eV and 1.48 eV for $CsPbI_3$ to $CH_3NH_3PbI_3$

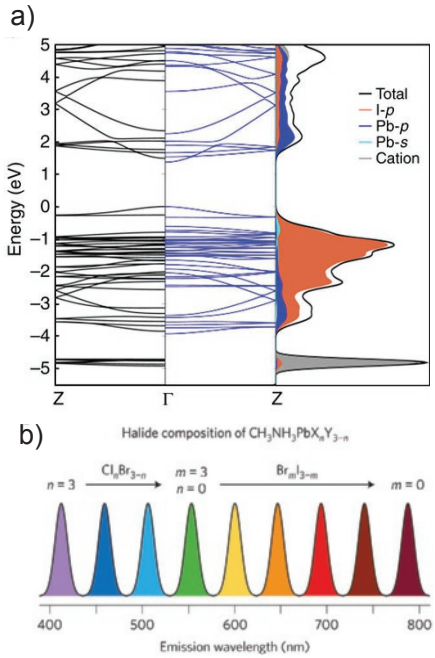

Figure 1.2: Electronic band structure of halide perovskite and effect of ionic components on its band gap. a) Electronic band structure of $CH_3NH_3PbI_3$ in low-temperature orthrombic phase with (black lines) and without (blue lines) organic cation calculated by DFT. The left part of the graph shows the partial density of states, and indicates the contribution of orbitals of each ion in the formation of the band structure. The VBM consists of I $5p$ states and the Pb $6s$ states. The CBM consists mainly Pb $6p$ and I $5p$ states. Reproduced from Ref. [39] with permission from Springer Nature. **b)** Band gap tunability of $CH_3NH_3PbX_nY_{3-n}$. The emission of the $CH_3NH_3PbX_nY_{3-n}$ perovskite is tunable from 390 to 790 nm wavelength. Reproduced from Ref. [40] with permission from Springer Nature.

and then H_2NCHNH_2 PbI_3 respectively. Filip et al. [39] showed that the type and steric size of A^+ cation influences not only the lattice size, but also X-B-X bond angle [39]. On the other hand, the chemical interaction of the A^+ cation with the $[BX_6]^{-4}$ octahedra affects the ionic-covalent nature of chemical bonds. For example, increasing the hydrogen bonds of organic cation make the X-B (metal-halide) nature more ionic, and the VB and CB structures are getting more influenced by metal (Pb or Sn) [57]. Here the spin-orbit coupling from the heavy metals become more significant and decreases the band gap when going from smaller $CH_3NH_3^+$ to the larger $H_2NCHNH_2^+$.

Overall, halide perovskites benefit from defect tolerance which originates from their special band structure. The antibonding coupling of Pb lone-pair *s* orbitals

and halide *p* orbitals cause structural defects such as iodine and methylammonium vacancies forming energy levels outside of the forbidden band gap [58]. This characteristic gives them less defect density in the forbidden band gap compared to more covalent crystalline semiconductors such as CdTe and Cu_2ZnSnS_4 [59, 60]. However, the formation of defects within the conduction and valance band has its own consequences, for example it brings above band gap absorption [59].

1.3 Charge carrier dynamics in halide perovskites

Upon excitation of a semiconductor, the charge carriers are generated via the transfer of electrons from valance band to the higher-energy conduction band (Figure 1.3a). Eventually, the electrons and the holes recombine and release the energy difference between the excited state and the ground state in various energy forms, depending on the recombination process. These processes are schematically illustrated in Figure 1.3b.
In the trap-assisted recombination, a charge carrier (electron or hole) is captured

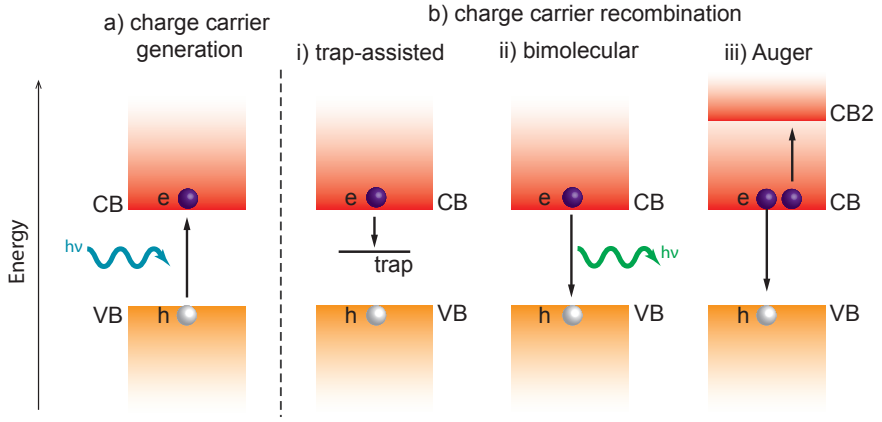

Figure 1.3: Charge carrier generation and recombination mechanisms in semiconductors. a)electron and hole are generated in the semiconductor upon optical excitation with photons with higher energy than semiconductor's band gap. **b)** The electron and hole recombine via various possible recombination mechanisms: *(i) Trap-assisted recombination* is a monomolecular process when the charge carrier is trapped in an extra energy level within the forbidden band gap, formed due to defects or impurities. *(ii) Bimolecular recombination* is the band-to-band transfer of electrons from conduction band (CB) to the valance band (VB) which is followed by the release of energy as a photon. *(ii) Auguer recombination* occurs at the high charge carrier density. The electron and holes recombine band-to-band but the energy of the process is given to a third particle.

in a trap state within the forbidden band gap of the semiconductor. In this process, the energy of the excited state is given off in the form of heat to the lattice phonons. These trap states are usually formed due to the impurities or structural defects in the lattice of the semiconductors. The recombination through the trap states is also referred to as Shockley-Read-Hall (SRH) process[61, 62]. The interruption of the lattice and presence of dangling bonds at the surface can potentially introduce a large density of trap states and make the surface a source of non-radiative recombination in semiconductors[63]. In general, reducing trap states lowers the non-radiative recombination rate, increases the effective lifetime and diffusion length of charge carriers, and boosts the performance of devices. Therefore it is important to recognize the contribution of trap states in the surface and bulk of a semiconductor separately and choose the proper strategies to reduce them in each.
Bimolecular recombination occurs when an electron directly fills the hole in the valance band. The energy of this process is released as a photon with an energy equal to the band gap of the semiconductor. Since the dominant recombination process involving two species (electron and hole) radiates photons, it is also called radiative recombination.
The third recombination processes is Auger recombination, which involves three charge carriers. In this process, an electron and a hole recombine band-to-band, but they give off their energy to a third particle in the form of kinetic energy. The third carrier usually loses its energy as heat. Auger recombination is only significant in non-equilibrium condition at high excitation densities. In this process, both the energy and momentum must be preserved [64]. In fact, Richter et al [65] reported that only at $n > 10^{18}$ the rate equation is related to the carrier density cubic for $CH_3NH_3PbI_3$. Since increasing the band gap of semiconductors makes the conservation of momentum more difficult, Auger processes become less important in materials with higher band gaps [66].
The contribution of each process depends on many factors including the initial carrier density, the semiconductor's electronic band structure and the density and energy of trap states within the band gap. Importantly the energy and density of trap states are sample-dependent factors in halide perovskites, and depend on the morphology and fabrication processes of the material [67]. Thus it is highly important to distinguish these mechanisms in charge carrier dynamics individually. The decay of charge carrier density (n) over time (t) is formulated in Equation (1.3):

$$\frac{dn(t)}{dt} = -k_3 n^3 - k_2 n^2 - k_1 n \tag{1.3}$$

where k_1 is the recombination rate constant associated with the monomolecular trap-assisted recombination, k_2 represents the bimolecular radiative recombination rate constant, and k_3 is the Auger recombination rate constant. As a result, the

total charge recombination rate normalized by carrier density is written as [67, 68] :

$$R(n,t) = k_3 n^2 + k_2 n + k_1 \tag{1.4}$$

and by definition, charge carrier lifetime is the inverse of recombination rate:

$$\tau = \frac{1}{k_3 n^2 + k_2 n + k_1} \tag{1.5}$$

By knowing the rate constants for each process we can predict the contribution of each to the total recombination rate under a given set of material/device parameters. Recognizing which process has the biggest impact on the total recombination rate helps to define strategies to optimize the contribution of each process, depending on the relevant application of the device and its active semiconductor.
In general, radiative recombination is considered non-detrimental for efficient function of optoelectronic devices, and efforts are focused on maximizing this recombination channel compared to the other pathways [67]. In the direct band gap semiconductors, such as halide perovskites, the radiative recombination originates from the band-to-band relaxation of the free charge carriers. Several different processes can lead to emission in a semiconductor, such as radiative recombination of a free exciton, an electron donor-acceptor pair, or trap-mediated florescence [69]. So far there has been no evidence of other radiative pathway than band-to-band relaxation of free holes and electrons [70]. Therefore we can say that only the recombination coefficient k_2 represents this radiative process and non-radiative recombination in halide perovskites is mostly from trap-assisted and Auger. However, Richter et al [65] proposed the existence of a non-radiative bimolecular channel. Although the nature of this recombination is unclear, its presence could be speculated from the difference between the recombination coefficients from transient PL and absorption kinetics of $CH_3NH_3PbI_3$ thin films.
Non-radiative Auger recombination can be harmful for the performance of devices, but according to both experiments and simulations [65, 67, 71] it does not play a role until carrier densities higher than ($> 10^{18}$) in halide perovskite devices. Therefore, although it can be considered irrelevant for light emitting diodes (LEDs) and photovoltaics under standard sunlight performance conditions [67], it is harmful for applications at high excitation densities like lasing devices or solar cells under concentrators.
The nature, density and energy of traps in perovskites is highly dependant on their fabrication processing. This caused a considerable range of recombination rates, charge carrier lifetime and mobility values being reported in literature for perovskites[72]. For instance, for the most studied hybrid halide perovskite, $CH_3NH_3PbI_3$, the PL lifetime varies from nanosececonds to microseconds. It is

suggested that p-type Pb vacancies and n-type methylammonium interstitials form shallow traps near the band edges and cause the PL to quench [58]. Electron-phonon coupling has been also suggested as a cause of below gap excitonic and carrier traps formed in halide perovskites [73].
The nature of perovskites as a mechanically soft and chemically less stable semiconductor as compared to the classical inorganic ones, as well as their low energy of trap formation, makes the defect density and states to be sample preparation-dependent [74] . Therefore the study of the defects in perovskites is a complex issue, depending on several factors such as processing temperature and atmosphere, the ratio and age of the initial components, the duration of process, the time between preparation and performance, and even the measurement conditions like humidity and atmosphere. All these factors can decrease or enhance the defect densities and consequently the recombination rates. Moreover, grain boundaries are a source of defects in the polycrystalline film, therefore lower defect density is expected for single crystalline perovskites. Experimental studies [75, 76] estimated small density of traps for single crystals of $CH_3NH_3PbI_3$ ($\approx 10^{10}$-10^{11}cm^{-3}) and $CH_3NH_3PbBr_3$ ($\approx 10^9$) close to the valance ($\approx$ 0.1 eV) and conduction band ($\approx$ 0.2 eV), matching with the predictions from DFT simulations [77]. These findings indicate the superior performance the single-crystalline perovskite devices may have over polycrystalline thin films.
Non-radiative recombination affects the performance of optoelectronic devices in different ways. For instance, in solar cells it causes the charge carriers to decay rapidly, before they reach the electrodes to be collected and contribute to the current. The non-radiative recombination also lowers the voltage of the device at open circuit (V_{oc}) from V_{oc}^{rad} according to Equation (1.6) [78, 79], assuming that we have perfect contacts, i.e. the quasi-Fermi level splitting is the same as the extracted device V_{oc}.

$$V_{oc} = V_{oc}^{rad} + \frac{k_B T}{q} ln(\eta_{ext}) \tag{1.6}$$

where V_{oc}^{rad} is the V_{oc} at the radiative limit, k_B is the Boltzmann's constant and T is the temperature and q is the electron charge. η_{ext} is the external quantum efficiency given by:

$$\eta_{ext} = \frac{k_2 n^2}{k_3 n^3 + k_2 n^2 + k_1 n} \tag{1.7}$$

Equation (1.6) and Equation (1.7) show that increasing the non-radiative recombination channels reduces the radiative efficiency and results in a reduced solar cell V_{oc}. Therefore achieving highly-efficient solar cells requires strategies to reduce the bulk and surface trap state densities through optimizing processing conditions and passivating the surface or grain boundaries. In light emitting appli-

cations, the high performance of the device also relies on the high radiative efficiency and minimizing the non-radiative recombination pathways according to Equation (1.7). The recombination processes are highly dependent on carrier concentration (Equation (1.4)). [80, 81]. In lasing applications where the carrier densities are considerably higher, the effect of Auger recombination becomes more dominant. Halide perovskites have Auger recombination rate coefficients ≈25 times higher than GaAs [82], therefore halide perovskite-based lasers may suffer more dramatically from non-radiative Auger channels. Since Auger recombination is based on the simultaneous energy and momentum conservation, it strongly depends on the electronic band structure. Tailoring band structure by proper compositional changes in a way to avoid additional bands, for example split-off bands from spin-orbit coupling, is important for designing efficient devices at high injection levels [72].

1.4 Halide perovskites in optoelectronic applications

Halide perovskites as direct band gap solution-processed semiconductors are efficiently applied to many applications from solar energy conversion [83] and storage [84] to light emission [85, 86] and detection[87, 88]. They behave in many ways like more traditional direct band gap inorganic semiconductors with their long carrier diffusion length and high charge carrier mobility [68]. However, their low-temperature solution-based processing (below 200°C) is analogous to organic semiconductors, making them a potential candidate for cost-effective fabrication of flexible, semi-transparent, colorful thin-film and low-weight devices [84]. Here we give an overview of advances in halide perovskite devices, mainly solar cells, light emitting devices (LEDs and lasers) and photodetectors (PD).

As mentioned in Section 1.1, in the early perovskite-based solar cells, the hybrid halide perovskites were employed as light absorber in liquid electrolyte DSSCs because of their high absorption coefficient (1.5×10^4 cm^{-1} at 550 nm compared to the conventional dye 1.5×10^3 cm^{-1} for the Ruthenium based organic dye N719 at 540 nm) and broad absorption spectrum. In these devices, $CH_3NH_3PbI_3$ and $CH_3NH_3PbBr_3$ nanocrystals were deposited on mesoporous TiO_2 instead of the organic dye. The PCE of these early devices were 3.8% for $CH_3NH_3PbI_3$ and 3.1% for $CH_3NH_3PbBr_3$ based solar cells. Optimizing perovskite precursor solution and electrolyte composition later enhanced the PCE to 6.5% [89]. Although these efficiencies showed the potential of halide perovskites for implementation in photovoltaics, the stability of the devices were low. The perovskites in the liquid electrolyte lasted only about 10 minutes before decomposition. Replacement of the electrolyte with spiro-MeOTAD (2,2́,7,7́-tetrakis(N,N-di-p-methoxyphenylamine)-9,9́-spirobifluorene) in the solid-state DSSC structure increased both the perfor-

mance (PCE 9.7%) and stability [90]. Further improvement to above 12% efficiencies was also achieved by employing mixed halide perovskite $CH_3NH_3PbI_{3-x}Cl_x$ for its better stability when processing in air and under light exposure [21, 91, 92].
Within the last years, the architecture of perovskite-based photovoltaic devices developed from DSSC to thin film planar heterojuntion (See Figure 1.4). In a conventional DSSC, the sensitizing dye coats a wide band gap semiconductor (like TiO_2) and absorbs the photon which consequently generates an electron-hole pair. The electrons are transported to the electrode by transferring to the conduction band of the TiO_2, leaving the dye in oxidized state. Simultaneously an electrolyte reduces the oxidized dye to its neutral state and transports the holes to the other electrode. This mechanism is different than conventional inorganic solar cells with *p-n* junction architecture [93]. Due to the higher dielectric constant of inorganic semiconductors, the electron-hole pairs are generated, separated and transported directly within the semiconductor. When the mesoporous n-type TiO_2 in the perovskite-based solar cell was replaced with the insulating Al_2O_3 scaffold [21], it was observed that the open circuit voltage (V_{OC}) and therefore the efficiency was improved . Moreover, transient absorption spectroscopy [92] showed the charge separation is absent in both perovskite/TiO_2 and perovskite/Al_2O_3 interfaces. These reports demonstrated that perovskite itself can sufficiently transport both electrons and holes and enables charge collection in a planar heterojunction, similar to inorganic semiconductors. This was a breakthrough in this field which led to a split of perovskite solar cells from conventional DSSCs and proved the high potential of perovskite solar cells beyond laboratory demonstrations. Today, the international contribution to the progress of this field resulted in the record efficiency of 22.1% in photovoltaic devices. [20]
Despite the high efficiency and relatively simple fabrication of halide perovskite solar cells, several fundamental issues such as performance instability and durability have to be improved. Perovskites in nature consist of ions and evidence of ionic conductivity was reported in inorganic oxide and halide perovskites already many years ago [94, 95]. In hybrid halide perovskites also conduction of ions, known as ionic migration, is proposed to be relevant to the long-term device issues such as degradation[96], and short-term performance issues such as slow response time and hysteresis in current-voltage (I-V) curves [84, 97, 98]. I-V measurement is the typical method to determine the photovoltaic characteristics of solar cells by sweeping the voltage from short circuit to open circuit and recording the current response. In most solar cells, such as Si and organic photovoltaic, the I-V curve does not depend on the direction of the scan, if it is not done too fast [93]. A mismatch between the I-V curves of a perovskite solar cell in forward direction scan (from short circuit to open circuit) and reverse scan is reported since the early stages of perovskite solar cells development [98]. This effect is known as hysteresis. Apart

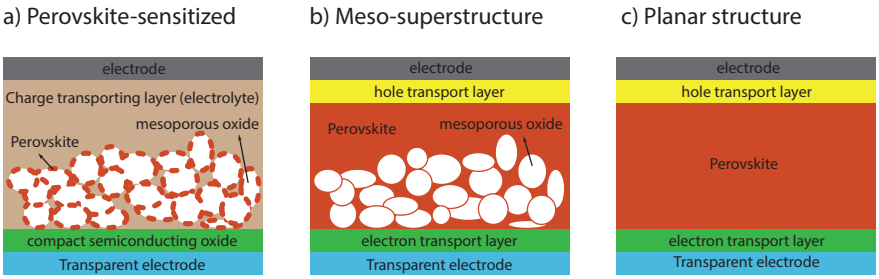

Figure 1.4: Evolution of perovskite solar cells from DSSC to planar heterojunction structure a) DSSC structure, with perovskites coating a porous wide band gap semiconductor (like TiO_2). The perovskite here serves only as an absorber, while TiO_2 transports electrons and a liquid or solid electrolyte transports holes to the respective electrodes. b) In meso-superstructure architecture, perovskite coats a mesoporous metal oxide scaffold. The metal oxide can be a wide band gap semiconductor, or an insulating oxide like Al_2O_3 which only has a role as a scaffold. Perovskite is capable of not only absorbing light, but also transporting charge carriers. c) The planar structure is realized with a thin film of perovskite sandwiched between electrodes, or with extra charge transport layers, but without a metal oxide scaffold.

from ionic migration, ferroelectricity and charge carrier trapping in perovskites have been also proposed as a mechanism behind hysteresis [4]. Ferroelectricity was initially suggested because of the observed ferroelectric behavior in some oxide perovskite compounds such as $BiFeO_3$ and $BaTiO_3$. Although some early studies hypothesized the rotation of organic cations in hybrid halide perovskites could be responsible for ferroelectricity [99] later more detailed simulations and theoretical work disproved that [100]. Another hypothesis for the cause of hysteresis is charge carrier trapping, which was proposed that occurs due to the migration of mobile ions [101] or the interaction of photogenerated charges with the lattice forming deep trap states, known as small polarons [102]. It is also possible that a combination of all mentioned factors are involved in device-related issues or they are inter-related, but how much each factor is involved is still under debate. Whether the ionic migration can be prevented by tuning processing conditions, or if it can be utilized effectively in the design of novel optoelectronic devices beyond photovoltaics, such as memresistors and switchable diodes, remains as an open question in this field. [103]

Application of direct band-gap perovskite semiconductors in light emission devices (such as LEDs, lasers and light-emitting field effect transistors) has been also widely examined [80, 104, 105] . According to detailed balance in the Shockley-Queisser (SQ) limit [106], when only the radiative bimolecular recombination is considered, an ideal light absorber is an ideal LED as well. The tuning of the band gap by

mixing and substitution of the ions in the perovskite makes it possible to access the full visible light color spectrum for light emission applications. The narrow emission spectra (full width at half maximum ≤20nm) [107] of halide perovskites gives them high color purity. These special emission characteristics, in addition to their high radiative recombination rates, long carrier mobility, and defect tolerance [103] attracts many scientists to study halide perovskites for colorful solid-state lighting [85, 86, 108, 109] . The light emission capability of perovskites, especially their 2-D form, was demonstrated in the 1990s, even before their emergence in photovoltaics [110–112]. However, these early perovskite-based electroluminescence devices were only applicable upon charge injection at very low temperatures. Soon during the first years of development of perovskite solar cells, the incorporation of perovskite nanoparticle emitters in a host (alumina) has been realized [113]. A couple of years after, Tan et al [114] demonstrated green, red and infrared LEDs with mixed halide hybrid perovskites thin films ($CH_3NH_3PbI_{3-x}Cl_x$ and $CH_3NH_3PbI_{3-x}Br_x$). The broad spectral tunability of perovskites led to the first demonstration of white light emission (blue, green, red) by blending perovskite nanocrystals [115] and perovskite $CsPbX_3$ quantum dots [116] in a polymer host. So far, a lot of efforts have been put together to increase external quantum efficiency of perovskite LEDs up to 3.5% in the near infrared [117] and 8.5% in the green [104], through improving the hole and electron blocking interlayers [117–121] and perovskite film uniformity [104, 122]. Although these efficiencies have improved since the early demonstrations of perovskite LEDs, they are still below those of the well-established organic and colloidal quantum dot LEDs [40]. The main reason is the dominance of trap-assisted non-radiative recombination of carriers at the normal LED carrier injection densities [85]. Thus, further efficiency improvement towards commercialization of perovskite LEDs should be focused on decreasing the monomolecular recombination through methods such as surface passivation, confinement of the injected carrier within perovskite nanograins [104] and synthesis of trap-free perovskite quantom dots [116], as well as improving carrier-selective injection layers [109].

Apart from applications in LEDs, halide perovskites are considered as potential candidates for low-cost solid-state lasers since the demonstration of amplified spontanous emission of $CH_3NH_3PbI_3$ films at room temperature [43]. The optically pumped lasing of halide perovskites has been presented both in the polycrystalline thin films [80] and single crystal micro and nanostructures, such as nanowires [123], microdisks [124] and nanoplatelets [125]. Realizing electrically injected perovskite lasers, suitable for commercialization of lasing devices, still remains as a challenge in this field [40].

Halide perovskites show also remarkable potentials in a new generation of low-cost light detection devices applicable in several areas such as imaging and opti-

cal communication due to their solution processability, high photoconductivity, wide absorption spectral tunablity and large charge carrier mobility [87, 88]. The direct band gap nature of perovskites potentially can bring a higher performance for perovskite PDs in comparison to the common Si ones [88]. Following the first demonstration of $CH_3NH_3PbI_3$ thin film photodetectors, perovskite light detection devices (including photodiodes, photoconductors and phototransistors) with high responsivity ($\geq 10^4 A.W^{-1}$) [126, 127] and detectivity ($\geq 10^{14}$) [128, 129], large linear dynamic range ($\leq 150dB$) [127, 130], low noise equivalent power ($\leq 50 fWHz^{-1/2}$) [131, 132] and small response time ($\leq 1ns$) [133, 134] have been realized. Especially, improved crystallinity of perovskites and interfacial engineering have led to low dark current in the thin film based devices [135–137]. Besides the perovskite thin film photodetectors with standard vertical and lateral device configuration [88], PDs based on bulk single crystals and nanostructures (nanosheets and nanowires) have been successfully demonstrated [87].
The perovskite optoelectronic devices had an unprecedented progress in many performance aspects to date, however their further commercialization depends tightly on solving issues like long-term stability of both the material and the device, and the toxicity of lead. A full understanding of the degradation mechanism upon exposure to moisture, light, heat and electric field is required to design long lasting devices. Exploring an alternative divalent cation to replace the toxic lead while maintaining the high efficiency of devices, or offering well-established protocols for recycling the lead without environmental damage are the perspectives for the future advances in this field.

1.5 Perovskites single crystals and nanostructures

The development of the halide perovskites for optoelectronics has not been only devoted to the thin films, but also single crystals and various nanostructures of this class of semiconductors. The monocrystalline perovskites benefit from the lack of grain boundaries and low defect density compared to the polycrystalline perovskite films [138, 139]. In addition to the superior properties like longer carrier diffusion length and lifetime [76, 140], perovskite single crystals are an ideal platform to study the intrinsic photophysical properties [141–144] and crystallographic-dependent characteristics such as facet-dependent degradation [145]. The first demonstrations of the organic-inorganic halide perovskites by Weber [11, 12] was on the single crystals grown from solution temperature lowering - a classical chemistry method to make large single crystals. During the emergence of the halide perovskite field in the past few years, this method (also known as seeded solution growth [132, 140, 146, 147]) along with others, such as inverse temperature [143, 148–152] and anti-solvent vapor assisted [76, 144, 153] crystallization has been revisited to grow

bulk milimeter to centimeter size perovskite single crystals. Although these crystal sizes are suitable for laboratory investigations, methods such as Czochralski and Bridgmann [154, 155], which are common for making wafers of Si and other semiconductor crystals, are not fully developed for halide perovskites. This could be due to the high vapor pressure and instability of organic compounds. Although Stoumpos et al [156] fabricated an all inorganic $CsPbBr_3$ single crystal ingot with the Bridgmann method, there is a lot of room for development of large halide perovskite single crystal growth methods. In addition to the bulk crystals, a few recent studies reported large-area single crystal film growth with innovative methods such as cavitation-triggered asymmetrical crystallization [157], modified inverse temperature crystallization [158, 159], space-confined solution-processed strategy for on-substrate growth [160] and wafer-sized geometrically confined lateral crystal growth [161]. So far, the application of bulk single crystal perovskites in highly efficient devices has been limited to the light detection devices [132, 146, 150, 152], due to the unfavorable thickness of them. Incorporation of single crystal thin films into devices such as solar cells and LEDs will be a breakthrough in this field.
Decreasing the dimensions of the perovskite semiconductors tunes their optical band gap further via quantum-size effect. Moreover, nanomaterials can be used for studying the dimension-dependent properties (for example surface effects) as well as building blocks for future optoelectronic devices. Hence, the synthesis and application of various low-dimensional perovskite structures have been investigated extensively in the literature [162], as schematically shown in Figure 1.5. A wide variety of nanostructures are reported in the literature such as 0-D quantum dots and nanoparticles [46, 163–166], 1-D nanowires and nanorods [167–172] and ultrathin 2-D nanosheets and nanoplates [173–177]. Their application is demonstrated in nano-scale devices including optically pumped lasers [45, 123, 178–180], waveguides [181], whispering-gallery-mode nanocavity [125] and also in large-scale devices such as solar cells [170], LEDs [171], photodetectors [182] and field-effect transistors [168] based on nanowire arrays, or solar cells [183–185] and LEDs [46, 115, 186–188] based on quantum dots and nanocrystal assemblies.

1.6 Outline of this thesis

The fabrication and characterization of micro- and nanostructured monocrystalline halide perovskites with optoelectronic applications in mind forms the core of this thesis. $CH_3NH_3PbBr_3$ is chosen as a representative of halide perovskites family, because of the ideal cubic structure, longer stability and less sensitivity to preparation and characterization in the ambient condition. Moreover, $CH_3NH_3PbBr_3$ has a band gap in the visible, between the high band gap energy of $CH_3NH_3PbCl_3$ in the UV and the band gap energy of $CH_3NH_3PbI_3$ in the

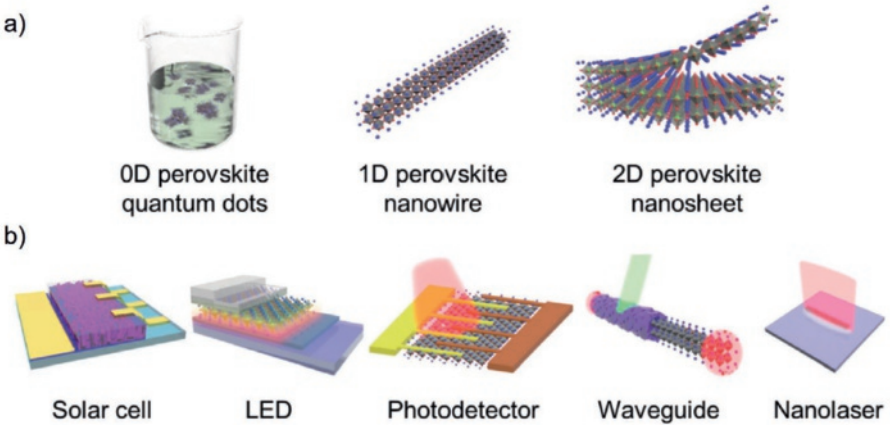

Figure 1.5: Halide perovskite nanostructures' synthesis and application a) Low-dimensional perovskite nanostructures. **b)** The application of nanostructures in optoelectronics. Reproduced from Ref. [162] with permission from The Royal Society of Chemistry.

near-IR.

The first half of this thesis focuses on thin single micro-crystals of $CH_3NH_3PbBr_3$. Most of the common techniques for making perovskite single crystals from solution suffer from long preparation time and non-ideal bulk size of the crystals, resulting in crystals too thick for most device applications. In **chapter two** we present a method based on confining the solvent evaporation to fabricate relatively large perovskite crystals with sub-micron thickness from solution. The well-faceted crystals are proven to be monocrystalline using electron back-scatter diffraction (EBSD) microscopy. This method can be generally extended to other perovskites of the halide family. We also introduce a back-contacted electrode configuration to make simple devices for further optoelectrical characterization.

Ionic migration has been proposed as the main mechanism causing short and long-term degradation in halide perovskite devices. In **chapter three** we aim to study ionic migration and its effect on the performance of back-contacted $CH_3NH_3PbBr_3$ single crystals. We use the introduced platform to map the elemental composition and photoluminescence *in-situ* while the crystals are under applied electric field. The direct observation of halide migration in the single crystals is provided with synchrotron-based nanoprobe X-ray fluorescence (nano-XRF) mapping of the perovskite crystal. We show that ionic migration across the crystal changes the optical properties of the crystal locally and causes superior optoelectronic performance where it is bromide-rich.

The second half of this thesis focused on $CH_3NH_3PbBr_3$ nanowires. In **chapter four** we describe a template-assisted method to fabricate single crystalline perovskite

nanowires via extrusion through anodized aluminum oxide (AAO) pores. With this method single and arrays of free-standing perovskite nanowires are produced with a simple and fast solution-processed technique. The high optical quality of perovskite single nanowires is tested by measuring photoluminescence quantum yield using the integrating sphere microscopy technique.
In **chapter five** we study the photophysical properties of perovskite nanowires embedded in an AAO template. The surface plays a major role in non-radiative recombination channels for charge carriers. In this chapter first we investigate the dynamics of excited states using transient photoluminescence spectroscopy. Then we provide a model to relate the charge carriers' lifetime to the surface to volume ratio of nanowires with various diameters. Using this model, we quantify the surface recombination velocity at the perovskite/alumina interface to understand the role of alumina passivation on the surface of perovskite nanowires.

2

Growth and characterization of PDMS-stamped halide perovskite single microcrystals

Recently, halide perovskites have attracted considerable attention for optoelectronic applications, but further progress in this field requires a thorough understanding of the fundamental properties of these materials. Studying perovskites in their single-crystalline form provides a model system for building such an understanding. In this chapter, a simple solution-processed method combined with PDMS (polydimethylsiloxane) stamping was used to prepare thin single microcrystals of halide perovskites. The method is general for a broad array of materials including $CH_3NH_3PbBr_3$, $CH_3NH_3PbCl_3$, $CH_3NH_3Pb(Br_{0.5}Cl_{0.5})_3$, $CH_3NH_3Pb(Br_{0.75}Cl_{0.25})_3$, $CsPbBr_3$, $Cs_3Bi_2Br_9$ and $Cs_3Bi_2I_9$. Electron back-scatter diffraction (EBSD) was used to investigate the microstructure of the crystals. In order to characterize the microcrystals of $CH_3NH_3PbBr_3$ electrically, the crystals were grown on pre-fabricated electrodes creating single-crystal devices contacted from the back. This back-contacted platform circumvents the incompatibility between halide perovskites and the aqueous chemistry used in standard microfabriation processes. It also allows in situ characterization of the perovskite crystal while it operates as a microscopic device.

2.1 Introduction

Since the introduction of organolead trihalide perovskites as the light-absorbing semiconductor in solar cells [19] much effort has been devoted to the development of these materials for optoelectronic applications [4, 13, 23, 108]. This is due to their high efficiency and inexpensive, solution-based processing. So far the efforts in this field have led to power conversion efficiencies exceeding 22% [20]. The perovskites with formula ABX_3 are crystalline materials in which A and B are cations of different sizes, and X is an anion. To date, most of the work on organic-inorganic hybrid perovskites has focused on materials with A=methylammonium ($CH_3NH_3^+$), B=lead (Pb_2^+), and X=Cl^-, Br^-, I^-, or a mixture of these halides. Mixtures of neighboring anions (e.g. I-Br and Br-Cl) can be produced to tune the band gap from that of pure $CH_3NH_3PbI_3$ (~1.5 eV) to $CH_3NH_3PbCl_3$ (~3.1 eV) [24, 57, 189]. $CH_3NH_3PbBr_3$ (~2.2 eV) sits in the middle of this range, making it and mixtures of it with $CH_3NH_3PbCl_3$ suitable for light-emission applications such as lasing [43] and light-emitting diodes (LEDs) [114, 118]. Mixtures of $CH_3NH_3PbBr_3$ with $CH_3NH_3PbI_3$ are appropriate for solar cells with high open-circuit voltage (V_{oc}) [190–193] and the upper cell in multijunction photovoltaics. Apart from hybrid organic-inorganic perovskites, all-inorganic halide perovskites such as $CsPbBr_3$ (with a band gap of ~ 2.4 eV) have also shown promise for photovoltaics and light-emitting diodes [194, 195].

Because the microstructure and crystallinity of hybrid perovskites are known to affect their properties [196] and performance in solar cells [197], it is important to study single crystalline perovskites free of grain boundaries [198]. Only a few previous studies have examined the growth and properties of single crystalline hybrid perovskites [76, 140, 141, 144, 199–203]. In these works the perovskite crystals were formed by slow crystallization processes, such as antisolvent vapor-assisted crystallization [76], top-seeded-solution-growth [140] or solvothermal growth [199]. These processes are unlike the rapid crystallization that occurs during the drying of the spin-coated films commonly used in solar cells. Also, the crystals' thicknesses of several millimetres were far from those relevant for optoelectronic devices. Therefore these previous studies focused primarily on the photophysical and optical properties of single crystals [141, 199] although Shi et al. [76] and Dong et al. [140] did fabricate electrodes on the top and bottom of their thick single crystals to investigate charge carrier dynamics.

Here we fabricated single-crystalline halide perovskites by applying the typical method of spincoating from solution used to make polycrystalline thin films. A PDMS-stamping step confined the solution during evaporation of the solvent and resulted in the formation of individual crystals. The typical thickness of the crystals grown by this method (500 nm to a few μm, depending on the processing

conditions) is much closer to what is commonly used in high-performance optoelectronic devices and can be reduced further to 100 nm by adjusting the deposition conditions [204] This method is general and can be applied to form thin single crystals of a variety of hybrid, inorganic, and lead-free halide perovskites.

2.2 Fabrication of perovskite microcrystals using PDMS-stamping method

Flat and smooth halide perovskite crystals were produced by combining solution deposition with a PDMS-stamping technique. To form the crystals, a stoichiometric solution of the perovskite precursors in relevant solvent (details in Section 2.6) was spin-coated onto the substrate. Prior to deposition of the solution, the substrate was cleaned with an O_2 plasma, which made it hydrophilic. Immediately after the deposition of the solution, the substrate was pressed face down into a piece of PDMS heated on a hotplate (100-200 °C) until the solvent had evaporated (Figure 2.1a-b). Individual crystals formed randomly on the substrate, and crystallizing in contact with the flat surface of the PDMS created faceted, smooth crystals with thicknesses of a few micrometers to hundreds of nanometers, depending on the deposition conditions (Figure 2.1c).The morphology of the crystals, including their size and thickness, was influenced by several parameters, such as the concentration of the precursor solution, additives to the solution such as hydrobromic acid, and the method of deposition of the solution before stamping (e.g. drop-casting or spin-coating). The crystals, however, were not produced uniformly over the entire substrate, likely because pressure was applied non-uniformly across the substrate; therefore, in each sample at least five crystals were measured on the substrate using either a profilometer or an atomic force microscope (AFM). Because of this sampling procedure, the chart boxes that compare the thicknesses of the crystals fabricated by different parameters are not necessarily representative of the thickness variations over each substrate. In general, however, a lower concentration of solution gave a majority of thinner crystals (below 1 μm), but the lateral dimensions of the crystals decreased as well. Addition of HBr or using DMSO as the solvent 30 decreased the thickness of $CH_3NH_3PbBr_3$ crystals. Spin-coating also provided a more uniform size distribution than drop-casting.
If the PDMS-stamping step was not applied, rapid evaporation of the solvent in the absence of PDMS produced unshaped crystals with very rough surfaces, as shown in the optical image of the $CH_3NH_3PbBr_3$ crystals in Figure 2.2a-b . AFM images of the surface of several $CH_3NH_3PbBr_3$ crystals indicated that the root-mean-square (rms) roughness was 7.1±4.6 nm as compared to 79.1±43.3 nm for crystals formed without stamping (Figure 2.2c-d).

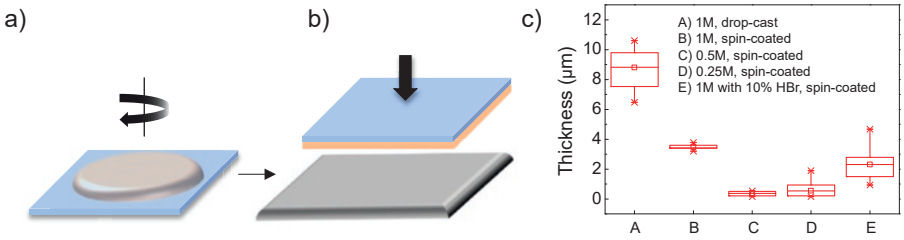

Figure 2.1: PDMS-stamping technique for fabrication of smooth and thin halide perovskites. **a)** Spin-coating of solution on top of the prepared platform. The solvent was not allowed to evaporate fully. **b)** Pressing the substrate face down into PDMS on a hotplate (100°C) until the crystals formed. **c)** Controlling the thickness of $CH_3NH_3PbBr_3$ crystals. All samples were prepared by deposition of freshly prepared $CH_3NH_3PbBr_3$ precursor solution in DMF with varied concentrations onto a glass substrate via the listed technique (drop-cast or spin-coated). For Sample E, 10 vol% of hydrobromic acid (HBr) (48% in H_2O) was added to the solution.

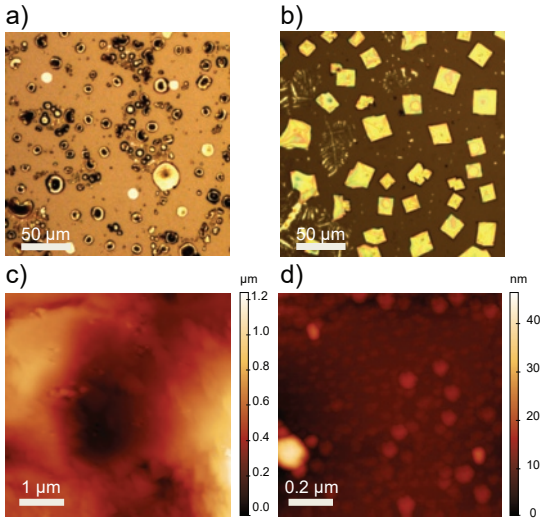

Figure 2.2: Comparison of the stamped and un-stamped $CH_3NH_3PbBr_3$ crystals. **a)** Optical microscopy image of $CH_3NH_3PbBr_3$ crystals formed by spin coating of solution on a glass substrate without and **b)** with PDMS-stamping. **c)** Atomic force microscopy image (AFM) of the surface of the crystal without and **d)** with PDMS-stamping.

This method is broadly applicable to produce smooth single crystals of a library of halide perovskites. In addition to crystals of $CH_3NH_3PbBr_3$, PDMS-stamped microcrystals of $CH_3NH_3PbCl_3$ and mixed halides ($CH_3NH_3Pb(Br_{0.75}Cl_{0.25})_3$ and $CH_3NH_3Pb(Br_{0.5}Cl_{0.5})_3$) were also generated (Figure 2.3a-c). By varying the spin conditions and annealing temperatures, this method also produced crystals of a variety of other halide perovskites, including inorganic $CsPbBr_3$ and lead-free hexagonal perovskites such as $Cs_3Bi_2I_9$ and $Cs_3Bi_2Br_9$ (Figure 2.3d-f).

2.3 Crystallinity of PDMS-stamped $CH_3NH_3PbBr_3$ microcrystals

The individual crystals of $CH_3NH_3PbBr_3$ formed by PDMS-stamping are typically single crystals with a faceted, square-prismatic shape. The smoothness of their surface allows the identification of the orientation and domains of the crystals by electron backscatter diffraction (EBSD) (Figure 2.4). EBSD is a SEM-based technique that is well established to determine the crystallographic orientations of microstructures [205, 206] In this technique, the focused electron beam strikes the surface of the crystal at a high angle (here, 70°). Electrons scattered from the surface form a diffraction pattern, called a Kikuchi pattern because of its prominent

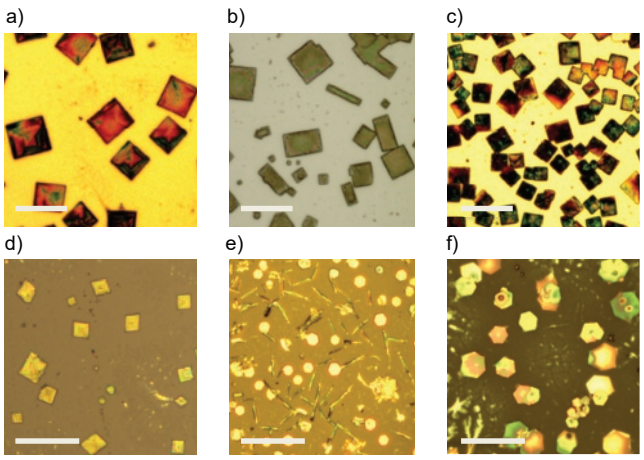

Figure 2.3: Optical microscopy image of variety of halide perovskite crystals including **a)** $CH_3NH_3PbCl_3$ **b)** $CH_3NH_3Pb(Br_{0.75}Cl_{0.25})_3$ **c)** $CH_3NH_3Pb(Br_{0.5}Cl_{0.5})_3$ **d)** $CsPbBr_3$ **e)** $Cs_3Bi_2I_9$ **f)** $Cs_3Bi_2Br_9$. These crystals fabricated by spin coating of solution on glass, followed by PDMS-stamping. scale bars in a-c are 20 μm and in d-g are 50μm.

Kikuchi bands [206]. Several positions on the surface of each smooth crystal of $CH_3NH_3PbBr_3$ were measured (Figure 2.4a). The Kikuchi patterns from these positions (Figure 2.4b) were similar, indicating that there are no grain boundaries within the crystal. Indexing the Kikuchi patterns (Figure 2.4c) for fourteen different single crystals showed that the surface plane is (100) (Figure 2.4d). Single-crystal X-ray diffraction confirmed the single crystallinity of the square crystals (Section 2.6.6). Although many of the crystals formed using PDMS-stamping were square prisms, others displayed a line along their diagonal (Figure 2.5). EBSD patterns taken from opposite sides of the line were dissimilar, indicating that the line is a grain boundary between a <100> domain and a <110> domain. EBSD was also used to analyze the microstructure of $CsPbBr_3$ PDMS-stamped crystals, which were also typically single crystals (Figure 2.6).

2.4 Optical and electrical characterization of $CH_3NH_3PbBr_3$ single crystals

Optical characterization of the PDMS-stamped single crystals of $CH_3NH_3PbBr_3$ was performed by diffraction-limited absorption and photoluminescence (PL) measurements (excitation wavelength of 405nm) (Figure 2.7) on a 1-micron thick crystal. The PL spectrum, which was collected in reflection, shows a narrow emission peak centred around 540 nm (2.29 eV). The onset of absorption is red-shifted and located at ~555 nm (2.25 eV). Controlling the thickness of the crystals allowed the measurement of the material's complex refractive index from 405-1100 nm, which agreed well with values measured on macroscopic single crystals.[30]
To characterize the $CH_3NH_3PbBr_3$ single crystals electrically in a simple schottky junction device, the crystals must be contacted to metal electrodes; however, standard lithographic techniques require processing substrates in aqueous solutions, which will dissolve the ionic perovskite crystals. For this reason, electrodes were fabricated on the substrate using photolithography prior to the growth of the crystals (Section 2.6).The first requirement for the electrodes is their appropriate energy band alignment relative to the bands of the perovskite. The valence and conduction band edges of $CH_3NH_3PbBr_3$ have been reported as 5.9 eV and 3.6 eV, respectively [207]. Based on these band positions several metals were candidates for electron- or hole-selective electrodes.34 In the back-contacted geometry, however, the perovskite crystals are deposited on top of the electrodes, so the metals of the electrodes should be chemically inert in the solution containing the perovskite's precursors and in contact with the perovskite itself. TiO_2 is the common electron transporter material used in conventional planar perovskite solar cells [208], therefore, titanium was a clear choice for the electron-selective contact. A thin

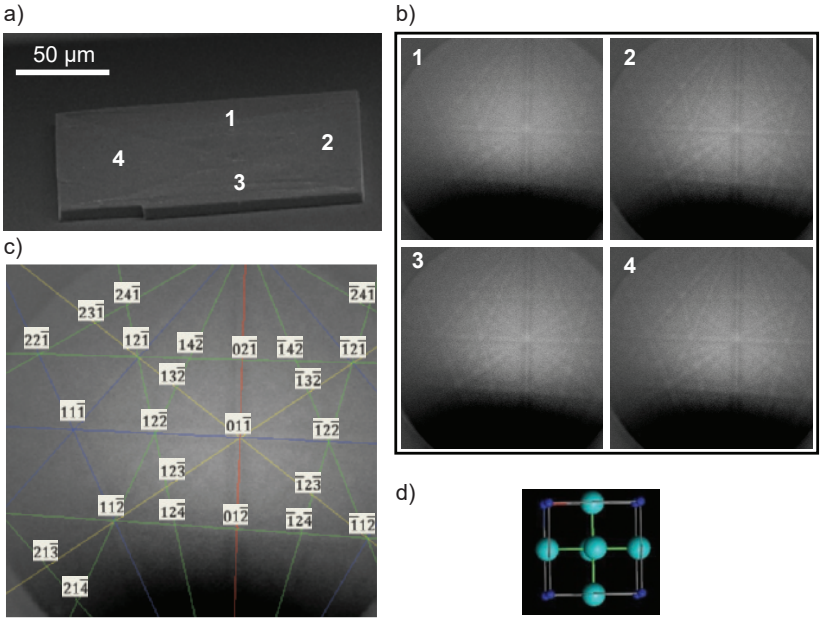

Figure 2.4: Electron backscatter diffraction (EBSD) of a $CH_3NH_3PbBr_3$ crystal. **a)** SEM image of a $CH_3NH_3PbBr_3$ single crystal. Numbers indicate the positions of the electron beam where the EBSD patterns were collected. **b)** EBSD patterns from four different locations on the crystal, which all show the same Kikuchi pattern indicating the same crystallographic orientation. Each pattern is related to the location with the similar number in a. **c)** Indexed EBSD pattern. **d)** The orientation of the surface of the $CH_3NH_3PbBr_3$ crystal is <100>, extracted from the indexed EBSD pattern. Light blue spheres are bromide anions, while dark blue spheres are the methylammonium cations.

titanium oxide layer forms on the surface of Ti metal and likely prevents chemical reactions between the perovskite and the underlying metal. Palladium was chosen as the hole-selective contact, and no damage to the electrodes were observed after deposition of the crystals or during measurements. Further details regarding the selection of electrode materials are given in the Section 2.6.7.

To produce solar cells, back-contacted devices with asymmetric contacts (Ti-Pd) were fabricated, followed by deposition of the perovskite crystals (Figure 2.8a). Current-voltage (I-V) curves of the devices were measured in the dark and under illumination with a standard light source (AM 1.5G, 100 mW cm^{-2} irradiance) (Figure 2.8b). The devices displayed rectifying I-V curves both in the dark and under illumination. A champion back-contacted single crystal solar cell had an open-circuit voltage (V_{oc}) of 1.04 V and 1.07 V in forward and reverse scans, respectively, better than the V_{oc} of the first demonstration of planar $CH_3NH_3PbBr_3$

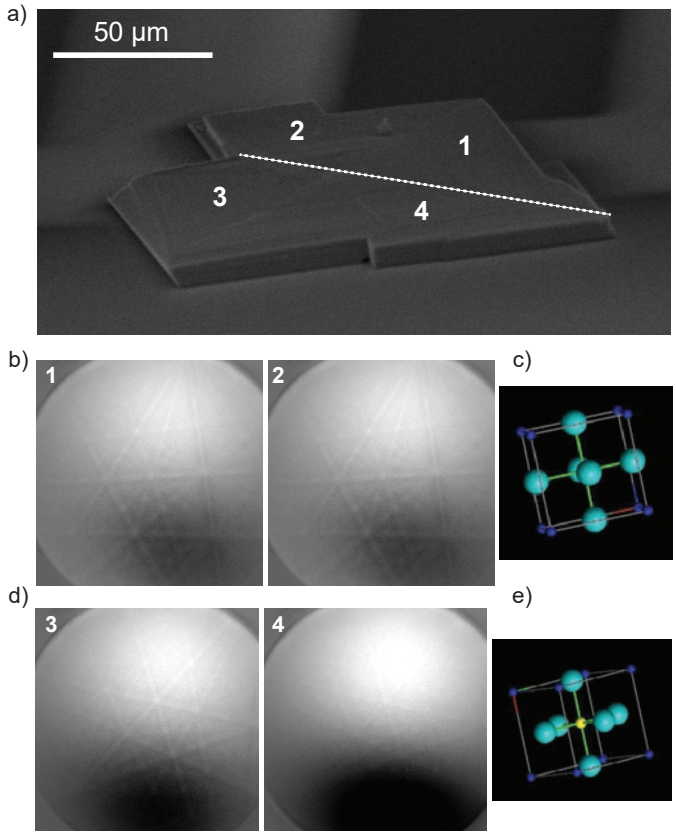

Figure 2.5: EBSD of a crystal with two domains. **a)** SEM image of the crystal of $CH_3NH_3PbBr_3$. Numbers show the position of the electron beam where the EBSD patterns were collected. The dashed line indicates the boundary between domains, based on the crystal's morphology and EBSD patterns. **b)** and **d)** EBSD patterns from different locations on the crystal, as indicated by numbers on a). Patterns 1 and 2 show similar kikuchi lines, whereas they are different from patterns 3 and 4, from points on the opposite side of the line. **c)** and **e)** crystal structure of the $CH_3NH_3PbBr_3$ extracted from kikuchi patterns in b and d. The crystal orientations of the patterns are <100> (b) and <110> (c). Light blue spheres are bromide anions, while dark blue spheres represent the methylammonium cations. The yellow spheres are the lead cation.

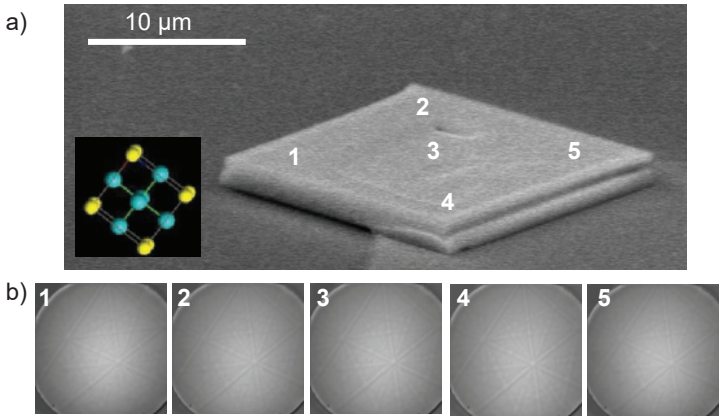

Figure 2.6: Electron backscatter diffraction of a CsPbBr3 crystal. a) SEM image of a $CsPbBr_3$ single crystal. Numbers indicate the positions of the electron beam where the EBSD patterns were collected. The inset shows the crystal structure constructed from kikuchi patterns. Green spheres are Br anions, while blue spheres represent the Cs cations. The yellow spheres are the Pb cation. **b)** EBSD patterns from 5 different locations on the crystal as numbered in a), which all show the same Kikuchi pattern indicating the same crystallographic orientation. Each pattern is related to the location with the similar number in (a).

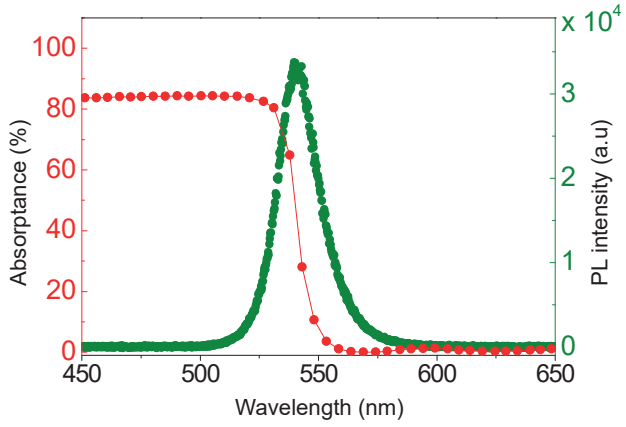

Figure 2.7: Optical characterization of $CH_3NH_3PbBr_3$ single crystal. Absorption (red) and photoluminescence (PL) (green) spectra of a CH3NH3PbBr3 single crystal prepared by the PDMS-stamping technique

perovskite solar cells in literature 14 (0.84V) but somewhat lower than cells with more optimized hole-selective layers (1.3 V) [192] and later studies (1.4V and 1.51V) [190, 191]. The single crystal $CH_3NH_3PbBr_3$ solar cell exhibited a short circuit current (I_{sc}) of 0.93 nA and 1.96 nA in forward and reverse scan directions, respectively, which is equivalent to 0.58 and 1.23 mA.cm^{-2} short circuit current density (J_{sc}). The J_{sc} was calculated by considering the overlapped area of the crystal with the Ti electrode as the active area, according to photocurrent mapping (Figure 2.9). Again, these values are comparable to those of early planar $CH_3NH_3PbBr_3$ perovskite solar cells (1.08 mA.cm^{-2}) [192] although later studies [190, 191] with improved hole transporter layers [192] and improving surface coverage of the $CH_3NH_3PbBr_3$ [190] demonstrated much higher J_sc values (6.113 and 8.412 mA.cm^{-2}). These reports show the importance of the hole transporter layer and suggest that the back-contacted single crystal $CH_3NH_3PbBr_3$ solar cell performance will improve substantially with deposition of proper charge transporter layers.

To investigate the spatial distribution of the photocurrent within the device, scanning photocurrent mapping using laser illumination (power density ~250 W.cm^{-2} at 540 nm) was applied on various $CH_3NH_3PbBr_3$ single crystal devices(Figure 2.9) . The positions of the crystals and electrodes were correlated to the photocurrent maps by superimposing the reflectance map (Figure 2.9a) of the crystal taken simultaneously with the photocurrent map and the optical image (Figure 2.9b). This correlation shows that the photocurrent originates only from the region of the crystal directly above the Ti electrode. Moreover, not all of the areas above this electrode are equally active.

The observation of current localized to the electron-selective Ti contact suggests

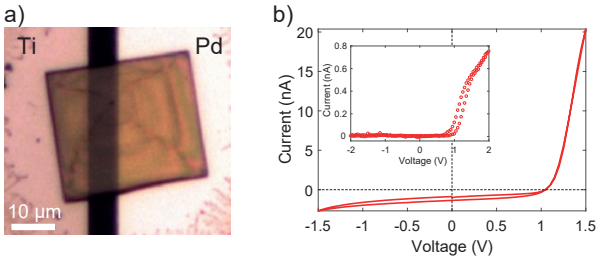

Scan direction	V_{oc} (V)	I_{sc} (nA)	J_{sc} (mA.cm^{-2})
Forward	1.04	0.93	0.58
Reverse	1.07	1.96	1.23

Figure 2.8: Electrical characterization of a back-contacted $CH_3NH_3PbBr_3$ single crystal. **a)** Optical microscopy image of the single crystal prepared on a pre-fabricated back-contacted electrode platform. **b)** I-V characteristic of the $CH_3NH_3PbBr_3$ single crystal device under 1-sun illumination. Inset shows the I-V curve of the crystal in dark **c)** The photovoltaic performance of the device in the forward and reverse scan directions (scan rate 0.1 V/s) .

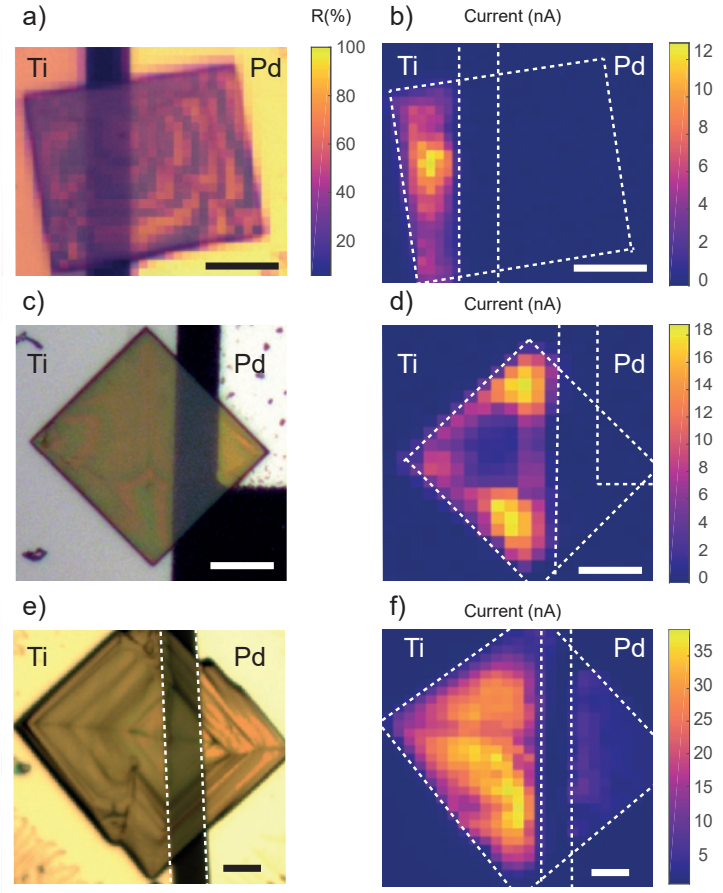

Figure 2.9: Scanning photocurrent map of $CH_3NH_3PbBr_3$ back contacted crystals (λ=540 nm, ~ 250 W.cm^{-2}). a) Over-laid optical microscopy image of the same crystal in Figure 2.8 on its reflection map, used as a reference to correlate the photocurrent map positionally with the crystal. **b)** Photocurrent map of the crystal in Figure 2.8. Dashed lines indicate the position of the electrodes, drawn from the superimposed reflection map and optical image. **c)** and **e)** Optical images of two different back-contacted $CH_3NH_3PbBr_3$ single crystals. **d)** and **f)** Correlated Photocurrent maps of crystals in c and e, with the lines indicating the position of the electrodes and crystals driven from superimposed reflection maps and optical images. The scale bars are 10 μm.

a short diffusion length for electrons in $CH_3NH_3PbBr_3$. In the case of illumination near the hole-selective electrode, electrons must travel laterally through the width of the gap between the electrodes (few microns) to be collected by the Ti contact. If their diffusion length is shorter than this width, they recombine before being collected; therefore, regions of the crystal far from the Ti electrode appear inactive. When the crystal is illuminated near the electron-selective contact, electrons must travel only the vertical distance between their position of excitation and the electrode. Since this crystal is relatively thin (~1μm) and the energy of the incident photons (2.29 eV) is close to the band gap of $CH_3NH_3PbBr_3$ (~2.2 eV), some electron-hole pairs are generated close enough to the back contact for the electrons to be collected. The lack of significant lateral current decay from the edge of the electrode indicates that the carrier diffusion length is smaller than the size of the optical spot, approximately 1 μm. This short electron diffusion length is consistent with predictions of p-type conductivity in $CH_3NH_3PbBr_3$ [209] and reported electron diffusion lengths in polycrystalline films of ~100 nm (in dark) and ~360 nm (under 0.03-0.04-sun illumination), which were measured by electron-beam-induced current (EBIC) [210] In millimeter-sized single crystals, Shi et al. [76] reported much longer diffusion lengths (~3-17 μm) determined by measuring the mobility and photoluminescence lifetime of their crystals. These larger crystals grown by slow precipitation over several days likely have fewer defects than the perovskite deposited by rapid precipitation after spin-coating, yielding a longer diffusion length.

The second observation in the photocurrent map of the $CH_3NH_3PbBr_3$ single crystal is the non-uniformity of the photocurrent over the Ti contact. The locations of spots with highest current on the photocurrent map vary for different measured crystals (Figure 2.9c-f). While most of the region on the Ti electrode produces more than 3 nA of current, some regions produce as much as four times that amount. Because the photocurrent map is a convolution of light absorption and charge collection, the variations could arise from either process. For thin crystals, changes in thickness can lead to dramatic variations in photocurrent because absorption is enhanced or suppressed by thin-film interference; however, a simple one-dimensional model (details in Figure 2.10) based on the AFM-measured thicknesses in this crystal (Section 2.6) indicates that the observed variations are too large to arise from interference effects alone (Figure 2.10). Variations in the efficiency of charge collection could also contribute to this inhomogeneity and might result from a non-uniform interface between the electrode and perovskite. For example, the nucleation site of the crystal might produce the most intimate contact with the electrode, which could locally enhance the efficiency of charge collection. Differences in the thickness or chemical composition of the titanium oxide layer on the surface of the electrode could also influence the local collection

efficiency and yield the observed variations in photocurrent.

2.5 Conclusion

In summary, we have introduced a simple technique to create smooth, thin halide perovskite microcrystals by combining single-step deposition of precursors from solution with PDMS-stamping. This method is general for making a variety of halide perovskites, including hybrid, all-inorganic, and lead-free hexagonal perovskites. Because of the smooth surface of the crystals, EBSD could be used to identify the microstructure of $CH_3NH_3PbBr_3$ crystals, which typically exhibited a (100) surface facet. These single crystals are ideal for studying perovskite optoelectronic devices on a fundamental level, as used in this chapter and further in Chapter 3. To this end, the crystals were electrically contacted from the back to avoid any post-growth fabrication steps that might damage the crystals. Here, We used this back-contacted platform to investigate the photovoltaic performance of single-crystal $CH_3NH_3PbBr_3$ and performed photocurrent mapping of the device to understand the spatial distribution of its photogenerated current. The photocurrent originated from the portion of the crystal directly above the electron-

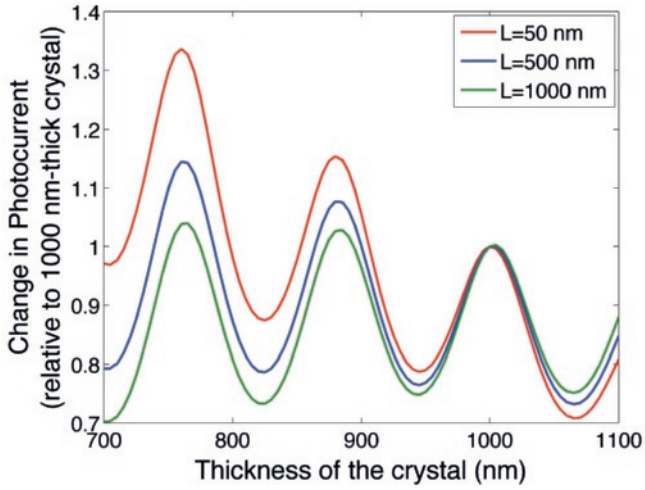

Figure 2.10: Calculation of the relative change in photocurrent (at λ =540 nm) expected with changes in the thickness of the crystal. Changes are estimated relative to a 1000-nm-thick crystal and for three different diffusion lengths (L). A thickness variation in the crystal can cause both increases and decreases in photocurrent, but the total magnitude of the change (from minimum to maximum) is always less than a factor of two.

selective contact, suggesting these $CH_3NH_3PbBr_3$ single crystals are p-type and have an electron diffusion length below 1 μm. This PDMS-stamping approach, together with the back-contacted platform for electrical characterization, provides a unique tool to investigate the optoelectronic properties of a variety of single-crystalline halide perovskites.

2.6 Supplementary Information

2.6.1 Experimental methods

Preparation of methylammonium halide

(CH_3NH_3X, X=Br or Cl): CH_3NH_3X was synthesized by the addition of hydrobromic acid (48% wt. in H2O, Sigma-Aldrich) or hydrochloric acid (37% wt. in H_2O, Sigma-Aldrich) dropwise into methylamine (33% wt. in EtOH, Sigma-Aldrich) while it was stirring in an ice bath. After stirring for 2 hours in the ice bath, the solution was removed and heated to 150°C to evaporate off the solvents, while stirring was continued. The resulting powder, either white or occasionally pale yellow, was recrystallized from ethanol. The final white crystals of CH_3NH_3X were dried by heating at 100-150°C in air.

Preparation of halide perovskite solutions:

All solutions were prepared at room temperature and in air. To prepare pure $CH_3NH_3PbBr_3$ crystals, $PbBr_2$ (Sigma-Aldrich, purity ≤98%) was mixed in a 1:1 molar ratio with CH_3NH_3Br in dimethylformamide (DMF) (Sigma-Aldrich, anhydrous, 99.8%) or dimethyl sulfoxide (DMSO) (Sigma-Aldrich, anhydrous, purity≤ 99.5%). For pure $CH_3NH_3PbCl_3$ crystals, $PbBr_2$ (Sigma-Aldrich, purity ≤98%) and CH_3NH_3Cl were mixed in a 1:1 molar ratio in DMSO at 1 M concentration. To prepare mixed halide ($CH_3NH_3Pb(Br_{0.5}Cl_{0.5})_3$ and $CH_3NH_3Pb(Br_{0.75}Cl_{0.25})_3$) solutions, pure 1 M solutions of $CH_3NH_3PbBr_3$ and $CH_3NH_3PbCl_3$ in DMSO were mixed in the desired stoichiometric ratio (1:1 or 3:1). For making the all-inorganic $CsPbBr_3$ solution, CsBr (Sigma-Aldrich, 99.999%) and $PbBr_2$ precursors were mixed in a stoichiometric ratio in DMSO (0.33 M solution). $Cs_3Bi_2I_9$ and $Cs_3Bi_2Br_9$ solutions were made by mixing CsBr with $BiBr_3$ (Sigma-Aldrich, purity ≤98%) and CsI (Sigma-Aldrich, 99.9%) with BiI3(Sigma-Aldrich, 99%) in a stoichiometric ratio in DMSO (concentrations well below 1M). The fresh solutions were ultrasonicated for 5 minutes to ensure full dissolution of the precursors prior to deposition.

Fabrication of single-crystals:

The perovskite solution was spin coated on fused silica substrates. The substrates were cleaned with acetone, isopropanol, and O_2 plasma prior the deposition. A RIE/ICP plasma etcher from Oxford Instruments (Plasmalab 80 plus) was used to remove the contamination and treat the surface of the substrates. The process parameters were as follows: O_2 flow of 25 sccm, pressure of 30 mTorr, and forward power of 50 W for 2 minutes. The spinning speed and time were adjusted to prevent the full evaporation of the solvent (10 seconds at 500 rpm for DMF solutions and 30-60 s at 2000-4000 rpm for DMSO solutions). The wet substrate was immediately pressed face down onto a piece of PDMS on a hot plate held at 100°C (for DMF solutions) or 150°C (for DMSO solutions) for 2-5 min, until the crystals formed and the substrate changed color. Inorganic perovskites in DMSO were annealed at 150-200°C. After the crystals were formed on the substrate in contact with PDMS, the sample was removed from the PDMS and annealed for about 10 min face up to ensure the evaporation of excess solvent. The PDMS stamp was fabricated by mixing the monomer and curing agent (10:1 ratio, SYLGRAD 184, Dow Corning) and curing on a piece of clean Si wafer. The side formed in contact with the Si was always used to stamp the crystals. PDMS stamps were reused after cleaning the surface by ultrasonication in water and a rinse in isopropanol.

Electrode fabrication:

The electrodes were fabricated on glass substrates by a two-step photolithography process. Glass substrates were cleaned in acetone and isopropanol prior to spin coating with photoresist. In the first step, one set of electrodes was patterned, and the metal was deposited by electron-beam or thermal evaporation, followed by lift-off in acetone. The second lithography step was repeated as the first one, using alignment markers to adjust the gap between the electrodes. Another metal was then deposited. In the case of symmetric devices, the lithography was done in one step. The thickness of the metals was 100 nm. The geometry of electrodes is shown in Figure 2.11.

Device fabrication:

To make $CH_3NH_3PbBr_3$ back-contacted devices, the same procedure of spin coating the precursor solution followed by PDMS-stamping was applied using substrates with pre-fabricated electrodes. To fabricate the devices, O_2 plasma cleaning of substrates was necessary to form consistent contacts. Using a table-top plasma cleaner to prepare the electrodes resulted in inferior devices. Atomic force microscopy: AFM images were taken by a Veeco Dimension 3100 in tapping mode.

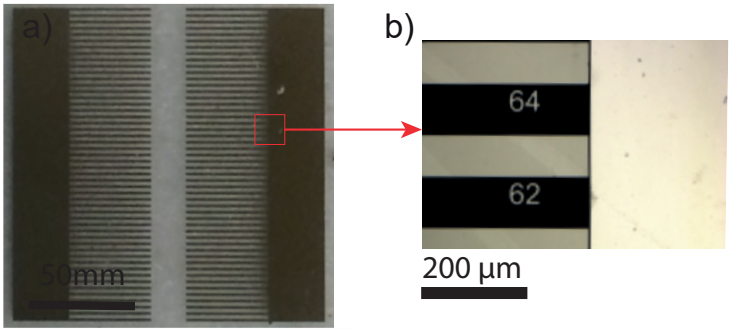

Figure 2.11: Configuration of electrodes of $CH_3NH_3PbBr_3$ back contacted devices. **a)** Full device image. The large pads on the edges of the sample and electrode lines are made in 2 separate lithography steps for devices with asymmetric electrodes. **b)** Enlarged image of the electrodes' configuration in the red box in a. The gap between the electrode pad and lines is 2μm

2.6.2 Scanning electron microscopy

SEM images were taken by a FEI Verios 460 at 5 kV accelerating voltage, in secondary electron mode, and under a 30° tilt.

2.6.3 Electron Backscatter Diffraction (EBSD)

The EBSD setup was built in a FEI XL30 S FEG. The patterns were collected using 20 kV accelerating voltage and 6nA beam current. The exposure area was 1μm^2 and exposure time for hybrid perovskite crystals 10 seconds and for inorganic perovskites 3-6 minutes. The sample was tilted 70°. The patterns were indexed using Delphi 2 software from EDAX. The system was calibrated prior to indexing with Si (100).

2.6.4 Device Characterization

I-V curves were measured with an Agilent B2902A source-measure unit. To simulate solar illumination, an Oriel Sol2A Class ABA Solar Simulator from Newport was used. 1-sun intensity was calibrated using a silicon reference cell (Newport 91150V).

2.6.5 Scanning Photocurrent Mapping

The photocurrent maps were taken using a home-built optical setup (similar to Section 4.6.2, without using integrating sphere in the setup) consisting of a supercontinuum Fianium WL-SC390-3 laser, sent through an acousto-optic tunable filter

(Fianium AOTF-V1-N1). The beam was focused through the objective (Mitutoyo M PLAN APO NUV 50X, NA 0.42) onto the mounted substrate. The spot radius was 650 nm. The sample was electrically wire-bonded to a printed circuit board specially designed for the setup and scanned spatially with the focused laser beam using a piezoelectric stage (Piezosystem Jena Tritor 400 CAP). The photocurrent was measured with the same source-measure unit as used for *I-V* measurements. The voltage on the sample was scanned from zero up to 2V and then returned to zero prior to measuring the photocurrent map, and the mapping was done while the sample was kept at the short-circuit condition. The reflected beam power was measured simultaneously with a Thorlabs amplified photodiode (PDA100A) to correlate the position with the current in the superimposed maps. A silicon photodetector (Newport model 818-UV-L) was used to measure the absolute beam power in each measurement.

2.6.6 Single-crystal X-ray diffraction of $CH_3NH_3PbBr_3$

To confirm the single-crystalline character of the grown $CH_3NH_3PbBr_3$ crystals, the unit cell parameters of several randomly selected crystals were measured using single crystal X-ray diffraction. In all cases the cubic unit cell was found (a = b = c = 5.92$\mathring{A}$), which is in accord with previous reports [11, 76, 211]. Solution of the crystal structure of one of the selected crystals confirmed the $Pm\bar{3}m$ space group (no. 221). As pointed out by Knop et al. [211] in this space group, the $CH_3NH_3^+$ cation has to be positionally disordered over at least 6 equivalent C-N orientations. This should also lead to a small intensity of diffraction compared to the contributions of Pb^{2+} and Br^-. Indeed, due to this disorder, determining the precise location of the N and C atoms was difficult; however, a model with the $CH_3NH_3^+$ cation being disordered over 12 positions led to a satisfactory R-value. The assignment of the N versus C atoms was based on the expectation that the NH_3^+ group should be directed towards the negatively charged Br^- atom. During an unconstrained refinement, due to the positional disorder, the C and N atoms tended to shorten their distance to values close to 1 $\mathring{A}$; therefore, their distance was constrained to 1.50 $\mathring{A}$ and these atoms were refined isotropically. As a result of the disorder, no satisfactory positioning of the hydrogen atoms of the $CH_3NH_3^+$ cation could be obtained, as after refinement they tended to occupy chemically wrong locations; therefore, for the final solution the hydrogen atoms were not included. The above results are in agreement with the structure recently reported by Shi et al.[209] (Figure 2.12). The crystal structure of $CH_3NH_3PbBr_3$ achieved from single crystal XRD measurement is shown in Table 2.1 . The full data set is presented elsewhere [212]

Data was collected on a Bruker D8 Quest Eco diffractometer, equipped with a TRI-

Table 2.1: Single Crystal XRD Data of $CH_3NH_3PbBr_3$

Temperature	296 K
Wavelength	0.71073 $\AA$
Crystal size	0.026 × 0.187 × 0.227 mm
Crystal system	cubic
Space group	$Pm\bar{3}m$
Unit cell dimensions	a = 5.92 $\AA$, α = 90°
	b = 5.92 $\AA$, β = 90°
	c = 5.92 $\AA$, γ= 90°
Volume	207.71 $\AA^3$
Z	1
Density (calculated)	3.829
	g/cm^3
Absorption coefficient	34.633 mm^{-1}
F(000)	206

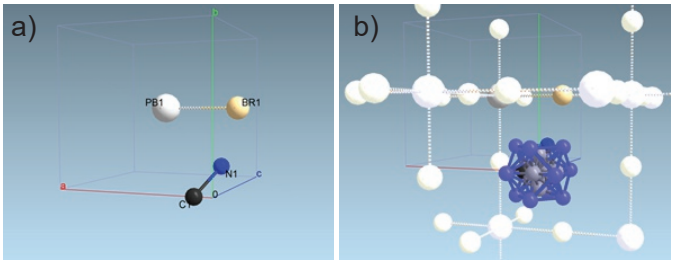

Figure 2.12: Crystallographic structure of $CH_3NH_3PbBr_3$ derived from single crystal XRD study. a) Asymmetric unit of $CH_3NH_3PbBr_3$ **b)** positional disorder of the $CH_3NH_3^+$ cation. Visualization was made with ShelXle

UMPH monochromator and a CMOS PHOTON 50 detector, using Mo-Kα radiation (λ = 0.71073 $\AA$). The intensity data were integrated with the Bruker APEX2 software [213]. Absorption correction and scaling was performed with SADABS [214]. The structures were solved with SHELXT. Least-squares refinement was performed with SHELXL-2014 [215].A relatively thick orange crystal of $CH_3NH_3PbBr_3$, approximate dimensions 0.026 mm × 0.187 mm × 0.227 mm, was used for the X-ray crystallographic analysis. The X-ray intensity data were measured. A total of 86 frames were collected. The total exposure time was 0.24 hours. The frames were integrated with the Bruker SAINT software package using a narrow-frame algorithm. The integration of the data using a cubic unit cell yielded a total of 496 reflections to a maximum θ angle of 26.16° (0.81 $\AA$ resolution), of which 68 were independent (average redundancy 7.294, completeness = 100.0%, R_int = 5.49%,

R_sig = 3.85%) and 68 (100.00%) were greater than 2σ(F2). The final cell constants of a = 5.9222(18) $\AA$, b = 5.9222(18) $\AA$, c = 5.9222(18) $\AA$, volume = 207.71(19) $\AA$3, are based upon the refinement of the XYZ-centroids of 75 reflections above 20 σ(I) with 6.818°<2θ< 52.30°. Data were corrected for absorption effects using the multi-scan method (SADABS). The ratio of minimum to maximum apparent transmission was 0.215. The calculated minimum and maximum transmission coefficients (based on crystal size) are 0.0470 and 0.1780. The final anisotropic full-matrix least-squares refinement on F^2 with 9 variables converged at R1 = 3.52%, for the observed data and wR2 = 10.26% for all data. The goodness-of-fit was 1.349. The largest peak in the final difference electron density synthesis was 2.540 e^-/ $\AA^3$ and the largest hole was -1.561 e^-/ $\AA^3$ with an RMS deviation of 0.290 e^-/ $\AA^3$. On the basis of the final model, the calculated density was 3.829 g/cm^3 and F(000), 206 e^-.

2.6.7 Materials selection for the electrodes of the back-contacted platform

In order to make solar cells with $CH_3NH_3PbBr_3$,first the electrodes were fabricated on glass substrates using two steps of photolithography prior to the deposition of the perovskite crystals (as explained Section 2.6.1). Because the electrodes are fabricated before deposition of the crystals, this platform avoids the difficulty of finding a process for layer deposition that will not damage the perovskite. Standard processes for thin-film deposition - such as those requiring high temperature, plasma, incompatible solvents (e.g water), or oxidizing environments - can be used to fabricate the underlying contacts. Also, if no surface reactions occur between the electrodes and the perovskite, this structure is also a reusable test platform because the crystals can be removed using a suitable solvent. After the solution deposition and PDMS stamping, crystals were distributed randomly on the substrate so that some bridged the gaps between the electrodes. The large size of the crystals, whose edges often exceed 50 μm, enables optical imaging and facilitates in-situ characterization of the devices (as later presented in Chapter 3). In this chapter and Chapter 3 Ti, Pd and Pt were chosen as electrodes for back-contacted perovskite devices based on the following criteria.

In order to choose the correct carrier-selective electrode for $CH_3NH_3PbBr_3$ back-contacted devices,first a list of metals with higher work function than the valance band and lower work function than the conduction band of $CH_3NH_3PbBr_3$ was considered (Figure 2.13). Next requirement for selecting the electrode material is chemical stability of the electrode in the perovskite precursor solution. Ti electrodes were stable upon the deposition of the perovskite solution. When the $CH_3NH_3PbBr_3$ devices with symmetric electrodes (Ti-Ti) were fabricated, they had linear I-V curves, indicating the ohmic nature of the contact (Figure 2.13b). Other

metals with similarly small work functions, such as aluminium and silver, were also tested; however, severe corrosion of the metal was observed immediately following deposition of the perovskite solution.
Devices with Pd-Pd contacts were fabricated to test Pd as a hole-selective electrode for $CH_3NH_3PbBr_3$ solar cell devices. They were stable and conductive but showed saturation in their current (Figure 2.13c). While the cause of this saturation is unknown, similar behavior arises in other semiconductors when scattering with phonons or impurities imposes a limit on the drift velocity of the carriers at high fields. Alternatively, saturation can also appear when the conduction channel of the device becomes restricted, as is the case in transistors [217]. Gold and nickel were also tested as hole-selective electrodes; however, Au electrodes were disregarded according to a recent study showing the diffusion of gold atoms into perovskite layer [101]. In the case of devices with symmetric Ni-Ni electrodes, although no damage to the electrodes was visible after deposition of the perovskite crystals, running current through the devices caused them to break down electrically, and the

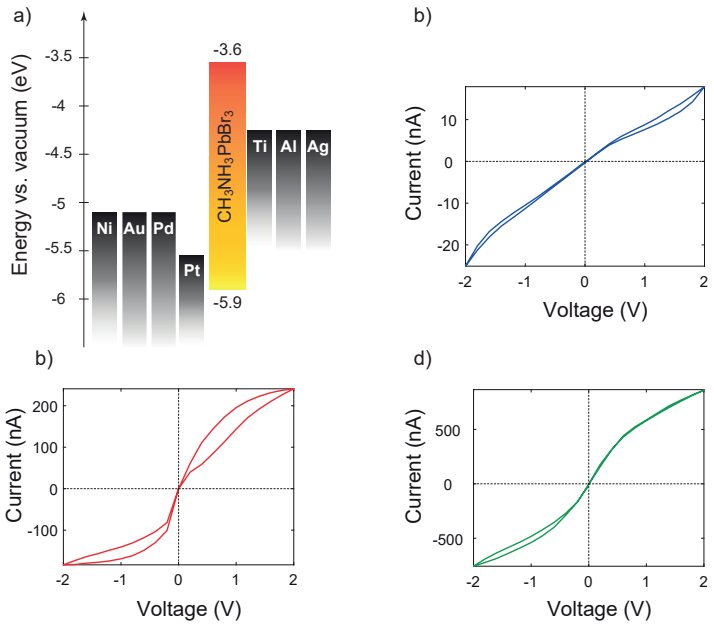

Figure 2.13: Electrical characterization of $CH_3NH_3PbBr_3$ single crystals using the symmetric back-contacted device platform a) Energy band diagram for $CH_3NH_3PbBr_3$ [216] and metals with appropriate work functions for extracting holes and electrons. **b)**I-V curves of CH3NH3PbBr3 single crystals in the dark (gray) and under 1-sun illumination (colors) with symmetric electron-selective electrodes (Ti-Ti) and **c)** symmetric hole-selective electrodes (Pd-Pd).

appearance of the nickel electrode was altered. Rather than Palladium, Platinum was also selected as an appropriate contact and showed behavior similar to that of palladium. This electrode platform was used later for the devices presented in Chapter 3.

2.6.8 One-dimensional model to calculate relative changes in photocurrent based on changes of the thickness

In general, the photocurrent (I) at a particular wavelength in a crystal of thickness d is given by:

$$I = \int_0^d G(x).C(x)dx \tag{2.1}$$

where G(x), is the generation profile as a function of depth (x), and is calculated numerically using a transfer-matrix model that accounts for thin-film interference and back reflection from the Ti electrode [218]. Values of the refractive indices for the perovskite[204] and Ti [219] were taken from the literature. The refractive index of the TiO_2 was measured by ellipsometry. The collection efficiency was modeled as an exponential decay from the perovskite-electrode interface:

$$C(x) = C_0 e^{(x-d)/L} \tag{2.2}$$

in which C_0 is a constant that describes the collection efficiency at the perovskite-metal interface, d is the thickness of the crystal, and L is the minority carrier diffusion length. Based on this calculation, the changes in photocurrent in Figure 2.9 (a factor of four increase) cannot arise solely from a local change in the crystal's thickness (d), assuming that the local collection efficiency at the contact (C_0) and diffusion length (L) remain constant. AFM (Figure 2.14) shows that the crystal's thickness over the Ti electrode varies in the simulated range, from 760 to 1000 nm.

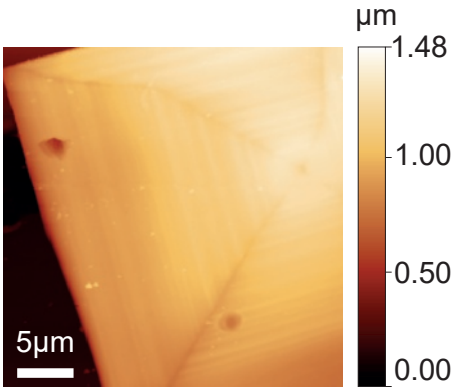

Figure 2.14: Atomic force microscopy of the $CH_3NH_3PbBr_3$ single crystal device presented in Figure 2.9a

3

Halide migration and its effect on the photoluminescence of single crystal perovskites

Single crystal perovskites are the simple structures to study perovskites to their most fundamental properties. In this chapter we varied the electric field applied to single crystals of methylammonium lead bromide and mapped changes in both their elemental composition and photoluminescence. Synchrotron-based nanoprobe X-ray fluorescence (nano-XRF) with 250 nm resolution revealed quasi-reversible field-assisted halide migration, with corresponding changes in photoluminescence (PL). We observed that higher local bromide concentration was correlated to superior optoelectronic performance in $CH_3NH_3PbBr_3$, while regions with lower bromide concentration showed decreased PL intensities . A lower limit on the electromigration rate is calculated from these experiments, and the motion is interpreted as vacancy-mediated migration based on nudged elastic band density functional theory simulations. The XRF mapping data provides direct evidence of field-assisted ionic migration in a model hybrid perovskite thin single crystal, while the link with photoluminescence proves that the halide stoichiometry plays a key role in the optoelectronic properties of the perovskite.

3.1 Introduction

Halide perovskite materials have shown promise for a wide range optoelectronic applications including light-emitting diodes [114], photonic lasers [123], and solar cells [220, 221] . Despite their impressive potential demonstrated in laboratory devices, questions remain regarding many of the fundamental properties that govern their performance limits, especially their stability under hot [222], humid [223], illuminated [224] and biased operating conditions [225]. Understanding both the origin of this instability and its connection to performance is key to developing perovskite optoelectronic devices beyond the laboratory.

Many groups have suspected ionic migration under an electric field and illumination as an important limiting mechanism in hybrid perovskite devices, particularly in regard to current-voltage sweep hysteresis [97, 226–229]. Assuming thermal equilibrium and non-interacting defects, perovskites are predicted to have a high concentration of vacancies ($10^{17} - 10^{20} cm^{-3}$ for $CH_3NH_3PbI_3$) [230]. Evidence of vacancy-mediated diffusion of X-site anions (in the ABX_3 structure) with low activation energy through the conventional hopping mechanism along the anion octahedral edge has been determined for oxide [231] and inorganic halide perovskites [94]. In the analogous hybrid halide perovskites, extensive computational investigations, particularly in the methylammonium lead iodide ($CH_3NH_3PbI_3$) system, have shown that I^- is likely the most mobile ion because it exhibits a lower energy barrier to migration in comparison to Pb^{2+} and $CH_3NH_3^+$ [226, 228, 232]. Several groups have observed ionic migration of both organic cations and halide anions and in $CH_3NH_3PbI_3$ and $CH_3NH_3PbI_{3-x}Cl_x$ using techniques such as energy-dispersive X-ray spectroscopy (EDX) [233, 234], time-of-flight secondary-ion-mass spectrometry (tof-SIMS) [235], X-ray photoemission spectroscopy (XPS)[236] and IR microscopy mapping techniques [234]. These analytical techniques each have their own specific limitations. For instance, tof-SIMS involves sample fragmentation and physical destruction of the investigated area [237]; IR microscopy can detect bond stretches of the organic components in perovskite films but is generally not sensitive to the low-frequency vibrations of the inorganic components [238]; and XPS is sensitive only to the first few nanometers near the surface and requires high-vacuum conditions. EDS must be applied with caution to halide perovskites because of their sensitivity to electron beam damage [224, 239]. Finally, the nanoprobe X-ray fluorescence (nano-XRF) technique maps heavy elements throughout the bulk of the sample with higher spatial resolution and sensitivity than XPS, tof-SIMS, EDS, or IR microscopy.

Recently, synchrotron-based nanoprobe X-ray fluorescence (nano-XRF) mapping has been shown to be an effective probe of local composition in $CH_3NH_3PbI_{3-x}Cl_x$ devices without affecting the elemental distribution[240]. During nano-XRF mea-

surement, a focused X-ray beam excites core-shell electrons from the atoms in the sample. When a core-hole is filled by relaxation of an outer shell electron, a fluorescent photon is emitted, and its energy identifies the element from which it came due to the characteristic energy of electronic transitions. As a photon-in, photon-out process, nano-XRF is dose efficient, critical for radiation-sensitive materials like the hybrid perovskites and enables nanoscale elemental mapping with part per million sensitivity for elements heavier than sodium [241]. The many-millimeter working distance at hard X-ray energies also facilitates *in situ* and *in operando* studies [242]. More details of XRF technique is discussed in the Supplementary Information (SI) (see Section 3.6).

The best way to provide a direct link between composition and performance is to combine spatially-resolved elemental or chemical detection methods with techniques that probe the material' s local optoelectronic properties. Luminescence spectroscopy and imaging are versatile techniques to probe recombination mechanisms and dynamics in semiconductors. For example, recently researchers have

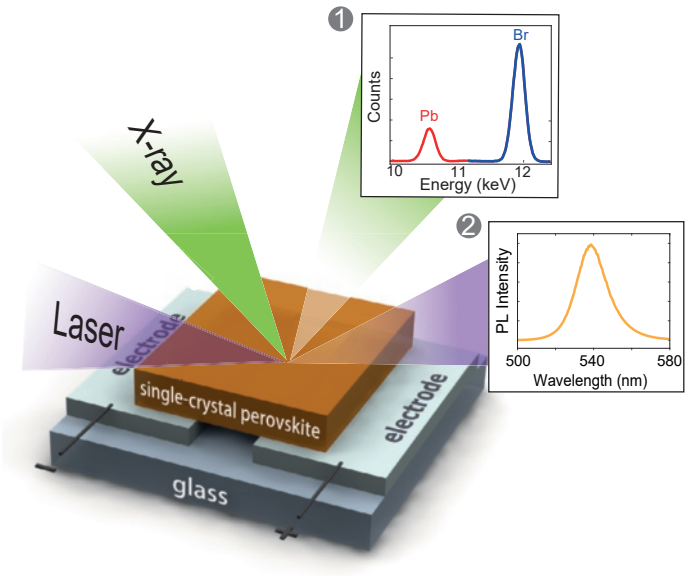

Figure 3.1: schematic of nanoprobe X-ray fluorescence and spatially resolved photoluminescence (PL) measurement. A 250 nm FWHM X-ray beam excites elemental fluorescence that reveals the local perovskite stoichiometry in single crystals bridging Pt-Pt electrodes. Subsequently, a laser beam excites optical luminescence to elucidate local optoelectronic quality. Note XRF and PL were not performed at the same time, but sequentially in a correlative microscopy approach.

used spatially-resolved luminescence to reveal the role of Cl in $CH_3NH_3PbI_{3-x}Cl_x$ [220], to correlate contact resistance with morphology [243, 244], and to understand the degradation of the perovskite layer [245] and its interfaces [244]. Despite the importance of ionic migration, open questions remain as to how stoichiometric changes affect to photoluminescence a property directly linked to device performance [78, 246].

In this study, we identify a direct relationship between halide migration and local optoelectronic quality. Direct elemental evidence of halide migration in a $CH_3NH_3PbBr_3$ single crystal is detected using nano-XRF. Thin single crystals of $CH_3NH_3PbBr_3$, which are tens of micrometers wide and ~500 nm thick, are used as a model system (fabricated according to the method presented in Chapter 2) to study the fundamental properties of ionic migration in hybrid perovskites, avoiding complications from grain boundaries that are present in perovskite thin films. In response to an applied electric field, local stoichiometric variations appear along the crystal, which are correlated to local changes in the PL intensity. PL intensity increases in halide-rich regions and decreases in halide-poor ones, with quasi-reversible variation observed over multiple voltage biasing cycles. Furthermore, nudged elastic band (NEB) density functional theory (DFT) computations confirm that Br^- ions experience a low energy barrier to migration within the $CH_3NH_3PbBr_3$ structure. The direct link between local stoichiometry and optoelectronic quality also clarifies that halide migration is a challenge that is intrinsic to the absorber and one that may play a determining role in the ultimate performance limits of perovskite devices.

3.2 Nanoprobe X-ray fluorescence mapping

Nano-XRF mapping is used to identify the spatial distribution of elements within a $CH_3NH_3PbBr_3$ single crystal under applied bias. The crystals bridge Pt electrodes, and the voltage is applied laterally across the device as shown in Figure 3.1. Pt electrodes prevent any driving force from a difference in the work functions of two different metals and also minimize chemical reactions or diffusion [247] of metallic atoms at the metal/perovskite interface [101]. Although, some small variations due to slightly different surface of Pt, like surface roughness variations or impurities may exist. Prior to the XRF measurement, electrical contact between the perovskite crystal and Pt electrodes was confirmed by current-voltage (I-V) scans (Figure 3.2). Fluorescence spectra were collected at each point during the XRF mapping using a synchrotron X-ray beam with a 250 nm full-width half maximum. Figure 3.3a shows the corresponding optical micrograph of the $CH_3NH_3PbBr_3$ crystal studied by XRF. To check the stability of the crystals under the X-ray beam and also the reproductivity of the XRF experiment, first a repeated x-ray mapping was performed

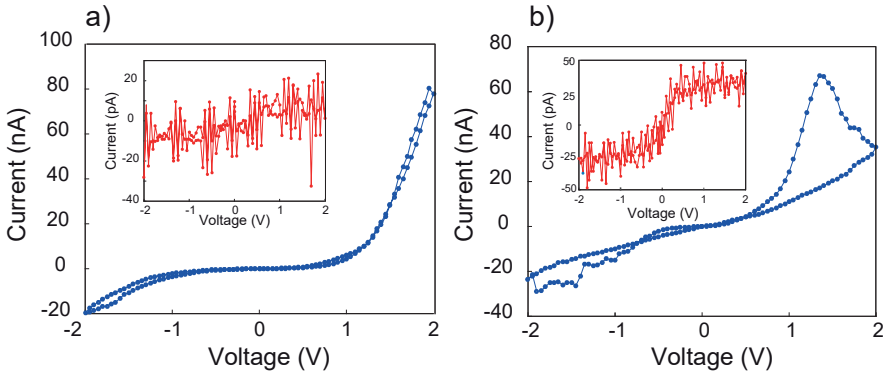

Figure 3.2: The I-V test under AM1.5G illumination of $CH_3NH_3PbBr_3$ crystals on Pt-Pt electrodes to ensure electrical contact and photoresponse prior to **a)** X-Ray exposure for XRF and **b)** laser exposure for PL measurements. Insets in both a and b show I-V curves under dark condition. Both IV curvers show the crystals were electrically contacted to the electrodes and their current enhances by light illumination.

on a crystal without electrical contacts. As expected, the spatial distribution and elemental composition of the crystals are uniform on the 250-nm length scale of measurement during repeated X-ray mapping under the focused 13.6 keV X-ray beam with a flux of 2.37×109 photons/sec (Section 3.6.1). The same conditions then were used to map a crystal on the electrodes with and without electrical bias. Note that the light elements in the methylammonium cation are not detectable by XRF, but the major heavy elements Pb and Br are detectable with sensitivity down to parts per million.

The local Br:Pb stoichiometry within the $CH_3NH_3PbBr_3$ single crystal is initially homogeneous across the crystal, prior to applying the bias, but changes systematically during application of an external electric field (Figure 3.3b). The seven XRF maps of the Br:Pb atomic ratio in the 30×30 μm^2 crystal are arranged from left (Map 1) to right (Map 7) based on the chronological sequence of applied bias. Map 1 is the initial scan showing the Br:Pb atomic ratio. As expected, the initial area-averaged Br:Pb ratio across the crystal was 3.08±0.2. An arrow above each XRF map measured under bias indicates the direction of the electric field. In this experiment the left electrode is held at ground and the right electrode has the applied voltage bias V_{app} (orange arrow (V_{app} = -2V) and blue arrow (V_{app} = +2V)). The Br:Pb ratio is plotted because it removes the effects of small spatial variations in thickness, but the shift in Br:Pb ratio seen in Figure 3.3 results entirely from a change in the Br distribution, as the Pb distribution remains constant throughout the XRF mapping (Figure 3.9).

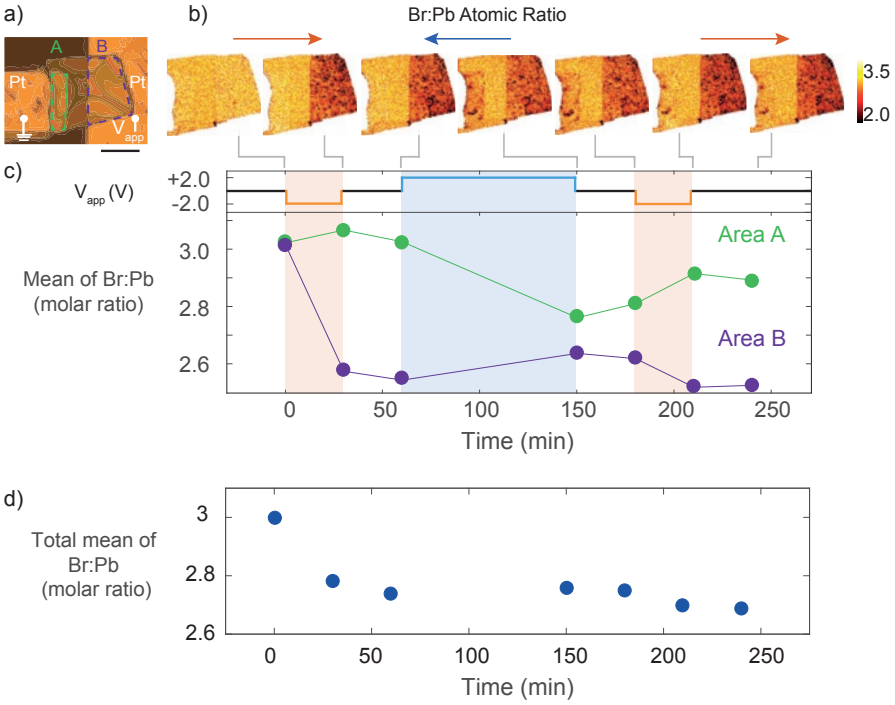

Figure 3.3: anoprobe X-ray fluorescence (Nano-XRF) measurement of the changes in elemental distribution in a $CH_3NH_3PbBr_3$ single crystal under bias. **a)**An optical image of the $CH_3NH_3PbBr_3$ crystal characterized by nano-XRF. Regions A and B where the crystal covers the two different electrodes are indicated. The electrode under region A is grounded and the other electrode is biased. Scale bar is 15 μm. **b)**X-ray fluorescence maps of the Br:Pb elemental ratio with 250 nm step size and 100 ms dwell time per point under a sequence of +/- 2V biases. The direction of the corresponding electric field for each map under bias is denoted by an arrow above the map (-2V orange and +2V blue). **c)**The mean Br:Pb ratio of Area A and Area B as measured by X-ray fluorescence during the bias sequence with the corresponding bias condition (top). Time spent at -2V is shaded in orange and +2V in blue. **d)** Average Br:Pb ratio with respect to time over the entire crystal

To examine the migration of ions under electric field, the perovskite crystal underwent a total of three poling cycles, from unbiased to +/- 2V bias to unbiased. After collecting the initial unbiased map (left of Figure 2b), a -2V DC bias was applied. After 30 minutes of bias applied without X-ray irradiation, we collected an XRF map (25 min duration) with the bias still applied to observe the effect of the electric field. The change in the Br:Pb atomic ratio between Maps 1 and 2 clearly indicates depletion of Br above the electrode at lower potential (right Pt pad). This depletion is consistent with the direction that Br^- anions would migrate. The bias was then removed, and after a 30 min relaxation period, a third XRF map was taken to visualize any diffusion along the Br concentration gradient. The Br concentration is then slightly depleted over the left-hand electrode as Br^- diffuses back in the absence of bias.

When the direction of the bias is reversed (+2V), the Br shifts toward the positively biased electrode, also consistent with migration of Br^-. A significant Br shift away from the left-hand negative electrode is observed in Map 4, while the Br concentration recovers slightly on the right-hand electrode (Map 2 vs 4). Upon subsequent relaxation in Map 5, a small recovery in the Br distribution is again seen. The last cycle seen in Maps 6 and 7 repeats the same -2V and 0V bias condition as Maps 1 and 2, respectively. It confirms that the observed changes in the Br:Pb distribution are partially repeatable.

The lower bound for mobility of Br ions is estimated at room temperature using Equation (3.1).

$$\mu = v/E \tag{3.1}$$

where μ is the mobility, v is the velocity and E is the applied electric field. The applied electric field is 2000 V/cm given the applied voltage of 2V and the gap space between electrodes of 10 μm. Knowing the 1800s duration of applied bias, the drift velocity (v) is calculated to be 5.56×10^{-7} cm/s . This estimates the lower bound of Br drift mobility at room temperature as 2.78×10^{-10} cm^2/V.s.

To assess the migration of Br^- within the crystal more quantitatively, the changes in average Br:Pb atomic ratio above each of the two electrodes are presented in Figure 3.3c. The average ratio is plotted with respect to time and applied bias. As Br:Pb increases on one electrode, a decreasing ratio is seen on the other, providing additional support for an ion migration mechanism. The largest Br concentration change occurs above the lower potential electrode (Electrode B) right after the first bias is applied, when the Br:Pb ratio drops from 3.0±0.03 to 2.6±0.07 . All subsequent changes are smaller, and the Electrode B area never recovers fully its initial Br concentration. On the other hand, Electrode A exhibits a more reversible response to applied bias and largely recovers from the smallest Br:Pb ratio near 2.8±0.09 to

2.9±0.06 after final relaxation. Small, severely Br deficient regions evidenced by localized dark spots in Figure 3.3 develop above both electrodes over time. These regions indicate local degradation of the perovskite phase and possible formation of $PbBr_2$. After biasing the crystal for 4 hours, the area-averaged Br:Pb ratio in the last XRF map (rightmost) is 2.69. The loss of Br occurs predominantly during the first negative bias of each electrode, after which the total average concentration of Br was fairly stable (Figure 3.3d). Given what appears to be nanoscopic local formation of $PbBr_2$ in some regions, one could speculate that trace amounts of CH_3NH_3Br leaves the sample in an electrochemical reaction in regions of negative bias under X-ray irradiation. On the other hand, little change of the Br:Pb ratio away from 3.0 is observed between the electrode gap throughout the biasing cycles. Overall, the Br:Pb distribution shifts in the direction opposite the applied field at all time points.

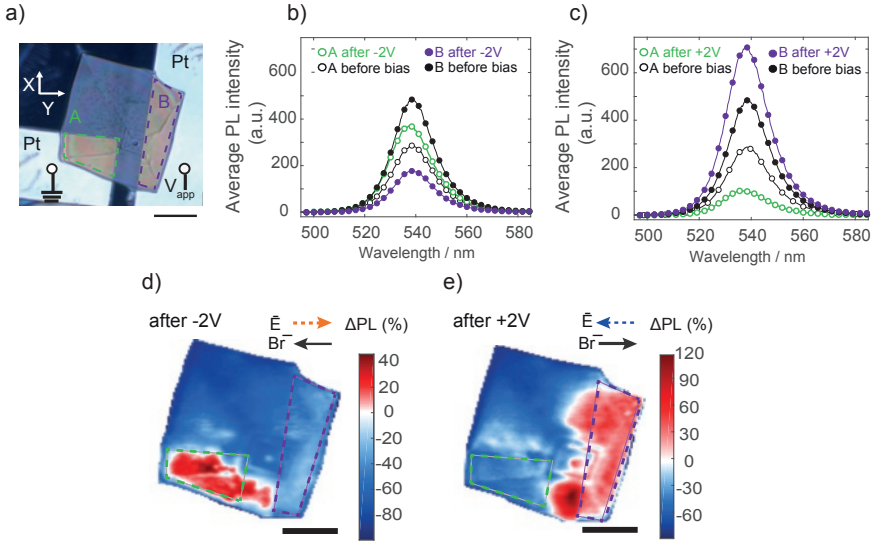

Figure 3.4: Photoluminescence mapping of $CH_3NH_3PbBr_3$ crystal. **a)**Optical image of a hybrid perovskite crystal on Pt electrodes with labeled regions of interest A and B. **b)** and **c)** Overlaid photoluminescence spectra in Areas A and B after -2V and after +2V biasing, respectively. Black curves in each figure represent the initial PL intensity before any biasing in areas A and B. Plots with empty and filled markers correspond to average PL spectra of areas A and B, respectively. The corresponding spatially-resolved relative PL intensity maps are shown in (d) for -2V bias and (e) for 2V bias relative to the initial unbiased PL map. Scale bars are 15 μm.

3.3 Photoluminescence mapping

A fresh $CH_3NH_3PbBr_3$ microcrystal, (optical image shown in Figure 3.4, I-V scan in Figure 3.2b), from the same sample chip is used to explore how the local optoelectronic properties vary in response to similar bias sequences as were used in the nano-XRF experiments. The crystal was excited using a 15 μW, 405 nm continuous-wave violet laser while performing PL mapping before, during, and after bias as presented in Figure 3.5a-g. Each map took ~30 min to be collected. PL emission spectra were collected for each point of the crystal by moving the stage in the X and Y directions by 333 nm steps, and PL maps were constructed from the integration of the total emission intensity over the wavelength 500-580 nm.

Enhancement of PL intensity under bias at the forward biased electrode and its reduction at the reverse biased electrode area is attributed to the change of the depletion region width at each contact. Similar changes in PL emission intensity with the variation of DC bias were reported in other semiconductors such as InP, GaAs, and CuGaSe2 [248–250]. To compare crystals at the same bias condition, the PL emission spectra averaged over the area of each electrode (area A and B) were collected at zero bias after applying and removing the electric field as shown in Figure 3.4b-c. An increase in PL intensity relative to its initial value was observed in the region above the electrode previously held at higher potential. A decrease was observed over the contact at lower potential. According to the XRF maps in Figure 3.3, the contact with the higher potential is where the Br concentration is higher; therefore, the Br^- rich regions exhibit enhanced PL after removal of the electric field.

Figure 3.4d-e show the spatial variation of PL intensity across the crystal in response to biasing as the percentage change of PL intensity (ΔPL%). Each map represents the percentage change of PL after removing the electric field and returning the crystal to the initial 0V condition. (Details of the calculation are in Section 3.6.)

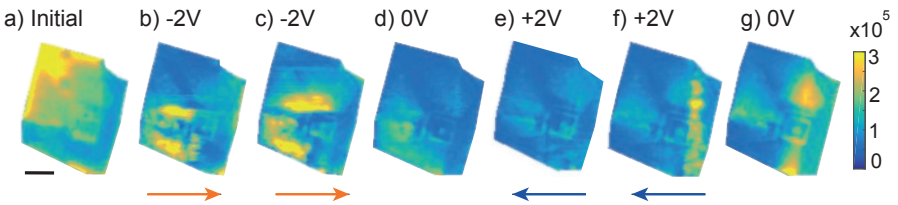

Figure 3.5: Spatially-resolved PL intensity maps. Each pixel of the each map is the integration of PL intensity at 500-580 nm. The bias condition is indicated above each map, and the direction of the electric field is indicated below with arrows if applicable. Scale bar is 15 μm.

The orange and blue arrows on figures 3d and 3e, respectively, show the electric field that the crystal experienced before collecting the PL maps. Comparing the relative changes with the direction of the electric field, one sees that the PL intensity increases in the region that experienced higher potential (see the red regions at left side Figure 3.4d and right side Figure 3.4e), and decreases in the region that was previously at lower potential (see the blue regions at right side Figure 3.4d and left side Figure 3.4e). This anti-correlation between electrodes A and B after bias mirrors the trend seen in XRF. The bias-dependence of the local photoluminescence is confirmed in $CH_3NH_3PbBr_3$ crystals deposited onto different electrodes (Au-Au and Au-Ti electrodes) as shown in the SI (Figure 3.11), indicating that the changes in PL are independent of the particular metal/perovskite interface. In all cases, the peak of the PL spectrum does not shift in energy significantly (less than 2 nm) between the Br-rich and Br-poor regions (see SI, Figure 3.12).
The changes in PL intensity may be explained by vacancy-mediated halide migration. Initially, the PL intensity was inhomogeneous across the single crystal as seen in Figure 3.5 suggesting that surface or bulk defects dominate the PL response. Upon applying bias across the crystal, it is observed that Br^- moves opposite to the direction of the electric field and the local PL increases where Br increases. This enhanced PL in bromide-rich regions may originate from three distinct but related mechanisms, triggered by the ionic migration as seen in the XRF maps (schematic of mechanisms in Section 3.3). First, bromide migration will lead to local changes in

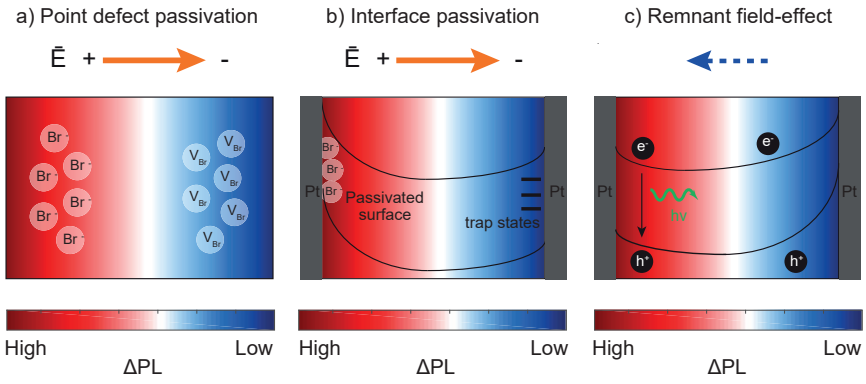

Figure 3.6: Schematic of mechanisms that can explain the observed PL intensity variation. At the positive (negative) electrode, Br^- migration may **a)** reduce (increase) a vacancy-related, recombination active point-defect concentration, or **b)** passivate (expose) surface states at the contact interface. Alternatively, **c)** the remnant field due to slow ionic back-diffusion after the electric field is removed may leave a narrower (wider) depletion region.

the bromide vacancy concentration, which has been proposed to play an important role in the photoluminescence quantum yield [104, 233, 251]. Crystal point defects such as vacancies may act as non-radiative recombination centers; therefore, a higher Br^- vacancy concentration could lead to lower radiative recombination efficiency, causing the band-to-band PL intensity to decrease. Second, bromide stoichiometry may play a role in the density of interface states at the contacts. The migration of the bromide away from the contact interface at the lower potential electrode may lead to a higher density of interface states, and at the other contact, the higher Br content may passivate interface states. Finally, ionic migration will cause some residual change in the potential at the perovskite/metal contact interface even after the electric field is removed, due to slow ionic diffusion. At the lower-potential contact the perovskite/metal interface behaves as in reverse bias: the residual change in potential increases the depletion region, which helps to split the photogenerated carriers and prevents them from recombining radiatively, suppressing PL intensity. At the higher-potential contact the interface behaves as in forward bias: the depletion region becomes smaller and PL intensity is enhanced. Further studies are necessary to quantify the relative importance of each mechanism. Self-trapped carriers in the crystal lattice (strong-coupled polarons) have been suggested to play a role in charge carrier dynamics of hybrid perovskites and affect the radiative recombination rate [252]. In the case of polaron formation, a red-shift in the energy of the PL peak is expected, but no red-shift was resolved within the detection limit of the PL setup in this study (see Figure 3.12, SI). Continued detailed study of ionic migration is critical because vacancies, as inherent material defects, may act as mediator or direct participants in non-radiative recombination centers in $CH_3NH_3PbBr_3$.

3.4 DFT calculations of ionic migration energy

The experimentally observed changes in Br concentration in the $CH_3NH_3PbBr_3$ single crystal are substantiated by the low energetic barrier to migration of Br^- - found by DFT climbing-image nudged elastic band (CI-NEB) calculations. To elucidate the ionic migration mechanism under applied bias, CI-NEB calculations were performed using $2 \times 2 \times 2$ supercells (computational details in SI). CI-NEB is a common method for finding minimum energy paths for ion migration [253–255]. A single positively-charged Br^- vacancy (V^+_{Br}) was introduced, and overall charge neutrality was achieved via a compensating background charge. We find that the lowest energy configuration for pristine $CH_3NH_3PbBr_3$ is in which the polar methylammonium cations are aligned, which is the expected orientation under an applied bias [228, 234]. This alignment of the MA cations breaks the cubic symmetry, resulting in three distinct migration paths for Br^-, which are shown in Figure 3.7.

The energy-migration coordinate diagram and the corresponding pathways viewed in a supercell are presented in the SI (see Figure 3.14). The paths where the Br^- moves with a component in the direction of the C-N bond alignment, denoted as B-C-B and B-A-B, show the lowest migration energy barriers of 227 meV and 306 meV, respectively. The other hop, C-A-C, shows a migration energy of 425 meV. The alignment of the $CH_3NH_3^+$ cations under bias appears to create a channel with a lower energy of Br^- vacancy migration along the field direction. In the absence of an electric field, this lowered barrier will be averaged out as methylammonium ions are randomly oriented at room temperature per $CH_3NH_3PbBr_3$ single crystal shown by neutron diffractometry [256]. Halide migration appears to benefit from $CH_3NH_3^+$ alignment that results in a lower migration energy barrier under an applied bias. The migration, in turn, is correlated with the density of recombination active defects as evidenced by the changes seen in the photoluminescence response under bias.

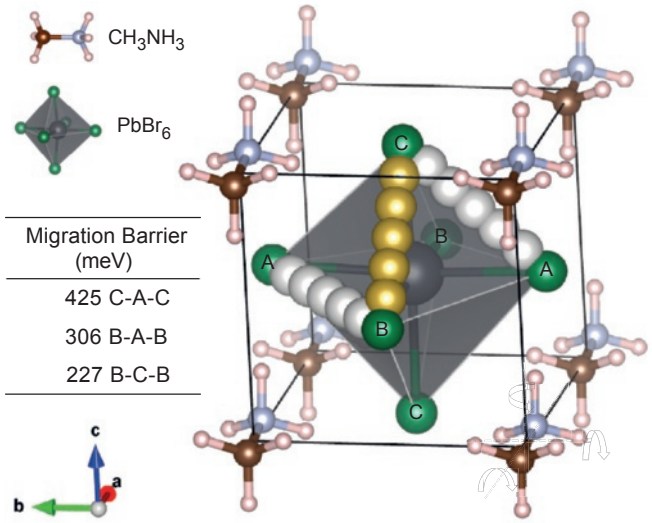

Figure 3.7: Schematic of Br^- diffusion pathways in $CH_3NH_3PbBr_3$ by nudged elastic band (NEB) The $PbBr_6$ octahedron becomes distorted after NEB relaxation. Primitive cell has lattice constants of 6.017, 6.041, and 6.115 rA, along the *a-*, *b-*, and *c-axis*, respectively. The geometrically distinct Br atoms are labeled as A, B and C and the corresponding migration energy barriers between Br atoms are shown in the table. White spheres represent the interpolated Br trajectories along pathway B-A-B and C-A-C, while yellow spheres indicating the smallest barrier migration for pathway B-C-B.

3.5 Conclusion

In summary, we systematically manipulate the halide concentration laterally within a thin $CH_3NH_3PbBr_3$ single crystal by applying a voltage bias. We observe the changes of Br distribution at the nanoscale by means of Nano-XRF. The halide migration is directly correlated to variations in PL response. As Br^- migrates away from the negatively biased electrode and the perovskite becomes locally sub-stochiometric, the PL intensity decreases. NEB calculations indicate that the alignment of the methylammonium cation under bias forms channels that facilitate halide migration along the field direction. Combining the quantitative analysis of ion migration with local optoelectronic characterization provides insight into the fundamental operation of halide perovskite devices. The link between intrinsic point defect migration and photoluminescence intensity makes it clear that controlling the crystal chemistry is paramount. Possible strategies to mitigate the effects of Br migration and improve optoelectronic performance in the perovskite include growing perovskites in halide-rich conditions [257] or applying post-growth treatments to lower the concentration of halide vacancies. Future work is needed to understand the defect kinetics of ion migration as a function of the absorber chemistry and to reveal the nature of the optoelectronic defects that arise under bias to achieve the full potential of the hybrid perovskite materials for optoelectronic devices.

3.6 Supplementary Information

3.6.1 Experimental details

In this study, we used the same method for the fabrication of perovskite precursors, solution and PDMS-stamped $CH_3NH_3PbBr_3$ single crystal devices as explained in Chapter 2 (See Section 2.6.1 for more details)

Synchrotron-Based XRF Characterization

In order to determine the elemental distribution in the absorber, the perovskite crystals were investigated by synchrotron-based nano-XRF with a 250 nm full-width half-maximum focused beam at 13.6 keV with a 50% aluminum absorption filter in place at beamline 2-IDD in a helium environment of the Advanced Photon Source at Argonne National Laboratory.
Fly-scanning was used with a dwell time per point of 100 ms. Using the beamline's nanopositioning stage, we scanned the sample in front of the focused X-ray beam and precisely mapped the local Pb and Br chemistry with a step size as small as 200

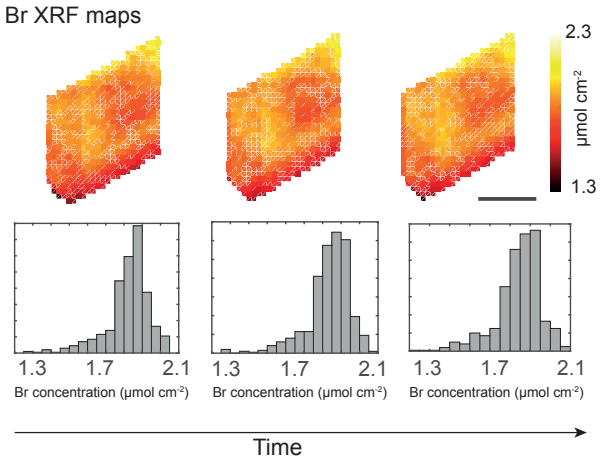

Figure 3.8: XRF maps of a $CH_3NH_3PbBr_3$ crystal with full beam illumination without electric bias. The Br XRF maps with the corresponding histograms are shown. The length of the scale bar is 5 µm. The mean and standard deviation for Map a, b and c are 1.82±0.12, 1.83±0.12, and 1.84±0.11 μmol/cm^2, respectively

nm. An SRS 570 current pre-amplifier at the beamline was used to bias the sample in-situ +/- 2V.

$CH_3NH_3PbBr_3$ stability was examined under focused X-ray beam at 13.6 keV with no filter in place (Figure 3.8). Br:Pb elemental ratio XRF maps indicate good stability of the material with no systematic change in its elements spatial distribution upon repetitive scanning with 100 ms dwell time per point. In our analysis, we focus on the quantitative Br:Pb ratio. NIST standard reference material 1832 and 1833 standards were used to quantify the XRF data, correcting for the uncertainty in the extrapolation of the fluorescence yield to the Br line using the initial perovskite stoichiometry. Additional XRF maps of quantitative Pb:Pt and Br:Pt mass ratio are presented in Figure 3.9. Linear color scale is applied to each elemental ratio, where yellow indicates high mass ratio and red indicates low mass ratio.

Analysis of spatially resolved PL maps of different $CH_3NH_3PbBr_3$ crystals

A WITec alpha300 SR confocal imaging microscope was used to collect photoluminescence spectra of $CH_3NH_3PbBr_3$ crystals while the crystal was being moved using a piezostage. Sample was excited with a 405 nm diode laser (Thorlabs S1FC405) through a NA 0.9 objective and the luminescence was collected in reflection using a spectrometer. The calibration of the spectral response of the collection optics, fiber, and spectrometer was done with a standard mercury light source, and the

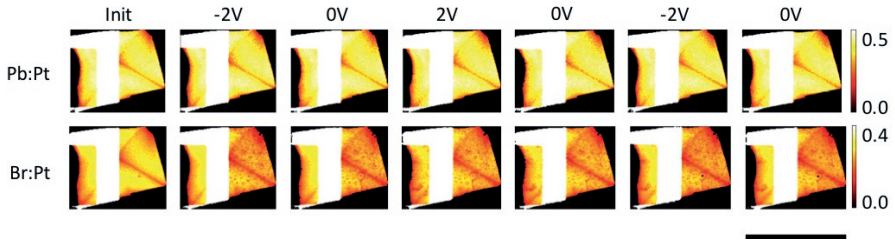

Figure 3.9: Pt:Pb and Pt:Br mass ratio XRF maps within the $CH_3NH_3PbBr_3$ crystal. The elemental ratio in each row has the same linear color scale. The scale bar is 33 μm.

spectrum was corrected accordingly. The spatially-resolved PL maps are obtained by integrating the PL intensity within the optical fluorescence peak width, from 500-580 nm. The relative changes of PL intensity (ΔPL) is computed using Equation (3.2),

$$\Delta^X(\%) = \frac{PLI^X - PLI_{initial0V}}{PLI_{initial0V}} \times 100 \tag{3.2}$$

where PLI is the photoluminescence intensity and X indicates the number of map according to Figure 3.5. All the relative PL maps of the crystal in the Figure 3.4 are shown in Figure 3.10.

Additionally, the PL maps of MAPbBr3 crystals on Au-Ti and Au-Au paired electrodes are shown in Figure 3.11. These maps display similar trends of PL intensity shifts under the influence of bias to the Pt-Pt electrodes shown in Figure 3.4.

The PL mapping experiment was also done on the crystal that was exposed to the X-ray beam during XRF mapping, and its the PL spectra were comparable to those of a fresh crystal (Figure 3.12k and l) with the PL peak being blue shifted by 10 nm.

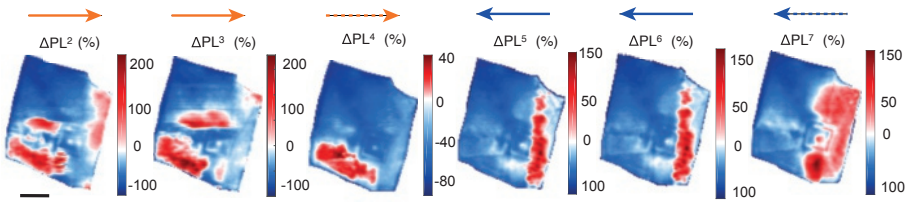

Figure 3.10: Relative PL maps of the crystal in different bias conditions compared to the initial 0V map. ΔPL_4 and ΔPL_7 are the same as maps shown in Figure 3.4d and e, respectively. The dashed arrows show the direction of the electric field that the crystal was under priorly. The total time to collect each map was 30 min. Scale bar is 10 μm.

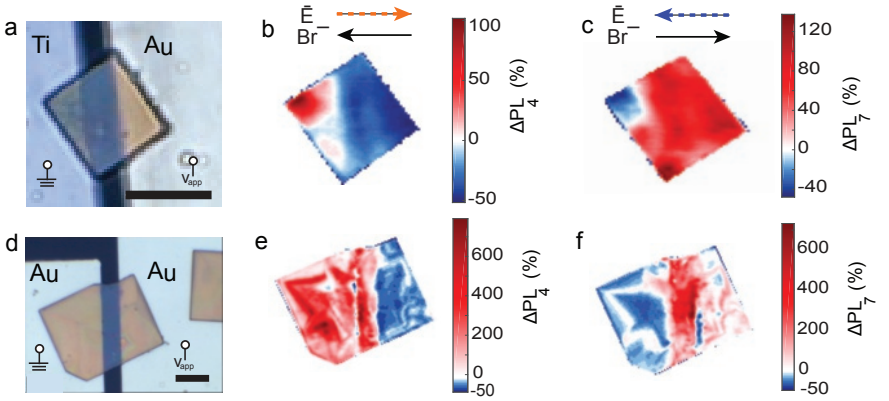

Figure 3.11: Series of relative PL maps for $CH_3NH_3PbBr_3$ crystal on Au-Ti (a-c) or Au-Au electrodes (d-f). The trend of an increase in PL intensity in the opposite direction of electric field is independent of electrode material. **a)** optical image of the crystal sitting on the gap between Au-Ti electrodes. **b)** relative PL intensity map of the crystal after applying -2V bias. **c)** relative PL intensity map of the crystal after applying +2V bias. **d)** optical image of the crystal sitting on the gap between Au-Ti electrodes. **e)**relative PL intensity map of the crystal after applying -2V bias.**f)**relative PL intensity map of the crystal after applying +2V bias. The arrows on top of each column show the direction of electric field and expected direction of Br^- movement. Scale bar is 10 μm.

A similar trend in PL intensity shift with electrical biasing is seen for this crystal, although the change in PL intensity is not as clear as it is for the fresh crystals (Figure 3.13). Synchrotron X-ray irradiation has been shown to degrade carrier collection in hybrid perovskites within seconds of exposure at a single spot [242], and it is thus not surprising that the PL changes are more clear in the fresh crystal.

3.6.2 Climbing-image nudged elastic band (CI-NEB) calculations

All DFT calculations were performed using the Vienna Ab initio Simulation Package (VASP) [258] within the projector augmented-wave approach [259]. Spin-polarized calculations using the Perdew-Burke-Ernzerhof (PBE) generalized-gradient approximation (GGA) [260] functional were used for structure relaxations and all analyses were carried out using the Python Materials Genomics (pymatgen) library [261]. We performed climbing image nudged elastic band (Cl-NEB) calculations using $2 \times 2 \times 2$ supercells (8 formula units) of the lowest energy structure obtained for cubic $CH_3NH_3PbBr_3$ to minimize the interaction between periodic images. To study Br^- vacancy migration, a single positively-charge Br^- vacancy (V^+_{Br}) was introduced and overall charge neutrality was achieved by

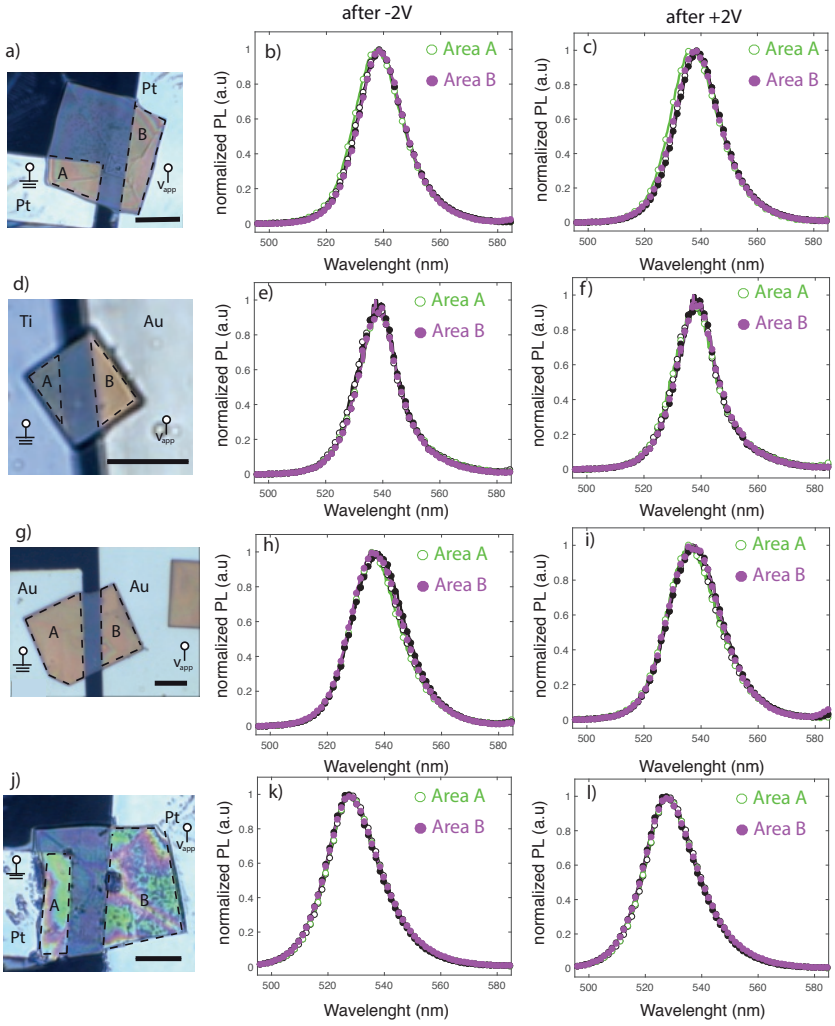

Figure 3.12: Normalized PL spectra of $CH_3NH_3PbBr_3$ crystals with different electrodes shows that the energy of PL peak does not vary upon applying electric field. The first column shows the optical image of the tested crystals on different electrode materials. Areas A and B are shown with dashed line on each figure. Second column presents normalized PL spectra after -2V poling for selected regions A and B. Third column shows normalized PL spectra after +2V poling for selected regions A and B. Scale bar is 10μ m.

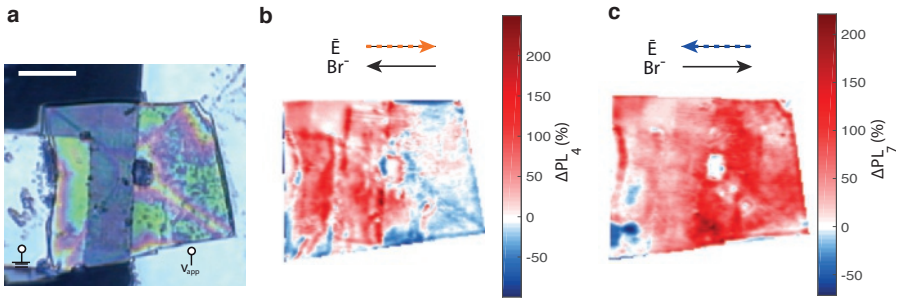

Figure 3.13: Percentage changes of PL intensity of the of $CH_3NH_3PbBr_3$ crystal after XRF measurement. **(a** optical image of the crystal. **b)** and **c)** are relative PL maps after -2V and +2V poling respectively Scale bar is 10μ m.

compensating background charge. A 2 × 2 × 2 k-point grid and energy cutoff of 520 eV were adopted for NEB calculations. The forces were converged to 0.05 eV/$\mathring{A}$.

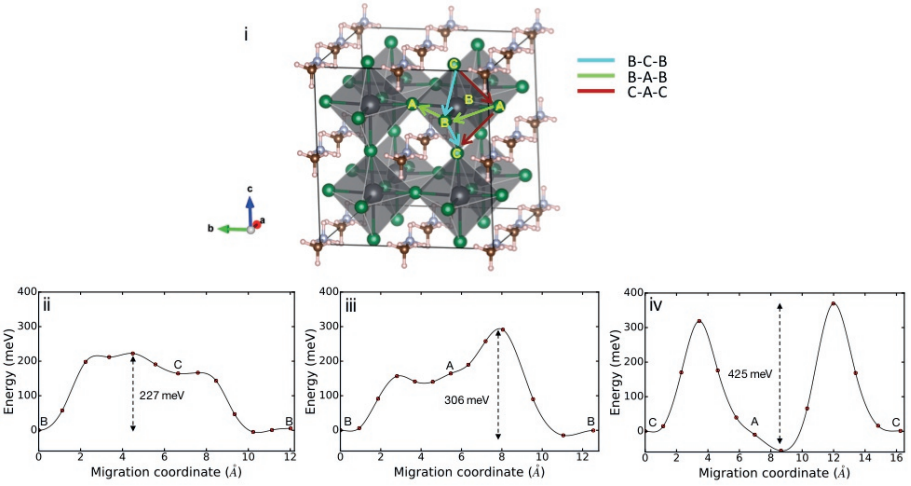

Figure 3.14: PBr- migration barriers from nudged elastic band (NEB) calculations. **(i** The migration paths depicted in the 2x2x2 super cell with paths labelled as B-A-B, B-C-B and C-A-C (labelled as in Figure 3.7 The energy vs migration coordinate of each path is shown: **ii)** B-C-B, **iii)** B-A-B **iv)C-A-C**

4

Perovskite nanowire extrusion

The defect-tolerance of halide perovskite materials has led to efficient optoelectronic devices based on thin-film geometries with unprecedented speed. Recently, ordered vertical arrays of perovskite nanowires have been realized, which can benefit from nanophotonic design strategies allowing precise control over light propagation, absorption, and emission. An anodized aluminum oxide template is used to confine the crystallization process, either in the solution or in the vapor phase. This approach, however, results in an unavoidable drawback: only nanowires embedded inside the AAO are obtainable, since the AAO cannot be etched selectively. The requirement for a support matrix originates from the intrinsic difficulty of controlling precise placement, sizes, and shapes of free-standing nanostructures during crystallization, especially in solution. Here we introduce a method to fabricate free-standing solution-based vertical nanowires with arbitrary dimensions. Our scheme also utilizes AAO, however, in contrast to embedding the perovskite inside the matrix, we apply a pressure gradient to extrude the solution from the free-standing templates. The exit profile of the template is subsequently translated into the final semiconductor geometry. The free-standing nanowires are single crystalline and show a PLQY up to ~29%. In principle, this rapid method is not limited to nanowires but can be extended to uniform and ordered high PLQY single crystalline perovskite nanostructures of different shapes and sizes by fabricating additional masking layers or using specifically shaped nanopore endings.

4.1 Introduction

Solution-based halide perovskite materials have attracted tremendous attention over the last five years. They show great potential for optoelectronic devices, such as solar cells and light-emitting diodes among other applications [84, 262]. While most research efforts have focused on thin-film geometries, highly ordered nanostructure array geometries have attracted less attention, even though nanophotonic design strategies could allow precise control over light propagation, absorption, and emission[263–271]. For example, while several reports exist on the formation of perovskite nanowires [45, 123, 127, 167, 170, 171, 178, 182, 272–278] , only a few of them show highly ordered vertical array geometries, which are of prime importance for large-scale device applications [182, 276–278].

Only recently, ordered vertical perovskite nanowire arrays inside anodized aluminum oxide (AAO) templates have been realized [182, 276–278]. In these studies, the AAO confines the crystallization process in either solution or vapor phase and therefore completely determines the cross-section and length of the final nanostructures. Since the AAO cannot be removed selectively, because of the sensitivity of perovskites to etchants, the nanowires remain embedded inside the AAO and are not free-standing arrays. Also, the geometries achievable with this approach are limited to what can be obtained in AAO.

In general, synthetic methods for making free-standing solution-based nanostructure arrays with arbitrary cross-sectional shapes and sizes are currently lacking. This limitation can be explained by the intrinsic difficulty of controlling the precise placement and form factors of free-standing nanostructures during crystallization from solution.

In this chapter we introduce a method to fabricate nanostructure arrays with arbitrary dimensions directly from solution. As proof of this concept, we show the fabrication of vertical free-standing $CH_3NH_3PbBr_3$ perovskite nanowires. The scheme utilizes AAO templates to confine the precursor solution into highly ordered nanopores with narrow size distributions. In contrast to techniques that embed the perovskite inside the AAO, the solution is extruded from the free-standing templates, driven by a small pressure gradient of 50-100 mbar versus atm. At this stage the formation of the nanowire-shaped intermediate crystal phase is initiated by more rapid evaporation of the solvent near the pore exits and the confinement of the solution. The pore exits therefore determine the dimensions of the nanostructures. After annealing, highly uniform free-standing perovskite nanowires with a wide variety of dimensions are obtained. Transmission electron microscopy (TEM) diffraction shows single crystallinity along the nanowire length. Photoluminescence quantum yield (PLQY) measurements on single nanowires reach values of ~29%, which are in line with values for the respective $CH_3NH_3PbBr_3$

thin-films [44, 104, 279].
In principle, this novel method is not limited to nanowire arrays but could be extended to a large variety of highly uniform and ordered high PLQY single crystalline perovskite nanostructures. Different shapes and sizes could be obtained by fabricating additional masking layers or using specifically shaped nanopore endings [280]. The concept of the fabrication process is very similar to macroscopic profile extrusion in the plastics industry, however, for a nanoscale optoelectronic material. The unprecedented simplicity and high speed make it therefore a highly promising approach for the industrial fabrication of novel optoelectronic devices based on high PLQY nanostructured arrays.

4.2 Fabrication of nanowires via AAO templates

Figure 4.1 shows the fabrication scheme. In the first step the $CH_3NH_3PbBr_3$ solution (3M in dimethyl sulfoxide, DMSO) is dropcast onto a free-standing AAO template (30-50 μm thick), which rests on an O-ring on top of a PDMS block. AAO is a well-known template for nanostructuring and allows control over pore size and shape from hundreds of nanometers down to around 5 nm on a wafer scale and even in binary array geometries [280–285]. By selectively etching the supporting aluminum substrate, free-standing AAO templates with double-sided pore access can be obtained [286, 287]. To facilitate the filling of the AAO pores with the perovskite solution, a low-pressure region is formed in the sealed air compartment between the AAO and the PDMS. We used a simple syringe connected via a plastic tube to establish the pressure gradient of 50-100 mbar versus atm when pulling the piston of the syringe. In general, any method to control the pressure can be utilized. Driven by the pressure gradient across the membrane, the perovskite solution rapidly fills the AAO pores and extrudes out of the AAO template on the bottom (inset in Figure 4.1a). The time of extrusion depends directly on the pressure gradient applied and the dsired length of final nanowires. In the next step, the template is carefully transferred onto glass spacers positioned on a hotplate and annealed at 120 °C to form the perovskite crystals (Figure 4.1b). Figure 4.1c shows schematically the final AAO template with the extruded free-standing nanowires. Finally, we dry-transfer the single perovskite nanowires to different substrates (glass, silicon, TEM grids) for subsequent characterization. We have used the same AAO templates numerous times, simply by dissolving the residual perovskite inside the pores with DMSO and rinsing in acetone and isopropanol followed by prolonged annealing. Therefore, the requirements for a reusable substrate scheme, e.g. by embedding the array nanostructures into a polymer layer followed by mechanical peel-off, are easily met.
In order ot understand the mechanism of nanowire formation and determine if

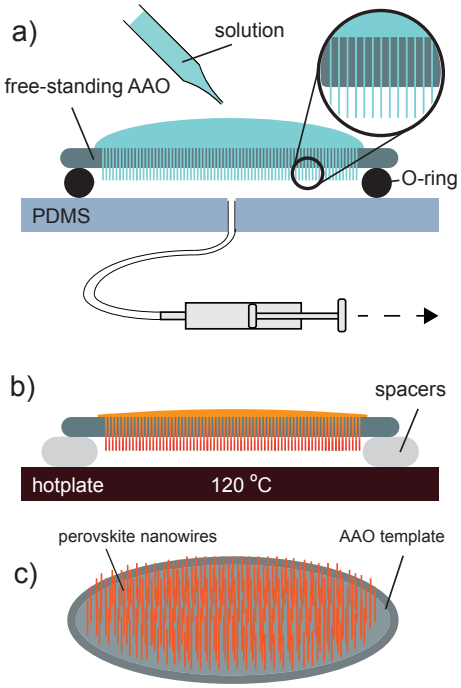

Figure 4.1: Perovskite nanowire extrusion scheme. **a)** $CH_3NH_3PbBr_3$ solution (3M in DMSO) is dropcast onto an AAO template placed on an O-ring on top of a PDMS block. A low pressure region is formed in the sealed air compartment between the AAO and the PDMS block with a glass syringe connected via plastic tubing. After a short time the perovskite solution fills the AAO pores and extrudes out of the AAO template on the bottom (inset). **b)** The template is carefully transferred to a hot stage and annealed. **c)** The final AAO template with extruded free-standing nanowire arrays.

the nanowire shape formed before or after the final annealing step, we carefully break off the nanowires and transfer them to a different substrate before annealing. Figure 4.2 shows the resulting structures which is an intermediate crystal phase probably consisting of $CH_3NH_3PbBr_3$ and DMSO formed in the nanowire shape right at the extrusion stage. Such intermediates have been reported previously [288–291]. The crystallization of the intermediate is likely due to preferential evaporation of the solvent from the pore exit and the solution confinement inside the AAO pores. The wires of the intermediate appear to have largely varying diameters. We ascribe this fact to merging of multiple nanowire during the break-off process. Figure 4.2b shows a part of the substrate which was still partly covered in DMSO. Interestingly, the wire-like intermediates are clearly visible in the bottom part of the image, even though they are embedded in DMSO. At the solvent front on the upper

part in the image, cubic perovskite crystals can be seen. After a short annealing for 5 min at 120°C we find the complete transformation of the wire-like intermediate into cubic crystals, as can be seen in Figure 4.2c. As has been noted before, due to the interaction with the substrate, the intermediate crystal structure rearranges into cubic crystals during the final perovskite formation. Therefore, the AAO template not only guide the shape of the intermediate into the nanowire form, but also stabilizes the structure during the final transformation from the intermediate phase into the perovskite crystal.

Figure 4.3 shows extruded free-standing vertical perovskite nanowires covering a wide area of the AAO surface. The length of the nanowires is dictated directly by the time and magnitude of applied pressure gradient to the template. As shown in the inset of Figure 4.3a nanowire are shorter when applying the pressure gradient for a shorter time. While our current results serve as a proof-of-concept, further optimization is necessary to improve the wire-to-pore ratio, diameter distribution and nanowire length. In this study, two different types of AAO templates were used: custom-made ordered templates with pore size of 250 nm (pitch 1 μm) (Figure 4.3a and b) and commercially available semi-ordered templates with average pore sizes of 200 nm (pitch 470 nm) (Figure 4.3c and d). The pitch-to-pore ratio serves as a crucial parameter in realizing nanowire arrays; for ratios smaller than ~4 the extruded nanowires coalesce (see Section 4.6). In order to increase the initial ratio the pore sizes of the semi-ordered templates were shrunk down by subsequent atomic layer deposition of alumina (see supporting information). We observed an increase in diameter compared to the AAO pore exit, which we attribute to a non-ideal contact angle between the pore wall and the back surface of the template,

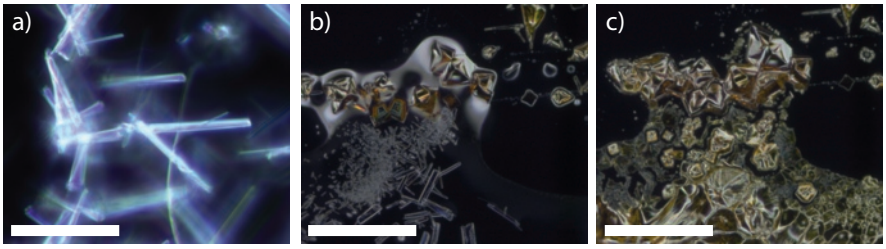

Figure 4.2: Optical microscopy images of intermediate crystal phase. a) Dark-field image of intermediate crystal phase in nanowire shape. **b)** Dark-field image of the wire-like intermediate broken off after extrusion through AAO template and before annealing. A few perovskite crystals formed already at this stage. **c)** Dark-field image after annealing of the same region than in b). As has been noted before, the nanowire shape of the intermediate is unstable on a glass substrate, in contrast to cubic crystals (compare upper parts of b) and c)). Scale bars are 10 μm, 20 μm and 20 μm for a)-c), respectively.

which leads to partial surface wetting around the pore instead of immediate extrusion. With increasing time of mechanical polishing to obtain a 90° angle, we observed a decreasing discrepancy between pore exit and the final nanowire diameter. The single nanowires were transfered to other substratets such as silica, TEM grid and silicone for furthere characterization by sliding carefully the substrate on top of the template (Figure 4.4). The thin wires were used for TEM studies, while the thick nanowires fabricated from ordered AAO templates were used for PLQY measurements, as described further. Figure 4.4a,b show a nanowire with a length of ~20 μm, originating from a template which was exposed for a longer time to the pressure gradient. The SEM images demonstrate high geometric uniformity and absence of any apparent surface disorder on the nanowires. Figure 4.3b and d show optical dark-field images taken from the vertical nanowire arrays fabricated with ordered and semi-ordered AAO templates respectively. In Figure 4.4c an optical dark-field image of single nanowires is shown, which supports the high uniformity of the wires by absence of strong optical variations along the length or in between nanowires, e.g. due to changing optical resonances because of variations in diameter [292, 293].

4.3 Single crystallinity of perovskite nanowire

To obtain crystallographic information, we performed transmission electron microscopy (TEM) diffraction on single perovskite nanowires and X-ray diffraction (XRD) measurements on a whole template. Figure 4.5a shows a bright-field image of a wire with the green marked regions (I, II, III) indicating the locations of selected-area diffraction measurements, as shown in Figure 4.5b-d, respectively. The same diffraction spot pattern can be clearly seen along the length of the wire, confirming it is a single crystal. Furthermore, all the measured wires via TEM diffraction showed a <100> growth direction for the cubic symmetry. The obtained lattice constant of a=5.85(5)$\mathring{A}$ is in agreement with previously reported values for $CH_3NH_3PbBr_3$ perovskite (a=5.92 $\mathring{A}$) [189, 233]. Besides the 0.5-1% difference between the measured and the literature value of the lattice constant we observe a set of symmetric diffraction spots not originating from the perfect cubic lattice, but which can be explained by a slight tilt of the octahedra in the crystal structure [294, 295]. Therefore, we attribute the difference in lattice constants to a deviation from the perfect cubic crystal phase [295].
During electron beam exposure we observed degradation of the perovskite crystal, as already noted by others [239]. The exposure resulted in a continuous conversion to polycrystallinity, i.e. the evolution of diffraction rings from distinct spot patterns with increasing exposure time which prevented perfect alignment to the zone axis. Figure 4.6a-c show bright field images of the same nanowire with marked regions

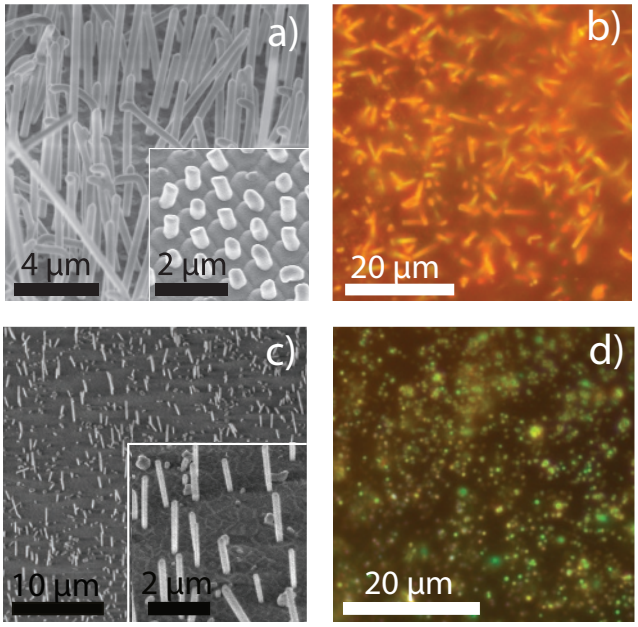

Figure 4.3: Electron and optical microscopy images of extruded perovskite nanowires. a) SEM image of vertical nanowire array made with ordered AAO template. Inset shows shorter nanowires that have been obtained by exposing the template for shorter times to the pressure gradient. **b)** Optical top view dark-field microscope image of the array in (a) under white light illumination. **c)** SEM image of extruded nanowire arrays from semi-ordered arrays. **d)** Optical top view dark-field microscope image of the array in (c).

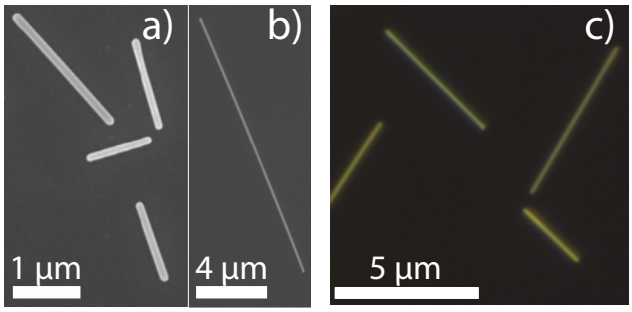

Figure 4.4: Electron and optical microscopy images of single perovskite nanowires. a) Higher magnification SEM images of single horizontal perovskite nanowires with different wire lengths. **b)** Optical dark-field microscope image of single nanowires.

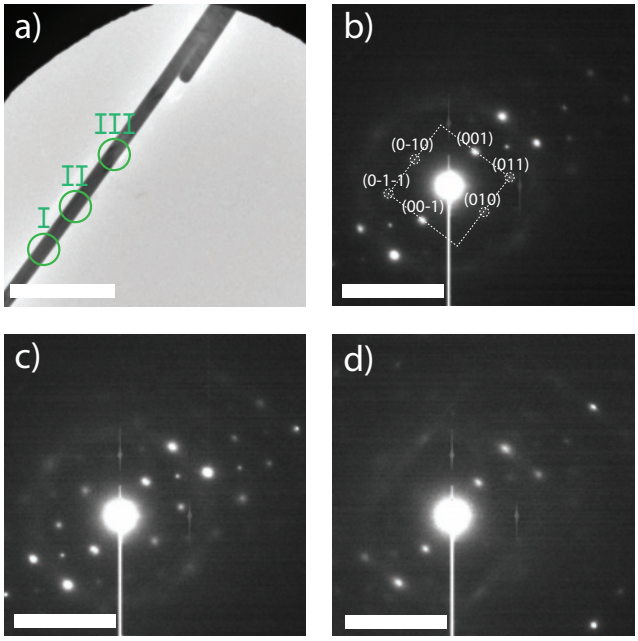

Figure 4.5: TEM single nanowire diffraction. **a)** Bright-field image of a single perovskite nanowire. **b-d)** Diffraction images of the regions I-III marked in a), respectively. The same diffraction spot pattern can be clearly seen along the length of the wire, confirming a single crystal phase. The obtained lattice constant for the wire, a=5.85(5) $\AA$, is in agreement with the literature value of $CH_3NH_3PbBr_3$ perovskite (a=5.92$\AA$) [189]. The scale bars in a) and b)-d) are 2 μm and 2 nm-1, respectively.

d-f for which the diffraction is shown , respectively. Figure 4.6g-i present bright field images of another nanowire and the formation of a granular contrast with prolonged exposure. The granular contrast is likely due to the observed polycrystallinity, as shown in f. Noteworthy, the transformation from the single into the polycrystalline structure is mostly initiated at the contact points with the Au TEM grid which points towards a charge-assisted degradation mechanism.

The X-Ray diffraction (XRD) measurements confirm the dominance of the <100> growth direction over the whole template, as showin in Figure 4.7. When XRD is conducted on assembles of nanowires extruded with ordered AAO, the (100) and (200) crystal planes present the strongest diffraction peaks, in agreement with the <100> growth direction of nanowires obtained from single wire TEM diffraction. Other diffraction peaks might originate from residual perovskite microcrystals formed on the AAO top surface during fabrication or slightly tilted nanowires.

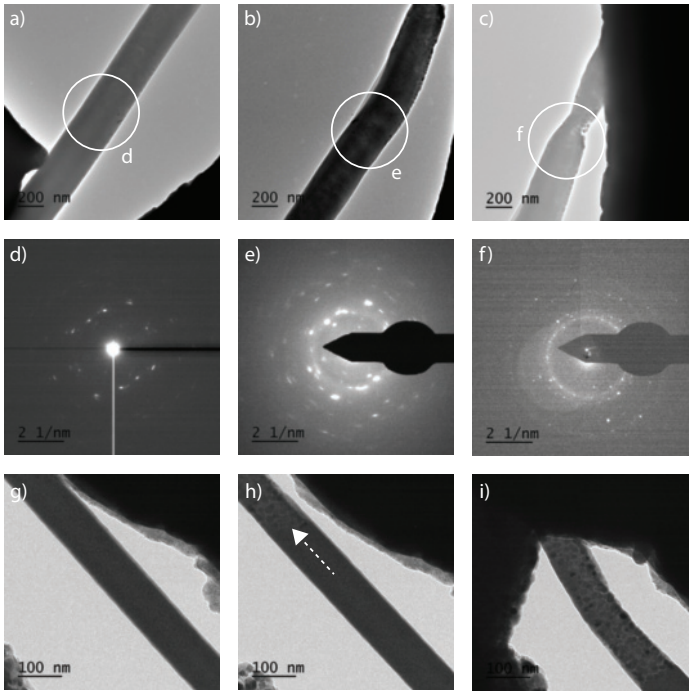

Figure 4.6: Electron beam-induced damage of perovskite nanowires. a-c) Bright field images of the same nanowire with marked regions d-f for which the diffraction is shown in Figure 4.5 **d-f)** The initially distinct diffraction spots change into rings during electron beam exposure. **g-i)** The initially distinct diffraction spots change into rings during electron beam exposure. **h)** the change originates from contact points with the TEM grid, as shown in **i**, which indicates a charging related degradation mechanism.

These results prove that highly uniform and single crystalline perovskite nanowires can be obtained with this novel nanowire extrusion method.

4.4 Optical properties of nanowire

To study the electronic and optical properties we performed photoluminescence quantum yield (PLQY) measurements .The PL spectrum in Figure 4.8a shows a peak centered at 535 nm, which is in agreement with previous reports for thin films of $CH_3NH_3PbBr_3$ [251]. To obtain spatially resolved PLQY measurements of single nanowires, we used integrating sphere microscopy [296, 297]. This technique allows us to determine quantitatively the spatially resolved absorptance, by

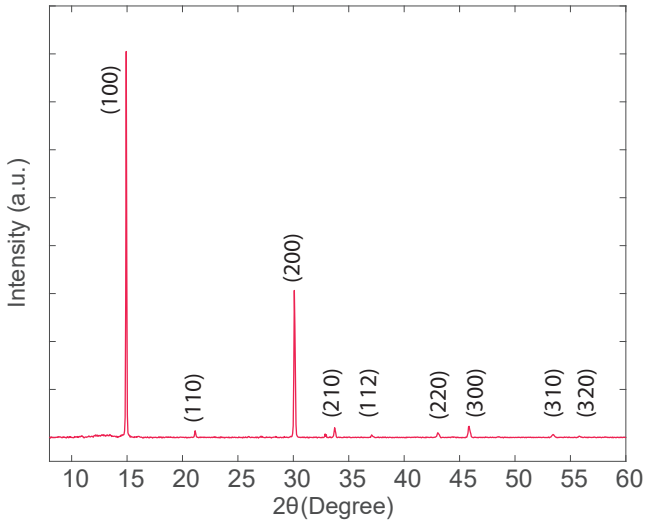

Figure 4.7: X-ray diffraction (XRD) pattern of perovskite nanowire array after extrusion through AAO template.

using an integrating sphere to measure all non-absorbed light and a glass sample holder on a piezo-stage to scan the sample across the laser beam. Additionally, by placing filters in front of the integrating sphere and reflection photodetectors, we can measure the photoluminescence quantitatively, as well. As a result, we can calculate the spatially resolved PLQY, i.e. how many photons are emitted per absorbed photon (see Section 4.6.2 for more details). As can be seen in Figure 4.8b, the PLQY has the highest value of 29.5% at the center of the nanowire while the average along the whole length is ~20%. The Average PLQY values were calculated from the PLQYs along the nanowire axis, and error bars are standard deviation from average. The PLQY experiment details is explained in Section 4.6.2. TEM measurements in Section 4.3 confirm the single-crystalline nature of these wires, while the PLQY shows deviations from the average value along the nanowire length Figure 4.8b. Given that the single-crystalline wire has no grain boundaries we suspect surface recombination and defect recombination from slight variations in stoichiometry or point defect density to be the main factors limiting the performance [104]. As discussed in Chapter 3 the inhomogeneous vacancy distributions in perovskite single crystals lead to inhomogeneous PL [298]. Given the emission of single crystal $CH_3NH_3PbBr_3$ nanowire here (Figure 4.8) we attribute the non-uniform PLQY map to the local variations in stochiometry.

To study the degradation behaviour of the nanowires in ambient conditions we

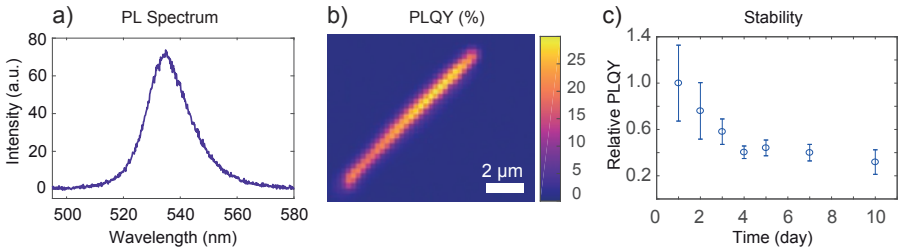

Figure 4.8: PLQY measurements of a single perovskite nanowire. a) Nanowire photoluminescence (PL) spectrum at the center of the nanowire with a peak centered at 535 nm. **b)** PLQY map at 1000 suns illumination intensity. **c)** Relative PLQY change from day 1. After 10 days the PLQY decays by ~70% from its initial value. The error bars are the standard deviation of the PLQY values along the nanowire.

measured the PLQY maps over a period of 10 days (Figure 4.9). The average PLQY decays within 10 days by ~70% from the initial PLQY of fresh nanowire at day 1. (Figure 4.8c)

The PLQY of the nanowire as a function of incident laser intensity (Suns) or generation rate was measured 3 days after fabrication (Figure 4.10) and shows a linear dependence with laser intensity (between 100 and 1000 suns), which can be explained by monomolecular recombination (Shockley-Read-Hall (SRH) or surface recombination)as the main limiting mechanism rather than radiative or Auger recombination (for detailed explanation of recombination mechanism please see Section 4.6.3) [297]. Therefore, we can extrapolate the PLQY down to 1 sun, which

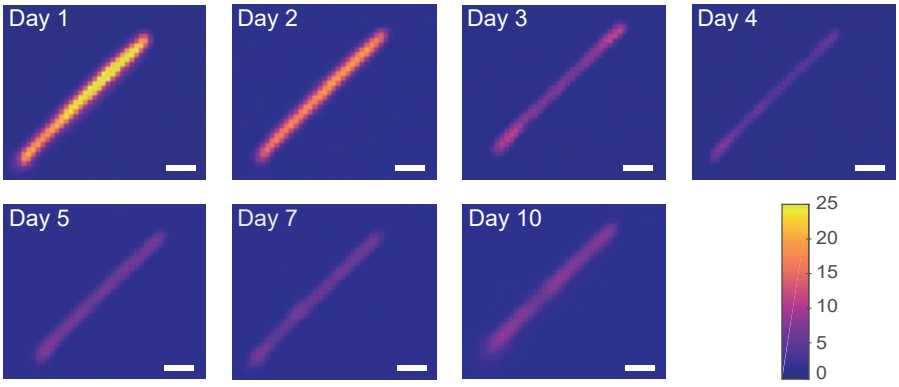

Figure 4.9: PLQY intensity maps (in %) as a function of time at 1000 suns intensity.

The scale bars are 2 μm

results in a value of ~1% for the measured wire, comparable to reported values of 3 for $CH_3NH_3PbBr_3$ thin-films with a 1:1 ratio (CH_3NH_3Br:$PbBr_2$) [104]. Given that the wire decayed from its PLQY value on day 1 we expect the PLQY at 1 sun to be initially higher.
We have observed lower PLQY values for nanowires extruded from freshly prepared solutions, while the higher values shown here come from extrusion of aged solutions. Such a variation suggests that the nanowire extrusion process has the same strong dependence on the exact preparation conditions of the precursor solution as has been observed in thin-films. Thin-film studies have concluded that preparation details including aging [299] and temperature [300] of the solution, solvent and precursors [301], precursors ratio [233], and ambient conditions [223, 302], all strongly influence the resulting material properties.

4.5 Conclusion and Outlook

In conclusion, solution-based nanostructure extrusion enables the fabrication of free-standing perovskite nanowire arrays. Our crystallographic and optical measurements show single crystallinity along the lengths of the nanowires and PLQY values of up to 29% for freshly made nanowires. This novel method can be general-

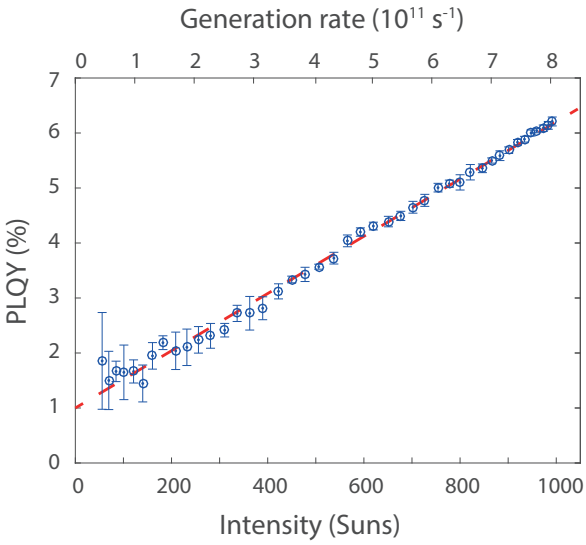

Figure 4.10: PLQY of the nanowire discussed Figure 4.8 as the function of incident laser intensity at day 3 after fabrication.

ized from nanowire arrays to other nanostructured shapes by altering the extrusion mask (Figure 4.11). Furthermore, provided the stability issues for perovskite based systems are resolved, e.g. by embedding the material in a flexible polymer encapsulation, the application extends potentially beyond research. The unprecedented simplicity and high speed of this novel nanostructure extrusion technique might be suitable for the industrial fabrication of nanostructured optoelectronic devices.

4.6 Supplementary Information

4.6.1 Experimental details

Preparation of Methylammonium Lead Bromide solution

The solution was prepared at room temperature and in ambient conditions. $CH_3NH_3PbBr_3$ was synthesized and recrystallized using a previously reported protocol [204]. The precursor $PbBr_2$ (Sigma-Aldrich, purity≥ 98%) was mixed with CH_3NH_3Br in a 1:1 molar ratio with DMSO (Sigma-Aldrich, anhydrous, purity≥ 99.5%) to obtain the 3M solution. The fresh solutions are heated up to 60 °C and stirred with a magnetic stirrer for $1\frac{1}{2}$ h. The solution could be used for the extrusion right away resulting in nanowires with PLQY < 5%, but was typically aged for 10-20 days at ambient conditions to allow for PLQY values of up to ~30%. Prior to use the solution was heated to 70°C while stirring.

Preparation of AAO templates

Two types of AAO templates were used for this study. The commercially available free-standing AAO templates were purchased from InRedox with pore size of 200 nm and pitch of 470 nm. Atomic layer deposition of 50 nm Al_2O_3 was performed on these templates to narrow down the pore diameter to about 100 nm. This way,

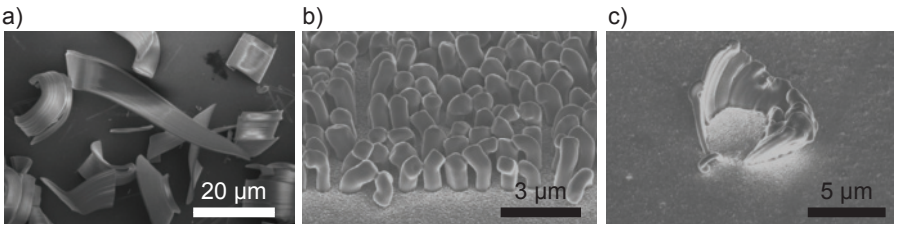

Figure 4.11: Various nanostructures fabricated with extrusion method, using a mask on top of the AAO template to change the shape of exit profile.

the spacing between two neighboring pores increased to avoid coalescence of individual nanowires into bundles. The final nanowire diameter is strongly influenced by the shape of the pore exit. Therefore, we mechanically polished the templates with polishing paper (4000, 6000 and 8000 grit) followed by a 10s HF (1%) etch and rinse in deionized to remove residual Al_2O_3 clogging the pores, with the side effect of slightly increasing the average pore diameter by about 20 nm. After the H_2O rinse, the templates were annealed for 2-3h at 250°C in air on clean glass slides. The final AAO templates had pore sizes of about 120 nm and provided nanowires with diameters of about 160 nm. This process unavoidably clogs some of the pores. Therefore custom-made ordered AAO templates were prepared. Specifically, Al foil was cut into 1.5 cm by 2.5 cm pieces and cleaned in acetone, isopropyl alcohol and deionized water with sonication, respectively. The foils were then electrochemically polished in a 1:3 (v:v) mixture of perchloric acid and ethanol for 150 s at 12.5 V and 10°C. The polished Al foils were then imprinted by 5 mm by 5 mm home-made silicon master (hexagonally ordered pillar array with height of 200 nm and pitches of 866 nm and 1000 nm) with a pressure of $\sim 2\times10^4$ N.cm^{-2} to initiate the perfectly ordered AAO growth. Thereafter, Al chips were anodized with a home-built anodization setup with voltage equal to pitch (nm)/ 2.5, and the anodization solution was made by mixture of 4 w.t% citric acid, ethylene glycol and 0.1 w.t% sulfuric acid with a ratio of 115: 115: 10 (v: v: v). The anodization was continued for 36 h to give an AAO thickness of ~40 μm. After that the AAO film was delaminated from the remaining aluminum by immersing the sample in over saturated $HgCl_2$. After aluminum was completely etched away, the sample was rinsed by acetone and then baked at 80°C. Then the bottom side of the freestanding AAO film was opened by ion milling with 85° tilted angle at 750 V for 2 h.

Pressure gradient and nanowire extrusion

To facilitate the filling and extrusion of the AAO pores by the perovskite solution, a pressure gradient of 50-100 mbar was applied across a 1 cm^2 AAO template, using an O-ring, a PDMS block and a syringe. A 5 ml syringe was connected via a plastic tube and hole in the PDMS block. Then the solution was dropcast onto the AAO top surface and the syringe was slowly pulled outwards at a rate of about 0.5 ml/s to maintain a pressure gradient. The extrusion took about 30s. While this procedure is suitable for a simple lab setup, a more controlled environment can be easily created with standard vacuum techniques. Due to the pressure gradient with the ambient, the perovskite solution slowly fills the whole AAO template until it reaches the AAO pore exit on the back. Subsequently, the templates were carefully transferred to glass spacers on a hot stage and annealed at 120°C for 10-90 min, depending on the amount of residual perovskite solution on the AAO top surface. We note that

the perovskite crystal structure is rapidly formed during the first few minutes of annealing, due to the evaporation of DMSO from the nanowire intermediate, and most of the annealing time is required to remove enough solvent from the template to avoid complication during the subsequent handling. To transfer the nanowires to different substrates (glass, silicon, TEM grid) for subsequent characterization, the wires were broken off by sliding the respective substrate over the AAO template.

TEM diffraction

The TEM diffraction measurements were done on a 300 keV TEM (FEI 80-300 Titan) at the Center for Advanced Materials Characterization in Oregon (CAMCOR). The selected-area diffraction aperture was 40 μm. A Au TEM grid was used to avoid chemical reactions of the perovskite nanowires with the grid.

4.6.2 Integrating spehere microscopy

Integrating sphere microscopy on single nanowires presents an ideal tool to study the influence of novel surface treatments and compositional variations on the electronic and optical performance of nanostructures, because it excludes inhomogeneity at the array level [296, 297]
In this study and also in Chapter 5 we measured the PLQY in a home-built integrating sphere microscopy setup, as depicted in Figure 4.12. The detail of the setup and measurement procedures are explained elsewhere [296]. In the IS microscopy all the light interacted with the sample can be measured quantitatively, and the absorptance of the sample is measured via the following equation:

$$A = 1 - \frac{R_s}{R_r} - \frac{IS_s}{IS_r} \tag{4.1}$$

where A is absorptance, R_s and IS_s are the signals detected by reflection photodetector and IS photodetector respectively, when the beam probes the sample and R_r and IS_r are the signals for reflection and transmission (IS) reference measurements respectively.
To distinguish between absorption and photoluminescence in the PLQY experiment we used short- and long pass filters with a cut off wavelength of 500 nm (Thorlabs FELH500 and FESH500) to measure the absorption and emission respectively. The filters were placed in front of the photodetectors as shown in Figure 4.12 and the scanning of the nanowire was repeated twice with each filters. The PL is then is then calculated from following equation:

$$PL = \frac{R_s}{R_r} + \frac{IS_s}{IS_r} \tag{4.2}$$

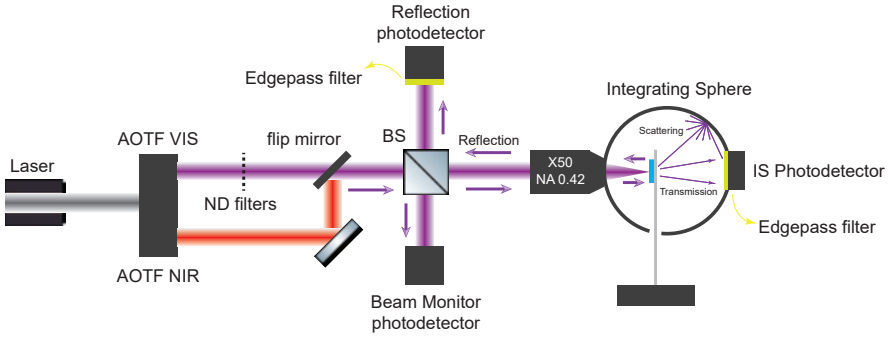

Figure 4.12: Optical setup

Reference measurements were performed here with the long pass filters in front of the photodetectors, where as reference measurements for absorption were done with the of shortpass filters. PLQYs were obtained by dividing the scanned map of emitted photons by the maximum number of absorbed photons, represented by following equation:

$$PLQY = \frac{PL}{A} \tag{4.3}$$

4.6.3 Intensity-dependent PLQY

In Figure 4.10 we showed that PLQY linearly increases with increasing the generated carriers in perovskite nanowires. The generation rate (G) is equal to total recombination rate in equilibrium. Three mechanisms contribute to the recombination dynamics of charge carrier in semiconductor [67]: (i) Monomolecular or trap-assisted recombination which involves one carrier (hole or electron) being trapped in the localized energy states within the bandgap. These localized states or deep-level traps are created by either impurities and lattice defects (Shockley-Read-Hall (SRH) process) or dangling bonds at the surface (surface states). (ii) Bimolecular recombination which associates with the band-to-band recombination of electrons and holes and emission of photons. Thus this mechanism is known as radiative recombination. (iii) Many-body process or Auger recombination in which an electron and hole recombine and give their energy to a third particle (electron or hole). Therefore G is:

$$G = R = An + Bn^2 + Cn^3 \tag{4.4}$$

Where n is charge carrier density, A is the monomolecular recombination rate co-

efficient, B is the radiative recombination rate, and C is the Auger coefficient. According to Equation (4.3), PLQY can be rewritten as:

$$PLQY = \frac{Bn^2}{An + Bn^2 + Cn^3} \tag{4.5}$$

If monomolecular recombination is dominant, we can simplify the above equation as:

$$PLQY = \frac{Bn^2}{An} = \frac{B}{A}n \tag{4.6}$$

Thus, linear relationship of PLQY with excitation intensity or generated carrier density reveals the dominance of monomolecular recombination, including SRH process and surface recombination.

5

Charge carrier dynamics at the Perovskite/Alumina interface

In the past few years, hybrid halide perovskites have been prominently used as active semiconductors in optoelectronics. However, like any other semiconductor, their high performance depends on the alleviation of the defects, especially on the surface. Passivation of the surface defects with metal oxides such as alumina is a common strategy in semiconductors to reduce the trap states at the surface. In this work we used perovskite nanowires embedded in anodized aluminum oxide templates as a well-controlled platform to study the charge carrier dynamics and effect of surface passivation with alumina. These $CH_3NH_3PbBr_3$/alumina nanowires had high charge carrier lifetimes of more than 20 ns. We developed a model to relate the charge carrier lifetimes with the nanowire radii. Using this model, we extracted a remarkably low surface recombination velocity (SRV) of 37.2 ± 20 $cm.s^{-1}$ for the perovskite/alumina interface which confirms the passivation role of alumina. Due to the ease of fabrication and excellent photophysical properties, the perovskite/alumina nanowires can be considered as a candidate for integration in optoelectronic device structures.

5.1 Introduction

Shockley-Read-Hall (SRH) recombination at the surface and in the bulk of semiconductors is detrimental for the performance of devices, especially at low charge carrier injection levels. The bulk and surface defects should be treated separately because the strategies to mitigate them in semiconductor technologies are different. Hybrid halide perovskites are also not an exception in this important matter and their efficient performance is tightly bound to tackling the right approaches for identifying and confronting their defects. The remarkable performance of halide perovskites is attributed to long charge-carrier diffusion length and lifetime, high absorption coefficient and high emission yields [13, 87, 108]. These characteristics are strongly dependent on the photophysical properties, specifically the charge carrier generation and recombination dynamics. Thus, it is crucial to provide in-depth understanding of how fast and via which channels the charge carriers recombine within the perovskite light-absorber. This knowledge assists in developing strategies to minimize the structural imperfections, such as bulk and surface lattice defects for designing highly efficient devices. In perovskite solar cells in particular, many interfaces exist in mesoscopic or planar device structure such as the interfaces of perovskite within mesoporous TiO_2 or Al_2O_3 scaffold, and with electron/hole transport layers (ETL/HTL). Interfacial defects and undesired doping at these interfaces facilitate the charge recombination processes and impact the overall performance of the device negatively[303].

Dangling bonds and interrupted lattice induce high density of charge traps at the surface. The presence of undercoordinated ions also causes the accumulation of excess charges which capture minority carriers and increase the recombination at the surface [304, 305]. Ultraviolet Photoemission Spectroscopy (UPS) measurements exhibited the presence of below-gap excitonic and hole traps on the surface of $CH_3NH_3PbI_3$ thin films[73]. In other studies, the electron trap states, especially at the perovskite/TiO_2 interface, were suggested to cause the inferior performance of perovskite devices without passivation [221]. Since facets with low Miller indices have lower density of dangling bonds[306], it is suggested that the growth of large crystals may decrease the recombination at the surface[73]. Indeed, the trap density estimated for single crystals of $CH_3NH_3PbBr_3$ (10^9 cm^{-3}) and $CH_3NH_3PbI_3$ (10^{10} cm^{-3}) is much lower than trap densities in perovskite thin films (10^{16} cm^{-3}) [76, 303]. The surface-sensitive Kelvin probe (KP) techniques were used widely in the literature to study the effect of trap states on the electronic structure of the surface[75, 307]. Adinolfi et al [75] showed that the Fermi level shifts to 0.12 eV from the conduction band at the surface of $CH_3NH_3PbI_3$ in comparison to the intrinsic bulk. Although the strong recombination of excess charges at the surface is commonly considered detrimental, this effect has been used advantageously to

make devices for narrow-band light and environmental gas detection [132, 308] with single crystal perovskites.
It is common to passivate the surface of inorganic semiconductors through saturating chemical bonds (chemical passivation) to reduce the density of traps or formation of internal electric field below the surface [309] to reduce the concentration of charge carriers or a combination of both [310]. The chemical passivation is usually done by growing an appropriate thin film such as SiN on the surface of c-Si [311, 312].The field-effect passivation is also conducted by either doping the surface or growing an insulator layer such as Al_2O_3 on Si [313] or III-IV semiconductors[314]. Growing thermal SiO_2 film on Si is an example of a passivation method which functions by both reduction of surface traps and providing a built-in field near the surface[310].
In halide perovskites similar passivation methods have been investigated by incorporation of external materials as well as new approaches according to their special chemical structure. Chemical treatments have been used to passivate surface, interface or grain boundaries of halide perovskites via halogenated organic compounds [305], lewis bases [304], fullerene [221, 315–317] and graphene [318]. DFT calculations and experimental observations explained the mechanism of the chemical passivation through binding of the introduced chemicals to certain defects. For example, fullerene suppresses the surface defects through interaction with iodide-rich trap sites at the grain boundaries[221]. Halogenated compounds behave similarly by forming halogen bonds with the excess halides [305]. On the other hand, the lewis bases and graphene interact with undercoordinated Pb ions and neutralize the excess charge caused by halide ions vacancies presented at the surface [304, 318]. The unique chemical structure of perovskites enables specific surface treatment strategies such as self-formation of chemical compounds through ambient exposure. In several studies it has been reported that the formation of PbI_2 during thermal annealing of $CH_3NH_3PbI_3$ films self-passivates the surface and grain boundaries and subsequently improves efficiency of devices [257, 304, 319–322]. In other studies [307, 323] thermal annealing was found beneficial to reduce the traps at the surface, although existence of PbI_2 at the grain boundaries was not speculated. In contrast, Wei et al [324] found formation of $PbBr_2$ at the surface of $CH_3NH_3PbBr_3$ single crystal due to the stoichiometric precursor ratio harmful for the emission properties. They further decreased the surface trap states by a UV-O_3 treatment. Brenes et al [325] performed a combination of light and atmospheric treatment to remove the shallow surface trap states of the $CH_3NH_3PbI_3$ thin films. This unique passivation method resulted in an extremely low surface recombination rate (SRV) of 0.4 $cm.s^{-1}$. Fang et al [308, 323] also employed an air treatment approach which led to the physisorption of water and oxygen on the surface of $CH_3NH_3PbBr_3$ single crystal and reduction of surface trap densities.

Many research groups investigated the application of ultra-thin metal oxide films, such as ZnO [326–329], SnO_x [328] and Al_2O_3[327, 329–334] by atomic layer deposition (ALD) on the halide perovskites as passivation layer in solar cells. More than passivating role, these films behave as promising encapsulation layers to overcome longterm stability issues of the devices at the ambient condition. Note that this is considered different than the common use of ALD metal oxides as the ETL or HTL in planar perovskite solar cells [335]. In most of these studies, comparing the photovoltaic parameters with and without oxide layer showed the improvements of device performance and stability. However, little details about the physical mechanism behind the passivation and its effect on recombination dynamics is known. For example, in a study by Adhyaksa et al[333], the recombination reduction is linked to the nearly threefold increase of diffusion length after ALD of Al_2O_3 on $CH_3NH_3PbBr_3$ thin films. In general very little is known about the exact role of metal oxide passivation and properties of passivated perovskite. Particularly, the recombination rates at the perovskite/metal oxide interface (SRV) have not been quantified previously.

Previously, semiconductor nanowires such as Ge [336], Si [337, 338] and InP [339] were studied to quantify the dynamics of charge carriers and/or investigate the effects of surface passivation. Mainly nanowires are interesting geometries for applications in electronic and optoelectronic devices [293, 340, 341] and also for case studies of dimension-dependent properties. They provide a well-controlled platform to manage and quantify the contribution of surface and bulk precisely by controlling their surface to volume ratio.

Here we employ a similar approach to study the recombination dynamics at the perovskite/alumina interface using perovskite nanowires embedded in anodized aluminum oxide (AAO) templates. The nanowires were fabricated via extrusion as introduced in Chapter 4, but the wires were kept within the template and were not extruded out (Figure 5.1a). Fabrication from perovskite solution directly into the pores of AAO template, without deposition of an extra ALD passivation, avoids high instrumental costs, slow deposition time, variations of film quality due to precursors' purity, and the possible degradation of perovskite film [333] in the ALD technique. We find that the surface of perovskite nanowires is well-passivated by alumina according to the low calculated surface recombination velocity (SRV) at perovskite/alumina interface. By using templates with various pore sizes from ~150 to ~ 350 nm, we systematically changed the surface to volume ratio of the final $CH_3NH_3PbBr_3$ perovskite nanowires. Assuming the bulk quality and radiative rates stay constant, the changes in total recombination rates should be directly connected to the recombination at the perovskite nanowire surfaces. We used time-resolved PL (TRPL) spectroscopy to obtain the dynamics of photoexcited carriers in the perovskite nanowire arrays. This technique is a suitable contactless method

to probe excited states' dynamics at room temperature with picosecond resolution and has been used in the literature widely to study the charge carrier lifetime in perovskites [342, 343]. The recombination rates were extracted from fitting of the PL intensity decay to a rate equation that includes radiative and non-radiative recombination. The obtained lifetime increases slightly from 24.3±2.3 ns to 28.3±1.5 ns when increasing the diameter by more than a factor of two. This shows the weak dependence of PL lifetime on nanowire surface to volume ratio. By fitting these TRPL results to a simple recombination model, we extract a low surface recombination velocity of 37.2±20 cm.s^{-1}. This SRV is very low compared to the value measured for unpassivated surfaces of single crystal $CH_3NH_3PbBr_3$ perovskites (~10^3 cm.s^{-1}) [132, 344, 345], indicating alumina provides excellent passivation for $CH_3NH_3PbBr_3$ perovskite nanowires. This structure can be extended to incorporation into the future device structures.

5.2 Fabrication of Perovskite/Alumina nanowires

In this study we used a suction process similar to the extrusion method explained in Section 4.2 to prepare $CH_3NH_3PbBr_3$ nanowires embedded in an AAO template (perovskite/alumina nanowires). We dropcast the $CH_3NH_3PbBr_3$ solution (3M in dimethyl sulfoxide, DMSO) onto an AAO template (50 μm thick) with pores open on both sides. The template is placed on an O-ring on top of a PDMS block with a hole connected to a low-pressure line. The low pressure in the sealed air compartment between the AAO and the PDMS is created by a simple syringe connected via a plastic tube to the hole. When pulling the piston of the syringe, 50-100 mbar versus atm pressure difference is formed which sucks the perovskite solution through AAO pores. By adjusting the time of the applied pressure gradient, the perovskite solution can either form extruded nanowires or (for shorter times) simply fill the template. In the next step, the template is annealed at 120 °C to remove the solvent and form perovskite nanowires embedded in the AAO template (schematic in Figure 5.1a). The SEM images from the bottom surface and the cross section of the filled templates indicate the filling of pores with $CH_3NH_3PbBr_3$ as presented in Section 5.7. The apparent breaks in the cross-section image can be explained by a cleavage plane that is not perfectly aligned with the pores. This can be seen from periodic breaks as expected from a tilted cleave with continuous nanowires.
Further evidence of pore filling comes from the conductivity and photoconductivity of the perovskite/AAO samples measured through the template thickness. In principle, if the nanowires are continuously expanded from top to the bottom of the AAO templates, the vertical conductivity of the templates should increase dramatically. To check the top-to-bottom conductivity of the templates, we coated thin films of Ti on the both sides of an empty and a perovskite-filled template.

The edges were masked during the coating to make sure that the only electrical pathways between the two bottom and top surfaces is the bulk template in between the Ti electrodes. Current-voltage (I-V) measurements revealed that the empty AAO is insulating as expected (the small current comes from capacitive charging) and the conductivity of the filled template is a thousand times more than the empty one. Moreover, the filled template generated photocurrent under 1 sun AM1.5 illumination as an indication of photocunductivity of perovskite nanowires (figure Figure 5.1b and c).
This simple method provides highly ordered arrays of long perovskite nanowires embedded in a transparent medium with surface passivation potential. The optical properties of perovskite/alumina nanowires were characterized with steady-state PL (405 nm excitation) and absorption measurement (Figure 5.2a). The emission peak at 540 nm (2.29 eV) matches the band gap of $CH_3NH_3PbBr_3$. The nanowire arrays with different diameters, but same sample thickness (50 μm), had similar PL and absorption spectra. The finite-difference time-domain (FDTD) simulation was performed to study the light intensity distribution and absorption in perovskite/alumina nanowire arrays with various diameter, as presented in Section 5.7.5. The electric-field intensity ($|E|^2$) upon the excitation with short-wavelength light (485 nm) decays quickly within the first 5 nanometers away from the surface for all the nanowire arrays with different diameters. The simulated absorption spectrum is in agreement with the experimental data.

5.3 Charge-carrier recombination dynamics at the perovskite/alumina nanowires

We used three templates with average pore diameters of 150.4±35.7, 208.2±34.8 and 361.7±20.4 nm and filled them with $CH_3NH_3PbBr_3$ nanowires to study the charge carrier dynamics and the contribution of the perovskite/alumina interface in the recombination mechanism. By increasing the aspect ratio of the nanowires (l/d) we expect to observe more contribution of the surface to overall recombination process, if bulk recombination stays constant. Since all the samples were prepared from the same solution batch at the same time, and also measured at the same time, we expect the bulk quality and defect densities to be comparable for all of them. Therefore changing nanowire diameters would affect the non-radiative recombination because of the higher density of trap states on the surface. Here we assume that there is no radiative channel in trap-assisted recombination and the only radiative process leading to emission is bimolecular recombination of two charge carriers[67]. Therefore the decay of PL as a function of time can be written

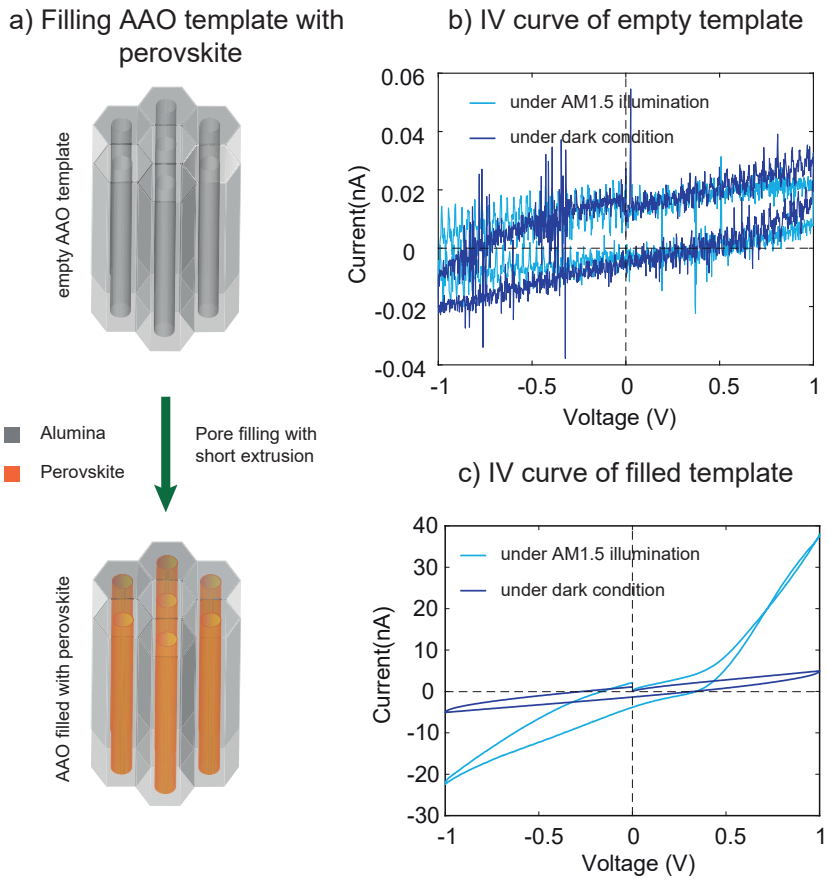

Figure 5.1: $CH_3NH_3PbBr_3$ nanowires embedded in AAO template. **a)** Schematic of AAO template before and after filling with perovskite. **b)** The IV test of a filled template with thin electrodes coated on the top and bottom of it. **c)** The IV curves of an empty AAO template with electrodes on the bottom and top. dark and light blue lines represent the IV curves with and without illumination respectively. The similar curves under both conditions in panel c indicate the insulating and non-photoconductivity nature of the empty AAO template.

as:

$$PL(t) = Ak_2 n(t)^2 + bcg \tag{5.1}$$

Where A is the collection efficiency, k_2 is the bimolecular recombination coefficient, n(t) is the charge carrier densities as a function of time and bcg is the background.

We measured PL(t) of nanowire arrays with time-correlated single photon counting (TCSPC) over more than 8 different spot on each sample (details in Section 5.7.2). A blue laser (485 nm) with fluence of 8.3 μJ.cm^{-2} excited the samples and generated initial carrier density of 3.2×10^{17}. The calculation of carrier density is explained in detail in Supplementary Information (Section 5.7). At this carrier density, the role of Auger recombination is considered negligible ([67, 71, 346]). The representative PL decay curves of each sample are shown in Figure 5.2b.

We solved the differential equation in Equation (1.3) , disregarding the Auger term, to achieve n(t) and replaced the solution in Equation (5.1) as shown below:

$$PL(t) = Ak_2\left(\frac{k_1 n_0}{(k_1 + k_2 n_0)exp(k_1 t) - k_2 n_0}\right)^2 + bcg \tag{5.2}$$

Where n_0 is the initial carrier density at t=0 and k_1 is the trap-assisted recombination coefficient.

By global fitting of Equation (5.2) to the experimental data from TRPL, we extracted the trap-assisted and radiative recombination coefficients k_1 and k_2 and the aver-

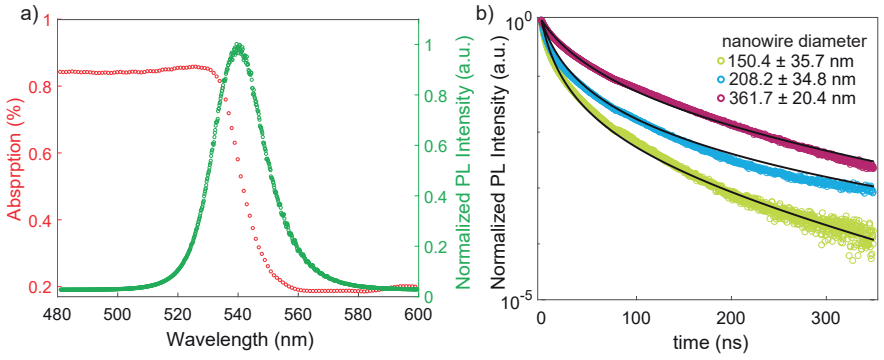

Figure 5.2: Steady-state PL, absorption and transient PL of perovskite/alumina nanowire arrays a) PL (405 nm excitation) and absorption spectra (measured with integrating sphere setup) of the nanowire arrays with average diameter 361.7 nm. The samples with smaller diameter had similar absorption and PL spectra. The absorption spectra of other samples is presented in Figure 5.8. **b)** PL intensity decay of nanowire arrays with various diameter. The black line is the fit to the data according to the model in Equation (5.2)

age values are shown in Table 5.1. For the fitting, we normalized the initial PL (at t=0) and carrier density (n_0) to 1, and removed the background by subtracting the average of data points before excitation from the PL decay data. More details of the fitting procedure are presented in Supplementary Information (Section 5.7).

d (nm)	k_1 ($\times 10^6$ s^{-1})	k_2 ($\times 10^{-10}$ cm^3.s^{-1})	τ (ns)
150.4 ± 35.7	3.71 ± 0.58	1.32 ± 0.24	24.3 ± 2.3
208.2 ± 34.8	3.99 ± 0.92	1.31 ± 0.19	26.9 ± 3.5
362.7 ± 20.4	2.10 ± 0.29	1.06 ± 0.06	28.3 ± 1.5

Table 5.1: Recombination coefficients of $CH_3NH_3PbBr_3$/AAO nanowires with different pore size extracted from global fitting of Equation (5.2) to measured PL decay, as shown in Figure 5.2. d is average diameter of nanowires measured with SEM over ~40 nanowires for each sample and errors are standard deviations. k_1 is trap-assisted recombination coefficient and k_2 is radiative recombination coefficient. The errors are standard errors of the mean of the extracted coefficients measured over more than 8 different spot for each sample. τ is the charge carrier lifetime calculated from Equation (1.5) and the errors are standard error of the means.

As seen in Table 5.1, increasing the nanowire diameter enhances the lifetime of charge carriers. The changes in k_1 can be attributed to the changes of surface defect density due to different surface contribution of each nanowire array, as well as sample-to-sample bulk defect density variations. The small deviation of the k_1 of the sample with 208.2 average diameter from the trend of decrease in non-radiative rate could be due to the later, although we expect such variations in bulk purity to be small because the samples were prepared from the same solution batch. Nevertheless, the decrease in k_1 follows a trend with increasing nanowires diameter considering the error bars of the experiment. The variation of k_2 from sample to sample is small, confirming the radiative processes comes from the band-to-band recombination and therefore depends on the materials' band structure and local density of states. The k_1 values are in the same range as measured by Richter et al [65] with Transient Absorption (TA) for $CH_3NH_3PbBr_3$ thin films ($2.5 \times 10^6 s^{-1}$) and by Wu et al [345] for $CH_3NH_3PbBr_3$ single crystals with TRPL (($2.9 \times 10^6 s^{-1}$), but one order of magnitude lower than values reported by Yang et al [346] from TA measurement ($2.7 \times 10^7 s^{-1}$) of $CH_3NH_3PbBr_3$ thin films. Radiative recombination coefficient is also comparable to references [345, 346], but 10 times lower than reference [65]. Using the recombination coefficients, we calculated the charge carrier lifetime from Equation (5.6) as presented in the last column of Table 5.1. The lifetime is relatively stable, increasing only slightly with diameter. Thus the surface contribution in charge carrier recombination can be considered as a small perturbation. In the next section we developed a model to quantify the surface recombination velocity.

5.4 Surface recombination velocity at the perovskite/alumina interface

In long nanowires studied here, the diameter is essentially the identifier of surface area to bulk volume. In order to discover the dependence of the recombination to the surface, we developed a model to relate the rates (or lifetime) to the nanowire diameter. Assuming the diffusion length of charge carriers in $CH_3NH_3PbBr_3$ is larger than the radius of the nanowires [333], we consider the surface plays a role in the recombination process of charge carriers. For a certain geometry, the total recombination is composed of two terms − bulk and surface − as shown below:

$$R_T = V.R_b + A.R_s \tag{5.3}$$

Where R_T is the total recombination rate , V is the volume, A is the surface area, and R_b and R_s are the total recombination rates at the bulk per volume and at the surface per area. Considering the geometry of the nanowire as a cylinder with radius r and length l Equation (5.3) can be written as:

$$R_T = \pi r^2 l.B + 2\pi r l.S_{alumina} + \pi r^2.S_{air} \tag{5.4}$$

Where B is the bulk recombination velocity and $S_{alumina}$ and S_{air} are the rate at which the charge carrier move towards the nanowire interfaces (SRV) with alumina and air respectively. Since the contribution of the top surface (πr^2) in comparison to the wall surface of the nanowires ($2\pi r l$) is insignificant (from 0.18% to 0.075% for this diameter range) we can neglect the term S_{air} and claim that mostly the perovskite/alumina interface plays a considerable role in surface recombination process. For simplicity, we call $S_{alumina}$ as S, and rewrite Equation (5.4) as:

$$R = R_v + \frac{2S}{r} \tag{5.5}$$

where R is the total recombination rate given by $R(n,t) = k_3 n^2 + k_2 n + k_1$ (Equation (1.4)) and by definition is the inverse of charge carrier lifetime (τ). Neglecting Auger recombination at low carrier densities (<$10^{18} cm^{-3}$), lifetime (τ) is:

$$\tau = \frac{1}{k_1 + k_2 n} \tag{5.6}$$

Therefore, Equation (5.5) is rearranged in the final form as below:

$$1/\tau = 1/\tau_b + \frac{2S}{r} \tag{5.7}$$

This equation shows the linear relationship of inverse of carrier lifetime with the inverse of nanowire radii, where the slope of the line is 2S, and y-intercept is the bulk recombination rate ($1/\tau_b$ =B). This model tells that the lower the slope is, the less the surface contributes to the recombination rates. Therefore if a perfect passivation of the surface is provided, the line would be horizontal with slope zero, and recombination coming only from the bulk. A similar approach using the continuity equation was implemented before by Leonard et al[336] and Dan et al[338] and the same linear relation of the recombination rate and nanowire diameter was derived as also explained in Supplementary Information (Section 5.7).

Fitting Equation (5.7) to the inverse of average lifetime (calculated from Equation (5.6) for more than 8 experiments for each sample) versus inverse of nanowire radii gives SRV of 37.2±20 $cm.s^{-1}$ and bulk recombination rate of 3 $\times 10^7 s^{-1}$ at the initial carrier density of 3.2 $\times 10^{17} cm^{-3}$. The error is the standard deviation of SRV extracted from 10^6 linear fits of the averages of 5 randomly selected data points at each nanowire radius. This result shows that at this carrier density, the recombination is dominated by bulk, and the surface is well passivated. This value is considerably lower than SRVs reported in the various studies for the unpassivated $CH_3NH_3PbBr_3$ single crystals [132, 324, 344, 345] (1.6-6.7$\times 10^3 cm.s^{-1}$) and lower but in the same range as reported for the passivated surface of $CH_3NH_3PbBr_3$ single crystals with UV-O_3 treatment (64 $cm.s^{-1}$) [324]. Fang et al. reported an unusually low SRV of 4 $cm.s^{-1}$ for the $CH_3NH_3PbBr_3$ single crystals by controlling the physisorption of oxygen and water molecules in their surface. We should note that SRV is a facet dependent parameter. While single crystals of $CH_3NH_3PbBr_3$ have (100) facets because of its cubic structure, the nanowire's walls have higher index facets. Most semiconductor nanowires, such as Si and Ge [336, 338], have SRVs 2-3 orders of magnitude higher than what is reported in this study. Obtaining the incredibly small SRV values of 37.2±20 $cm.s^{-1}$ for high index facets of perovskite nanowires confirms the good passivation that alumina provides.

SRV depends not only on the surface trap states (their type and density), but also on the charge carrier density [310]. Therefore we expect increasing the carrier density increases the SRV. We used the same recombination coefficients in Table 5.1, and plot various total recombination lifetimes versus the nanowire radii in Figure 5.3b for charge carrier densities from 10^{15} to $10^{18} cm^{-3}$. A higher carrier concentration is not selected because in the higher excitation regimes Auger recombination is playing a role [71], while it is not considered in our models. Fitting Equation (5.7) to the lines of different carrier density gives us the SRV and bulk recombination, as indicated on each line in Figure 5.3b and is summarized in Table 5.2. Considering the total recombination rate as $S/d + B$, by increasing the carrier density although both S and B increase relatively, the surface recombination plays even a more negligible role compared to the bulk.

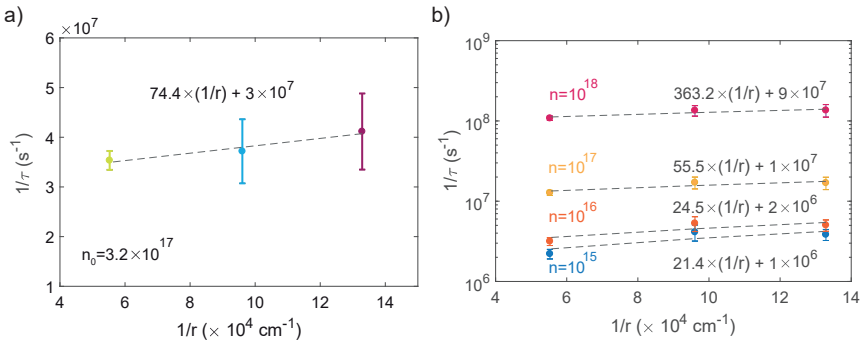

Figure 5.3: Modeling the surface recombination velocity (SRV) of perovskite/alumina using nanowires with various diameters a) Recombination rate ($1tau$) versus inverse of nanowire radii. the lifetime is calculated from Equation (1.5) for the initial carrier density as performed in the TRPL experiment. The dashed line shows the linear fit of Equation (5.5) to the experimental data. The equation achieved from the fit is written above the line. The slope is equal to 2*SRV and the y-intercept is total bulk recombination. **b)** The estimation of SRV and total bulk recombination for various carrier density from 10^{15} to 10^{18} cm^{-3}. With increasing the carrier density SRV increases, but bulk recombination stays dominant.

n (cm^{-3})	S (cm.s^{-1})	B (s^{-1})	S/(B.d_{av} + S)(%)
10^{15}	10.7	10^6	34.8
10^{16}	12.3	2 ×10^6	23.5
10^{17}	27.7	10^7	12.2
10^{18}	182.2	9 ×10^7	9.2

Table 5.2: Surface (S) and bulk (B) recombination velocities for $CH_3NH_3PbBr_3$/AAO nanowires at different carrier densities. S and B are fit parameters as shown in Figure 5.2b. $S/(B.d_{av} + S)$ is the contribution of surface recombination to the total recombination for a representative nanowire with average diameter of $d_{av} = 200nm$

5.5 Radiative efficiency of Perovskite/Alumina nanowires

An important parameter defining the optical quality of a light-absorbing structure is the radiative efficiency or as explained in Section 4.4 the photoluminescence quantum yield (PLQY). PLQY is described as the ratio of radiated photons out of the absorber to the total absorbed photons. Presumably the emitted photons are coming from band-to-band recombination of charge carriers and the absorbed photons

create total charge carriers which decay through one of the recombination channels. Hence, the total recombination rate represents to the total absorption. We can rewrite the PLQY based on the recombination mechanisms as:

$$PLQY = \frac{k_2 n^2}{k_1 n + k_2 n^2} \tag{5.8}$$

Therefore, defining the rate coefficients reveals the PLQYs for $CH_3NH_3PbBr_3$/alumina nanowires. Based on the recombination rates listed in Table 5.1, we calculated the PLQY of the nanowire arrays at various relevant charge carrier densities as listed in the table below:

$n(cm^{-3})$	$d_{av}(nm)$	$PLQY_{TRPL}(\%)$	$PLQY_{IS}(\%)$
1×10^{15}	150.4	3.44	-
	208.2	3.18	-
	361.7	4.80	-
3.2×10^{17}	150.4	91.94	-
	208.2	91.32	-
	361.7	94.16	-
1.5×10^{18}	150.4	-	1.18 ± 0.46
	208.2	-	4.29 ± 2.67
	361.7	-	4.49 ± 0.98

Table 5.3: PLQYs of $CH_3NH_3PbBr_3$/AAO nanowires nanowires at different carrier densities and various average diameters (d_{av}). $PLQY_{TRPL}$ are calculated from Equation (5.8) and recombination coefficients from Table 5.1. $PLQY_{IS}$ is directly measured with integrating sphere setup with the initial carrier density of $1.5 \times 10^{18} cm^{-3}$.

The last column in Table 5.3 presents the PLQY directly measured with the integrating sphere (IS) microscopy setup as presented in Figure 4.12 (excitation with pulsed (repetition rate 40 MHz) 480 laser and 37.4 $\mu J.cm^{-2}$ fluence). The box plot in Figure 5.4 shows the measured PLQY values over more than 2500 points for each perovskite/alumina nanowire array sample with $\approx 500 \times 500 \mu m$ size (details in Section 5.7.4).

We observe a high mismatch between the experimentally measured PLQYs and the ones calculated from Equation (5.8). This discrepancy have several contributing factors: (i) The PLQY and TRPL are performed at different carrier densities. The PLQY at higher carrier density ($1.5 \times 10^{18} cm^{-3}$) may suffer from Auger recombination, which is considered negligible at lower initial carrier density of TRPL ($3.2 \times 10^{17} cm^{-3}$). Taking Auger recombination into account will decrease the PLQYs calculated from the rate coefficients at high carrier density; a reduction by nearly a factor of 10 was seen in a previous study at these carrier density values [65]

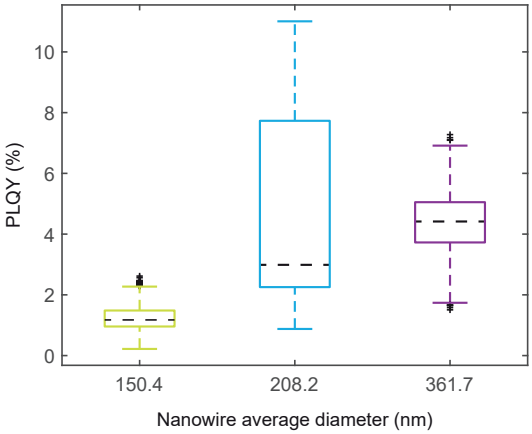

Figure 5.4: Statistics of PLQY values experimentally measured for perovskite nanowire arrays with pore dimension 150.4, 208.2 and 361.7 nm. The dashed line in each box is the median. The up and bottom edges of the boxes are 75% and 25% percentiles respectively. The horizontal lines on top and bottom, out of the of the boxes, show the upper and lower adjacent, and the black crosses are the outliers.

(ii) A second reason for the high mismatch between the experimental and calculated PLQY is that photon re-absorption plays a considerable role in the experimental PLQY measurement. Perovskite materials exhibit high photon re-absorption because of the the overlap of the absorption and emission spectra (see Figure 5.2a). When the absorber medium has high refractive index, the emitted photons from radiative recombination reflect back from the surface due to the total internal reflection and get re-absorbed inside the material. The narrow cone for the emitted light to escape the semiconductor (known as escape probability,p_{esc}) causes a significant deviation of externally measured quantum yield (PLQY) from the internal one (η_{in}) according to:

$$PLQY = \frac{\eta_{in}.p_{esc}}{1-\eta_{in}.(1-p_{esc})} \tag{5.9}$$

η_{in} is a material specific property, which is defined as the fraction of radiative events to the total recombination. In planar semiconductors with high refractive indices, the p_{esc} becomes very small, given by $1/2n^2$ where n is the refractive index. Our sample essentially consists of a photonic crystal, which may further reduce escape probability by altering in-plane and out-of-plane emission probabilities. Further work is needed to determine the effect of such photonic crystal effects.
We have evidence suggesting that photon re-absorption via in-plane emission and waveguiding plays a major role in reducing the PLQY measured in our integrating

sphere, namely that the PLQY is strongly dependent on sample size. Decreasing sample size reduces the distance that radiated photons have to travel to escape out. Therefore it is expected that samples with larger size have lower PLQY. Indeed, perovskite/alumina nanowire arrays with average diameter of 208 nm and larger sample size of ≈ 5×5 mm have experimental PLQY of 1.44 ± 0.36%, ~ 3 times lower than smaller samples (~ $500\times500\mu m$) with PLQY of 4.29 ± 2.67% (See Figure 5.6 and Figure 5.7). Further work must be done to understand the remaining contributions of waveguiding and re-absorption to PLQY in the smaller samples.
This discrepancy between the experimentally measured PLQYs and calculated PLQYs from recombination coefficients in halide perovskite thin films has been reported previously by Richter et al [65] and is attributed to the existence of non-radiative bimolecular recombination channel. The nature of this pathway is not known. On the other hand, the integrating sphere method is initially developed for measurement of small structures [347–349] and large area samples should be measured with caution due to photon re-absorption effect. It is necessary to repeat the TRPL and direct PLQY measurements at the same initial carrier intensity, as well as further intensity-dependent study of PLQY, to achieve a comprehensive picture of photon recycling effect and exact internal and external quantum yields.

5.6 Conclusion and Outlook

In this study we fabricated long $CH_3NH_3PbBr_3$ nanowire arrays embedded in AAO template (perovskite/alumina nanowires) using a simple solution technique by suction of the perovskite solution through the AAO pores. The charge carrier recombination mechanism of the perovskite/alumina nanowire arrays was studied with time-resolved PL spectroscopy. Fitting of the PL intensity decay to a rate equation that includes radiative (bimolecular) and non-radiative (monomolecular) recombination was used to obtain the recombination rate coefficients. We estimated a charge carrier lifetime of more than 20 ns at the initial carrier density of $3.2\times10^{17} cm^{-3}$ for nanowires with various diameters. The inverses of lifetimes increase linearly with decreasing the nanowire diameters. This data was fitted to a model to extract very low SRV of 37.2±20 $cm.s^{-1}$ at the $CH_3NH_3PbBr_3/Al_2O_3$ interface. The low SRV of passivated nanowires in comparison to unpassivated $CH_3NH_3PbBr_3$ single crystals (~ 10^3 $cm.s^{-1}$) [141, 345, 350], ensures that despite the large surface of perovskite nanowires, their surface was not dominant in recombination processes. The presented results here confirm the passivation effect alumina provides for hybrid halide perovskites and quantifies the surface recombination velocity at the perovskite/alumina interface for the first time. This study presents a simple method for the passivation of perovskite surface, without the need for ALD deposition of Al_2O_3. Further studies to compare the perovskite

nanowires passivated with ALD and the ones embedded in AAO template will provide a comprehensive picture of the similarities and differences of these two methods.
Here we measured the PLQYs using IS microscopy technique which showed significantly lower values than what is expected from the calculated PLQYs using recombination coefficients. The photon re-absorption effect, and involvement of Auger process in the recombination at the high excitation density of the experiment may be the reasons for this discrepancy. Future studies of the effect of photon recycling by measuring the PLQYs at the lower excitation regime are required to estimate the radiative efficiency of perovskite/alumina nanowire arrays more accurately. Perovskite nanowire arrays in AAO templates have high potential for integration in highly efficient optoelectronic devices as shown before for image sensors [182], photodetectors [277] and semi-transparent solar cells [351]. The simple solution fabrication and high quality photophysical properties presented here highlight perovskite/alumina nanowires as promising candidates for future applications.

5.7 Supplementary Information

The perovskite precursor, solution and template preparations are the same as explained in Section 4.6. The filling of AAO nanopores with perovskite solution were done in a similar condition as explained in extrusion of nanowires in Chapter 4, only the pressure gradient was applied for a shorter time in comparison, to keep the nanowires inside the template.

5.7.1 Scanning electron microscopy

SEM images were taken by a FEI Verios 460 at 5 kV accelerating voltage, with through the lens detector (TLD) for the top view image (Figure 5.5a) and the mirror high energy detector (MD) for the side view image (Figure 5.5b). The MD detector highlights the compositional and topographical contrasts. The brighter lines are attributed to the perovskite containing heavy Pb elements. Although these bright lines may not seem continuous, the non-uniformity of perovskite nanowires within the template's pores could be due to the fracture of nanowires when breaking the sample.

5.7.2 Time-correlated single photon counting

The time-resolved PL (TRPL) of nanowire arrays was measured with the time-correlated single photon counting (TCSPC) technique. In this method, a pulsed laser at 485 nm (PicoQuant PDL 828) is used to excite the samples and the

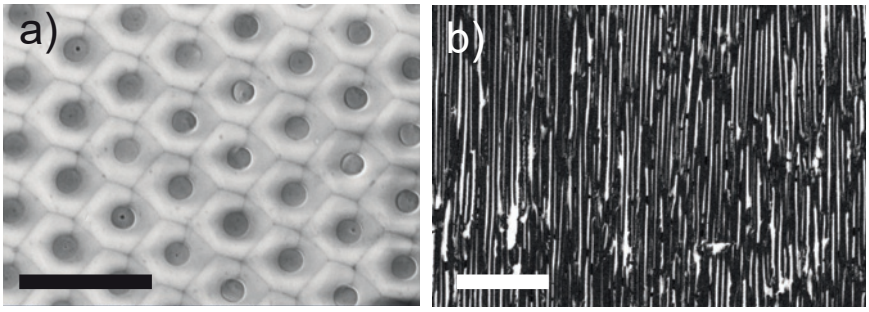

Figure 5.5: SEM images showing the morphology of perovskite nanowires inside AAO template poresa) Top-view image of the bottom side of the template after the pores were filled with perovskite. The scale bar 2 μm. **b)** The cross section view of the filled template taken with the MD detector of SEM. The bright lines show perovskites. The scale bar is 5 μm.

luminescence of the sample is collected over multiple cycles of excitation and emission using a single photon counting detector (MicroPhoton Devices, MPD-5CTD) and a picosecond time analyzer (PicoQuant HydraHarp 400). The repetition rate of the laser can be tuned from 0.5 to 40 MHz using a PicoQuant LDH-D-C-485. We chose the repetition rate of 1 MHz for this experiment. The excitation density was controlled with adjusting the power of the laser and using a series of neutral density filters. The power which the experiment was run at was 0.06 μW. A long pass filter (ET500LP, Chroma Tech) blocked the laser and let the emission of the samples to pass through to reach the detectors. The measurements were all done at the ambient condition.

In each sample more than 8 different 20×20 μm^2 regions were scanned over 256×256 pixel, where in each pixel the PL intensity decay was collected. The PL decay curve was integrated over the whole scanned area and fitted with the model presented in Equation (5.2) to extract the recombination coefficients for each region. The recombination coefficients presented in Table 5.1 are averages over all the measured regions for each sample, and the error bars are standard error of the mean.

Calculation of initial charge carrier density

We calculated the initial charge carrier density according to:

$$n_0 = \frac{N_{photons} \times A}{t} \tag{5.10}$$

Where $N_{photons}$ is the number of photons per pulse calculated from repetition rate (1 MHz), laser power density (8 W.cm^{-2}) and energy of photons at 485 nm excitation, t is the effective thickness of the sample and A is absorption at the excitation. A is considered 85% according to the absorption spectra measured for nanowire arrays (Figure 5.2a). Since the sample thickness (AAO thickness 50 μm) is much larger than expected diffusion lentgh of charge carriers, the effective thickness is assumed as the longest distance the charge carriers may travel, i.e. diffusion length. According to the reported charge carrier diffusion length of $CH_3NH_3PbBr_3$ coated with alumina [333] we considered it as 500 nm as well. We assumed the initial charge carrier density is consistent with all samples with different pore size.
The simulation of electric field distribution in perovskite nanowire arrays with different diameter (Section 5.7.5) showed that at the excitation wavelength (485 nm), the light is absorbed within the first 5 nanometer of the sample. However, the concentration of electric field within the nanowires with small diameter may generate a higher initial concentration. We calculated that even if the real initial carrier density was 10 times higher ($10^{18} cm^{-3}$), the SRV is the same as 37.2±20 cm.s^{-1} at the initial carrier density (although k_2 changes with initial carrier density, product of $n_0 k_2$ and k_1 remains the same), which makes it subsequently lower at device relevant carrier densities modeled in Figure 5.2b. We could fit the data with only taking mono- and bimolecular recombination into account, therefore we believe Auger recombination did not play a role in the recombination dynamics, even if we had higher initial carrier densities up to $10^{18} cm^{-3}$.

5.7.3 Calculation of SRV from continuity equation

A diameter-dependent carrier lifetime has been modeled previously for nanowires [336, 338, 339] based on the solution of continuity equation for an infinitely long cylinder with diameter d :

$$\frac{\partial n(r,t)}{\partial t} = D \bigtriangledown^2 n(r,t) - \frac{n(r,t)}{\tau_b} \tag{5.11}$$

Where n(r,t) is the photoexcited excess carrier density, D is the diffusion constant, r is radial coordinate and τ_b is carrier lifetime in the bulk. The boundary condition for this equation is given by:

$$-D(\frac{\partial n(r,t)}{\partial r})_{r=d/2} = S.n(d/2,t) \tag{5.12}$$

Where electron and holes recombine with the velocity S at the surface. Solving Equation (5.12) result in an exponential time decay of the carrier density given by:

$$1/\tau = 1/\tau_b + \lambda \tag{5.13}$$

where λ comes from:

$$D\lambda J_1(\lambda.d/2) = SJ_0(\lambda.d/2) \tag{5.14}$$

J_0 and J_1 are 0^{th} and 1^{st} order Bessel functions. If we assume S$\ll D/d$, it is valid to use the small argument behavior of Bessel function:

$$J_n(a) \approx \frac{1}{2^n n!} a^n \tag{5.15}$$

So $\lambda = 4S/d$. Substituting this into Equation (5.13), we have:

$$1/\tau = 1/\tau_b + \frac{4S}{d} \tag{5.16}$$

Which is the same as Equation (5.7) as presented in Section 5.4.
In order to check the validation of the assumption S$\ll D/d$, we obtained D from $L_{diff} = (D\tau_{eff})^{1/2}$, where L_{diff} is diffusion length and τ_{eff} is carrier effective lifetime. The L_{diff} extracted from reference [333] for $CH_3NH_3PbBr_3$ coated with ALD alumina as 500 nm and the carrier effective lifetime is considered as 20 ns^{-1} based on our TRPL experiment. Thus D=0.125 $cm^2.s^{-1}$. The largest perovskite nanowire has the average diameter of 362 nm. Having S = 37.2±20 $cm.s^{-1}$ and $D/d = (0.125 cm^2.s^{-1})/(362 \times 10^{-7} cm) = 3453$ the assumption S $\ll D/d$ is valid.

5.7.4 PLQY measurement

The PLQY experiment is done using the integrating sphere microscopy as explained in Section 4.6.2. The samples were excited with 480 nm laser with power density of $1.5{\times}10^3 W.cm^{-2}$. This power density generates 1.5 $\times 10^{19} cm^{-3}$ charge carrier density considering 85% absorption(Equation (5.10)). For each sample of perovskite nanowire arrays, the absorption and PL is scanned in at least 4 random area of $12{\times}12$ μm^2 with 0.5 μm scan step. The PLQY maps in each of the samples are shown in Figure 5.6. The Figure 5.4 represent the statistics of the PLQY values for these sample over more than 2500 points.

PLQY of samples with large size

In order to check the photon re-absorption effect in the perovskite/alumina nanowire array samples, we performed the PLQY experiment in the IS microscopy setup with $5{\times}5 mm^2$ large sample with 208 nm average nanowire dimatere in 3 different positions as shown in Figure 5.7. The PLQY average over in total more than 3400 points is 1.44 ±0.36%, ~3 times lower than average PLQY of the small size sample, as presented in Section 5.5.

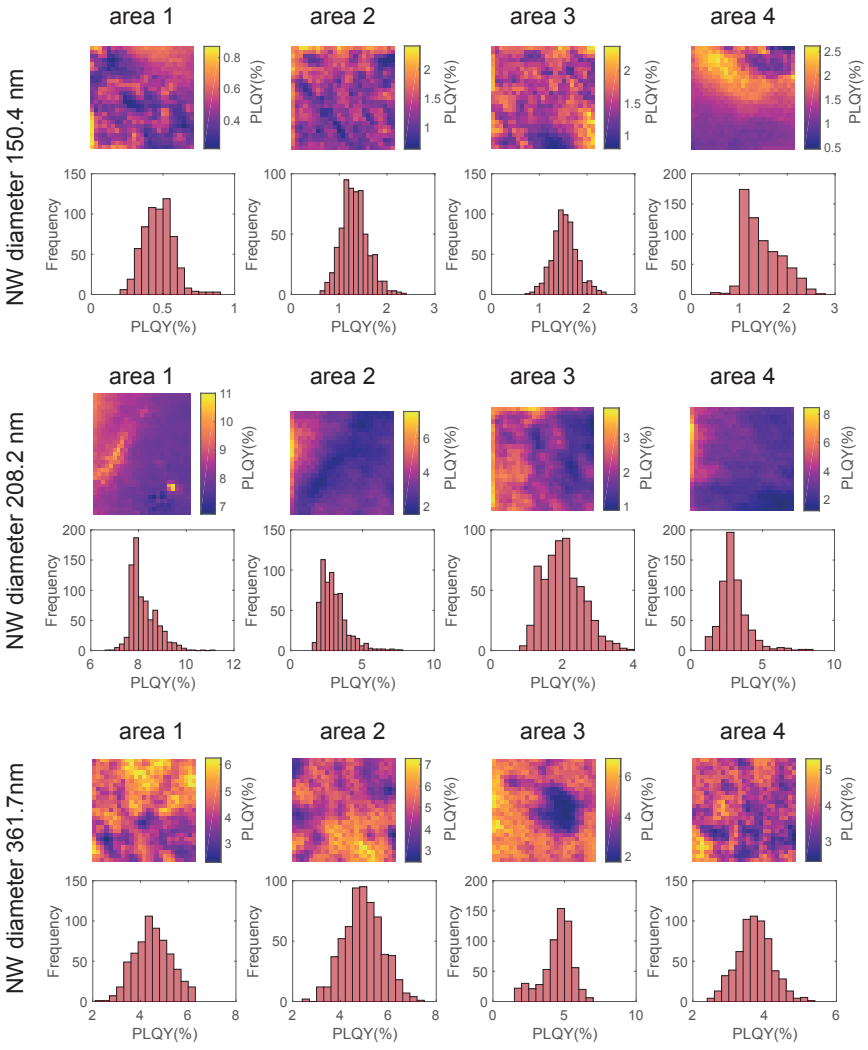

Figure 5.6: The PLQY maps of samples with different nanowire (NW) diameter in 4 different areas. Below each map the histogram of the PLQY values are presented to show the distribution of the data. all areas are $12\times12\ \mu m^2$ with 0.5 μm scan step except the scan of area 1 in the sample with nanowire diameter 208.2 nm, which is $15\times12\ \mu m^2$.

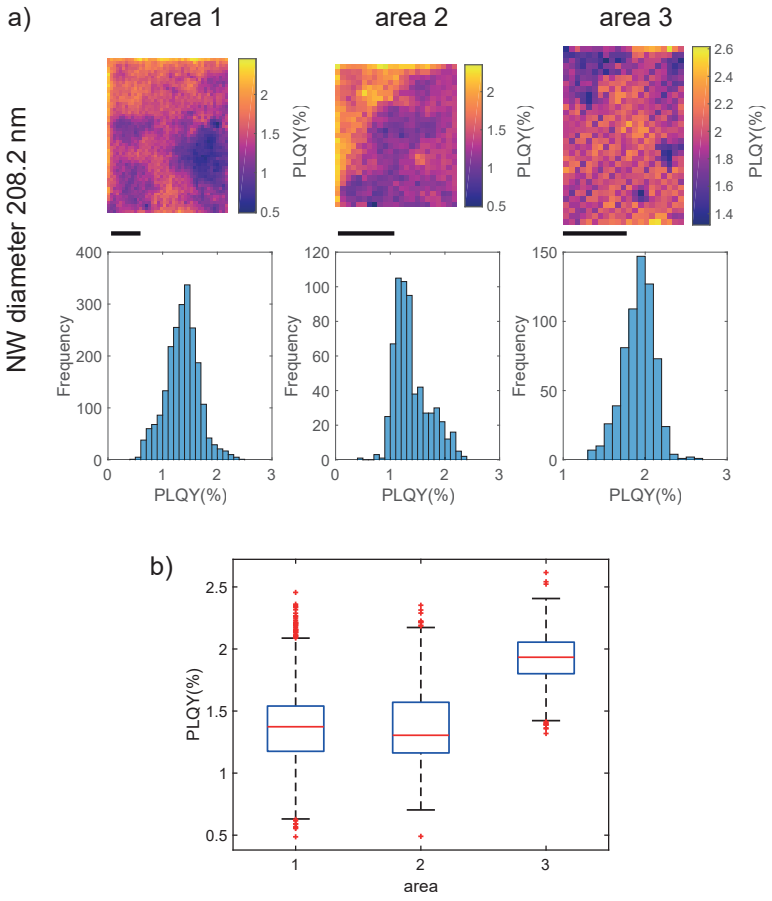

Figure 5.7: The PLQY study of nanowire array sample with large size 5×5mm^2 a) Maps of 5 × 5mm^2 sample with average nanowire (NW) diameter 208 nm in 3 different areas. Below each map the histogram of the PLQY values are presented to show the distribution of the data. The scale bar is 5 μm.**b)** The statics of PLQY distribution in each area.The red line in each box is the median. The up and bottom edges of the boxes are 75% and 25% percentiles respectively. The horizontal lines on top and bottom, out of the of the boxes, show the upper and lower adjacent, and the red crosses are the outliers.

5.7.5 Simulation of absorption and E-field distribution of nanowire array

The optical simulations on perovskite/alumina nanowires were performed using a commercial simulator based on the FDTD method (Lumerical, Inc) for nanowire arrays. The nanowires were considered as $CH_3NH_3PbBr_3$ cylinders with average diameter of 361.7, 208.2 and 150.4 nm and pitch of 977, 771 and 684 nm respectively embedded in alumina. A plane wave light source with wavelength=450-600nm was placed at z=3.8 μm with downward propagation. The nanowire surface was fixed at z=4.8 μm the x and y directions have periodic boundary condition (BC), while perfectly matched layer BC was chosen for the z direction.

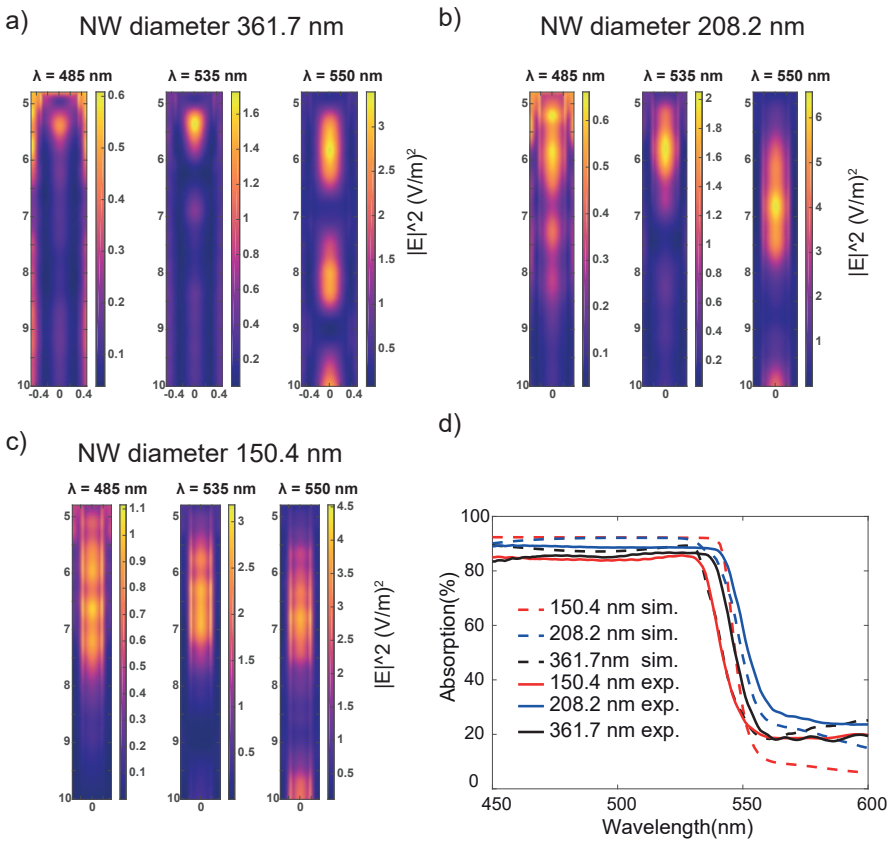

Figure 5.8: The optical simulation of electric field and absorption in perovskite/alumina nanowire arrays with FDTD method a-c) $|E|^2$ distribution at incident light wavelengths of 485, 535 and 550 nm for nanowires (NW) with different diameter. 485 nm is the wavelength of the light excitation at TRPL experiment, 535 is the perovskite bandgap and 550 is an example of below band gap incident light. **d)** Simulated (dashed lines) and experimentally measured (solid lines) absorption spectra for nanowires. The below band gap absorption probably comes from in the experiments from a slight tilt in sample mount during the experiment, and in the simulation from non-zero k optical constant of perovskite.

References

[1] *https://www.mindat.org*.

[2] F. Galasso, *STRUCTURE OF PEROVSKITE-TYPE COMPOUNDS*, in *Structure, Properties and Preparation of Perovskite-Type Compounds*, pages 3–49, Elsevier, 1969.

[3] J. Albero, A. R. Malik, and H. Garcia, *Influence of the Composition of Hybrid Perovskites on their Performance in Solar Cells*, J. Mater. Chem. A (2016).

[4] S. Brittman, G. W. P. Adhyaksa, and E. C. Garnett, *The expanding world of hybrid perovskites: materials properties and emerging applications*, MRS Communications , 1 (2015).

[5] V. M. Goldschmidt, *Die Gesetze der Krystallochemie*, Naturwissenschaften **14**, 477 (1926).

[6] D. M. Giaquinta and H.-C. zur Loye, *Structural Predictions in the ABO3 Phase Diagram*, Chemistry of Materials **6**, 365 (1994).

[7] C. Li, K. C. K. Soh, and P. Wu, *Formability of ABO3 perovskites*, Journal of Alloys and Compounds **372**, 40 (2004).

[8] J. Zhu, H. Li, L. Zhong, P. Xiao, X. Xu, X. Yang, Z. Zhao, and J. Li, *Perovskite oxides: Preparation, characterizations, and applications in heterogeneous catalysis*, ACS Catalysis **4**, 2917 (2014).

[9] H. L. Wells, *Über die Cäsium- und Kalium-Bleihalogenide*, Zeitschrift für anorganische Chemie **3**, 195 (1893).

[10] C. Li, X. Lu, W. Ding, L. Feng, Y. Gao, and Z. Guo, *Formability of ABX 3 (X = F, Cl, Br, I) halide perovskites*, Acta Crystallographica Section B Structural Science **64**, 702 (2008).

[11] D. Weber, *{CH3NH3PbX3}, a Pb(II)-System with Cubic Perovskite Structure*, Zeitschrift für Naturforschung B **33b**, 1443 (1978).

[12] D. Weber, *CH3NH3SnBrxI3-x (x=0-3), a Sn(II)-system with the cubic perovskite structure*, Zeitschrift für Naturforschung **33b**, 862 (1978).

[13] M. a. Green, A. Ho-Baillie, and H. J. Snaith, *The emergence of perovskite solar cells*, Nature Photonics **8**, 506 (2014).

[14] C. C. Stoumpos and M. G. Kanatzidis, *The Renaissance of Halide Perovskites and Their Evolution as Emerging Semiconductors*, Accounts of Chemical Research (2015).

[15] D. B. Mitzi, C. A. Feild, W. T. A. Harrison, and A. M. Guloy, *Conducting Tin Halides with a Layered Organic-based Perovskite Structure*, Nature **369**, 467 (1994).

[16] D. B. Mitzi, C. Feild, Z. Schlesinger, and R. B. Laibowitz, *Transport, Optical, and Magnetic Properties of the Conducting Halide Perovskite CH3NH3SnI3*, Journal of Solid State Chemistry **114**, 159 (1995).

[17] D. B. Mitzi, S. Wang, C. a. Feild, C. a. Chess, and a. M. Guloy, *Conducting Layered Organic-inorganic Halides Containing <110>-Oriented Perovskite Sheets*, Science (New York, N.Y.) **267**, 1473 (1995).

[18] D. B. Mitzi, K. Chondroudis, and C. R. Kagan, *Design, Structure, and Optical Properties of OrganicInorganic Perovskites Containing an Oligothiophene Chromophore*, Inorganic Chemistry **38**, 6246 (1999).

[19] A. Kojima, K. Teshima, Y. Shirai, and T. Miyasaka, *Organometal Halide Perovskites as Visible-light Sensitizers for Photovoltaic Cells*, Journal of the American Chemical Society **131**, 6050 (2009).

[20] *https://www.nrel.gov/pv/assets/images/efficiency-chart.png*.

[21] M. M. Lee, J. Teuscher, T. Miyasaka, T. N. Murakami, and H. J. Snaith, *Efficient Hybrid Solar Cells Based on Meso-superstructured Organometal Halide Perovskites*, Science **338**, 643 (2012).

[22] M. Liu, M. B. Johnston, and H. J. Snaith, *Efficient planar heterojunction perovskite solar cells by vapour deposition*, Nature **501**, 395 (2013).

[23] H. J. Snaith, *Perovskites: The Emergence of a New Era for Low-Cost, High-Efficiency Solar Cells*, The Journal of Physical Chemistry Letters **4**, 3623 (2013).

[24] N. J. Jeon, J. H. Noh, W. S. Yang, Y. C. Kim, S. Ryu, J. Seo, and S. I. Seok, *Compositional engineering of perovskite materials for high-performance solar cells*, Nature **517**, 476 (2015).

[25] W. Nie, H. Tsai, R. Asadpour, J.-C. Blancon, A. J. Neukirch, G. Gupta, J. J. Crochet, M. Chhowalla, S. Tretiak, M. A. Alam, H.-L. Wang, and A. D. Mohite, *High-efficiency solution-processed perovskite solar cells with millimeter-scale grains*, Science **347**, 522 (2015).

[26] P. Docampo and T. Bein, *A Long-Term View on Perovskite Optoelectronics*, Accounts of Chemical Research **49**, 339 (2016).

[27] J. You, L. Meng, Z. Hong, G. Li, and Y. Yang, *Inverted planar structure of perovskite solar cells*, Organic-Inorganic Halide Perovskite Photovoltaics: From Fundamentals to Device Architectures , 307 (2016).

[28] J. M. Frost, K. T. Butler, F. Brivio, C. H. Hendon, M. van Schilfgaarde, and A. Walsh, *Atomistic Origins of High-Performance in Hybrid Halide Perovskite Solar Cells*, Nano Letters **14**, 2584 (2014).

[29] A. Miyata, A. Mitioglu, P. Plochocka, O. Portugall, J. T.-W. Wang, S. D. Stranks, H. J. Snaith, and R. J. Nicholas, *Direct measurement of the exciton binding energy and effective masses for charge carriers in organic–inorganic tri-halide perovskites*, Nature Physics **11**, 582 (2015).

[30] A. R. Srimath Kandada and A. Petrozza, *Photophysics of Hybrid Lead Halide Perovskites: The Role of Microstructure*, Accounts of Chemical Research **49**, 536 (2016).

[31] M. B. Johnston and L. M. Herz, *Hybrid Perovskites for Photovoltaics: Charge-Carrier Recombination, Diffusion, and Radiative Efficiencies*, Accounts of Chemical Research **49**, 146 (2016).

[32] J. M. Frost and A. Walsh, *What Is Moving in Hybrid Halide Perovskite Solar Cells?*, Accounts of chemical research **49**, 528 (2016).

[33] S. S. Zumdahl, *Chemical Principles*, 2005.

[34] A. West, *Solid State Chemistry and its Applications, 2nd Edition, Student Edition*, 2014.

[35] T. Umebayashi, K. Asai, T. Kondo, and A. Nakao, *Electronic structures of lead iodide based low-dimensional crystals*, Physical Review B **67**, 155405 (2003).

[36] Y. H. Chang, C. H. Park, and K. Matsuishi, *First-principles study of the structural*

and the electronic properties of the lead-halide-based inorganic-organic perovskites (CH3NH3)PbX3 and CsPbX3 (X = Cl, Br, I), Journal of the Korean Physical Society **44**, 889 (2004).

[37] E. Mosconi, A. Amat, M. K. Nazeeruddin, M. Grätzel, and F. De Angelis, *First-Principles Modeling of Mixed Halide Organometal Perovskites for Photovoltaic Applications*, The Journal of Physical Chemistry C **117**, 13902 (2013).

[38] T. Baikie, Y. Fang, J. M. Kadro, M. Schreyer, F. Wei, S. G. Mhaisalkar, M. Graetzel, and T. J. White, *Synthesis and crystal chemistry of the hybrid perovskite (CH3NH3)PbI3 for solid-state sensitised solar cell applications*, Journal of Materials Chemistry A **1**, 5628 (2013).

[39] M. R. Filip, G. E. Eperon, H. J. Snaith, and F. Giustino, *Steric engineering of metal-halide perovskites with tunable optical band gaps*, Nature Communications **5**, 5757 (2014).

[40] B. R. Sutherland and E. H. Sargent, *Perovskite photonic sources*, Nature Photonics **10**, 295 (2016).

[41] M. Wei, Y.-H. Chung, Y. Xiao, and Z. Chen, *Color tunable halide perovskite CH3NH3PbBr3xClx emission via annealing*, Organic Electronics **26**, 260 (2015).

[42] Y. Wang, X. Sun, R. Shivanna, Y. Yang, Z. Chen, Y. Guo, G.-C. Wang, E. Wertz, F. Deschler, Z. Cai, H. Zhou, T.-M. Lu, and J. Shi, *Photon Transport in One-Dimensional Incommensurately Epitaxial CsPbX 3 Arrays*, Nano Letters , acs.nanolett.6b04297 (2016).

[43] G. Xing, N. Mathews, S. S. Lim, N. Yantara, X. Liu, D. Sabba, M. Grätzel, S. Mhaisalkar, and T. C. Sum, *Low-temperature solution-processed wavelength-tunable perovskites for lasing*, Nature Materials **13**, 476 (2014).

[44] C. M. Sutter-Fella, Y. Li, M. Amani, J. W. Ager, F. M. Toma, E. Yablonovitch, I. D. Sharp, and A. Javey, *High Photoluminescence Quantum Yield in Band Gap Tunable Bromide Containing Mixed Halide Perovskites*, Nano Letters **16**, 800 (2016).

[45] J. Xing, X. F. Liu, Q. Zhang, S. T. Ha, Y. W. Yuan, C. Shen, T. C. Sum, and Q. Xiong, *Vapor Phase Synthesis of Organometal Halide Perovskite Nanowires for Tunable Room-Temperature Nanolasers*, Nano Letters **15**, 4571 (2015).

[46] F. Zhang, H. Zhong, C. Chen, X.-G. Wu, X. Hu, H. Huang, J. Han, B. Zou, and Y. Dong, *Brightly Luminescent and Color-Tunable Colloidal CH3NH3PbX3 (X = Br, I, Cl) Quantum Dots: Potential Alternatives for Display Technology*, ACS nano (2015).

[47] S. a. Kulkarni, T. Baikie, P. P. Boix, N. Yantara, N. Mathews, and S. Mhaisalkar, *Band-gap tuning of lead halide perovskites using a sequential deposition process*, Journal of Materials Chemistry A **2**, 9221 (2014).

[48] N. K. Kumawat, A. Dey, A. Kumar, S. P. Gopinathan, K. L. Narasimhan, and D. Kabra, *Band Gap Tuning of CH3NH3Pb(Br(1-x)Clx)3 Hybrid Perovskite for Blue Electroluminescence*, ACS Applied Materials and Interfaces **7**, 13119 (2015).

[49] R. J. Sutton, G. E. Eperon, L. Miranda, E. S. Parrott, B. A. Kamino, J. B. Patel, M. T. Hörantner, M. B. Johnston, A. A. Haghighirad, D. T. Moore, and H. J. Snaith, *Bandgap-Tunable Cesium Lead Halide Perovskites with High Thermal Stability for Efficient Solar Cells*, Advanced Energy Materials , n/a (2016).

[50] Y. Tong, E. Bladt, M. F. Aygüler, A. Manzi, K. Z. Milowska, V. A. Hintermayr, P. Docampo, S. Bals, A. S. Urban, L. Polavarapu, and J. Feldmann, *Highly Luminescent Cesium Lead Halide Perovskite Nanocrystals with Tunable Composition and Thickness by Ultrasonication*, Angewandte Chemie International Edition (2016).

[51] Q. A. Akkerman, V. D'Innocenzo, S. Accornero, A. Scarpellini, A. Petrozza, M. Prato, and L. Manna, *Tuning the optical properties of cesium lead halide perovskite nanocrystals*

by anion exchange reactions, Journal of the American Chemical Society **137**, 10276 (2015).

[52] K. Yamada, K. Nakada, Y. Takeuchi, K. Nawa, and Y. Yamane, *Tunable Perovskite Semiconductor CH3NH3SnX3 (X: Cl, Br, or I) Characterized by X-ray and DTA*, Bulletin of the Chemical Society of Japan **84**, 926 (2011).

[53] H.-J. Feng, T. R. Paudel, E. Y. Tsymbal, and X. C. Zeng, *Tunable optical properties and charge separation in CH3NH3SnxPb1-xI3/TiO2 based planar perovskites cells.*, Journal of the American Chemical Society (2015).

[54] G. E. Eperon, S. D. Stranks, C. Menelaou, M. B. Johnston, L. M. Herz, and H. J. Snaith, *Formamidinium lead trihalide: a broadly tunable perovskite for efficient planar heterojunction solar cells*, Energy & Environmental Science **7**, 982 (2014).

[55] F. Hao, C. C. Stoumpos, R. P. H. Chang, and M. G. Kanatzidis, *Anomalous band gap behavior in mixed Sn and Pb perovskites enables broadening of absorption spectrum in solar cells Anomalous band gap behavior in mixed Sn and Pb perovskites enables broadening of absorption spectrum in solar cells*, Journal of the American Chemical Society **136**, 8094 (2014).

[56] L. Lang, J.-H. Yang, H.-R. Liu, H. Xiang, and X. Gong, *First-principles study on the electronic and optical properties of cubic ABX3 halide perovskites*, Physics Letters A **378**, 290 (2014).

[57] A. Amat, E. Mosconi, E. Ronca, C. Quarti, P. Umari, M. K. Nazeeruddin, M. Grätzel, and F. De Angelis, *Cation-induced band-gap tuning in organohalide perovskites: Interplay of spin-orbit coupling and octahedra tilting*, Nano Letters **14**, 3608 (2014).

[58] W.-J. Yin, T. Shi, and Y. Yan, *Unusual defect physics in CH3NH3PbI3 perovskite solar cell absorber*, Applied Physics Letters **104**, 63903 (2014).

[59] K. X. Steirer, P. Schulz, G. Teeter, V. Stevanovic, M. Yang, K. Zhu, and J. J. Berry, *Defect Tolerance in Methylammonium Lead Triiodide Perovskite*, ACS Energy Letters **1**, 360 (2016).

[60] J. Kang and L. W. Wang, *High Defect Tolerance in Lead Halide Perovskite CsPbBr3*, Journal of Physical Chemistry Letters **8**, 489 (2017).

[61] W. Shockley and W. T. Read, *Statistics of the Recombination of Holes and Electrons*, Physical Review **87**, 835 (1952).

[62] R. N. Hall, *Electron-Hole Recombination in Germanium*, Physical Review **87**, 387 (1952).

[63] D. Fitzgerald and A. Grove, *Surface recombination in semiconductors*, Surface Science **9**, 347 (1968).

[64] A. R. Beattie and P. T. Landsberg, *Auger Effect in Semiconductors*, Proceedings of the Royal Society A: Mathematical, Physical and Engineering Sciences **249**, 16 (1959).

[65] J. M. Richter, M. Abdi-Jalebi, A. Sadhanala, M. Tabachnyk, J. P. Rivett, L. M. Pazos-Outón, K. C. Gödel, M. Price, F. Deschler, and R. H. Friend, *Enhancing photoluminescence yields in lead halide perovskites by photon recycling and light out-coupling*, Nature Communications **7**, 13941 (2016).

[66] M. Beard and R. Ellingson, *Multiple exciton generation in semiconductor nanocrystals: Toward efficient solar energy conversion*, Laser & Photonics Review **2**, 377 (2008).

[67] L. M. Herz, *Charge-Carrier Dynamics in Organic-Inorganic Metal Halide Perovskites*, Annual Review of Physical Chemistry **67**, 65 (2016).

[68] L. M. Herz, *Charge-Carrier Mobilities in Metal Halide Perovskites: Fundamental Mechanisms and Limits*, ACS Energy Letters **2**, 1539 (2017).

[69] I. Pelant and J. Valenta, *Luminescence Spectroscopy of Semiconductors*, volume

9780199588, 2012.

[70] C. S. Ponseca, Y. Tian, V. Sundström, and I. G. Scheblykin, *Excited state and charge-carrier dynamics in perovskite solar cell materials*, Nanotechnology **27**, 82001 (2016).

[71] G. W. P. Adhyaksa, S. Brittman, . Haralds, A. Lof, X. Li, T. Duevski, D. P. Fenning, and E. C. Garnett, *Understanding detrimental and beneficial grain boundary effects in halide perovskites*.

[72] M. B. Johnston and L. M. Herz, *Hybrid Perovskites for Photovoltaics: Charge-Carrier Recombination, Diffusion, and Radiative Efficiencies*, Accounts of Chemical Research **49**, 146 (2016).

[73] X. Wu, M. T. Trinh, D. Niesner, H. Zhu, Z. Norman, J. S. Owen, O. Yaffe, B. J. Kudisch, and X. Zhu, *Trap States in Lead Iodide Perovskites*, Journal of the American Chemical Society **137**, 2089 (2015).

[74] J. M. Ball and A. Petrozza, *Defects in perovskite-halides and their effects in solar cells*, Nature Energy **1**, 16149 (2016).

[75] V. Adinolfi, M. Yuan, R. Comin, E. S. Thibau, D. Shi, M. I. Saidaminov, P. Kanjanaboos, D. Kopilovic, S. Hoogland, Z. H. Lu, O. M. Bakr, and E. H. Sargent, *The In-Gap Electronic State Spectrum of Methylammonium Lead Iodide Single-Crystal Perovskites*, Advanced Materials **28**, 3406 (2016).

[76] D. Shi, V. Adinolfi, R. Comin, M. Yuan, E. Alarousu, A. Buin, Y. Chen, S. Hoogland, A. Rothenberger, K. Katsiev, Y. Losovyj, X. Zhang, P. A. Dowben, O. F. Mohammed, E. H. Sargent, and O. M. Bakr, *Low trap-state density and long carrier diffusion in organolead trihalide perovskite single crystals*, Science **347**, 519 (2015).

[77] A. Buin, P. Pietsch, O. Voznyy, R. Comin, A. H. Ip, E. H. Sargent, and B. Xu, *Materials Processing Routes to Trap-free Halide Perovskites*, Nano letters **14**, 6281 (2014).

[78] U. Rau, *Reciprocity relation between photovoltaic quantum efficiency and electroluminescent emission of solar cells*, Physical Review B - Condensed Matter and Materials Physics **76**, 1 (2007).

[79] J. F. Geisz, M. A. Steiner, I. García, S. R. Kurtz, and D. J. Friedman, *Enhanced external radiative efficiency for 20.8% efficient single-junction GaInP solar cells*, Applied Physics Letters **103**, 041118 (2013).

[80] F. Deschler, M. Price, S. Pathak, L. Klintberg, D. D. Jarausch, R. Higler, S. Huettner, T. Leijtens, S. D. Stranks, H. J. Snaith, M. Atature, R. T. Phillips, and R. H. Friend, *High Photoluminescence Efficiency and Optically-Pumped Lasing in Solution-Processed Mixed Halide Perovskite Semiconductors*, The Journal of Physical Chemistry Letters **5**, 1421 (2014).

[81] J. S. Manser and P. V. Kamat, *Band filling with free charge carriers in organometal halide perovskites*, Nature Photonics **8**, 737 (2014).

[82] M. Sheik-Bahae and R. I. Epstein, *Can Laser Light Cool Semiconductors?*, Physical Review Letters **92**, 247403 (2004).

[83] N.-G. Park, M. Grätzel, and T. Miyasaka, editors, *Organic-Inorganic Halide Perovskite Photovoltaics*, Springer International Publishing, Cham, 2016.

[84] W. Zhang, G. E. Eperon, and H. J. Snaith, *Metal halide perovskites for energy applications*, Nature Energy **1**, 16048 (2016).

[85] S. Adjokatse, H. H. Fang, and M. A. Loi, *Broadly tunable metal halide perovskites for solid-state light-emission applications*, Materials Today **20**, 413 (2017).

[86] Y.-H. Kim, H. Cho, and T.-W. Lee, *Metal halide perovskite light emitters*, Proceedings of the National Academy of Sciences **113**, 11694 (2016).

[87] H. Wang and D. H. Kim, *Perovskite-based photodetectors: materials and devices*, Chem.

Soc. Rev. **46**, 5204 (2017).

[88] M. Ahmadi, T. Wu, and B. Hu, *A Review on Organic–Inorganic Halide Perovskite Photodetectors: Device Engineering and Fundamental Physics*, Advanced Materials **29**, 1 (2017).

[89] J.-H. Im, C.-R. Lee, J.-W. Lee, S.-W. Park, and N.-G. Park, *6.5% Efficient Perovskite Quantum-Dot-Sensitized Solar Cell*, Nanoscale **3**, 4088 (2011).

[90] H.-S. Kim, C.-R. Lee, J.-H. Im, K.-B. Lee, T. Moehl, A. Marchioro, S.-J. Moon, R. Humphry-Baker, J.-H. Yum, J. E. Moser, M. Grätzel, and N.-G. Park, *Lead Iodide Perovskite Sensitized All-Solid-State Submicron Thin Film Mesoscopic Solar Cell with Efficiency Exceeding 9%*, Scientific Reports **2**, 591 (2012).

[91] J. M. Ball, M. M. Lee, A. Hey, and H. J. Snaith, *Low-temperature processed meso-superstructured to thin-film perovskite solar cells*, Energy & Environmental Science **6**, 1739 (2013).

[92] S. D. Stranks, G. E. Eperon, G. Grancini, C. Menelaou, M. J. P. Alcocer, T. Leijtens, L. M. Herz, A. Petrozza, and H. J. Snaith, *Electron-hole diffusion lengths exceeding 1 micrometer in an organometal trihalide perovskite absorber*, Science (New York, N.Y.) **342**, 341 (2013).

[93] M. A. Green, *Silicon Solar Cells: Advanced Principles & Practice*, Centre for Photovoltaic Devices and Systems, University of New South Wales, 1995.

[94] J. Mizusaki, K. Arai, and K. Fueki, *Ionic conduction of the perovskite-type halides*, Solid State Ionics **11**, 203 (1983).

[95] T. Ishihara, H. Matsuda, and Y. Takita, *Doped LaGaO3 Perovskite Type Oxide as a New Oxide Ionic Conductor*, Journal of the American Chemical Society **116**, 3801 (1994).

[96] K. Domanski, B. Roose, T. Matsui, M. Saliba, S.-H. Turren-Cruz, J.-P. Correa-Baena, C. R. Carmona, G. Richardson, J. M. Foster, F. De Angelis, J. M. Ball, A. Petrozza, N. Mine, M. K. Nazeeruddin, W. Tress, M. Gratzel, U. Steiner, A. Hagfeldt, and A. Abate, *Migration of cations induces reversible performance losses over day/night cycling in perovskite solar cells*, Energy Environ. Sci. **10**, 604 (2017).

[97] S. Van Reenen, M. Kemerink, and H. J. Snaith, *Modeling Anomalous Hysteresis in Perovskite Solar Cells*, Journal of Physical Chemistry Letters **6**, 3808 (2015).

[98] H. J. Snaith, A. Abate, J. M. Ball, G. E. Eperon, T. Leijtens, N. K. Noel, S. D. Stranks, J. T. W. Wang, K. Wojciechowski, and W. Zhang, *Anomalous hysteresis in perovskite solar cells*, Journal of Physical Chemistry Letters **5**, 1511 (2014).

[99] J. M. Frost, K. T. Butler, and A. Walsh, *Molecular ferroelectric contributions to anomalous hysteresis in hybrid perovskite solar cells*, APL Materials **2**, 081506 (2014).

[100] C. Quarti, E. Mosconi, and F. De Angelis, *Interplay of orientational order and electronic structure in methylammonium lead iodide: Implications for solar cell operation*, Chemistry of Materials **26**, 6557 (2014).

[101] K. Domanski, J. P. Correa-Baena, N. Mine, M. K. Nazeeruddin, A. Abate, M. Saliba, W. Tress, A. Hagfeldt, and M. Graetzel, *Not All That Glitters Is Gold: Metal-Migration-Induced Degradation in Perovskite Solar Cells*, ACS Nano **10**, 6306 (2016).

[102] W. Nie, J.-C. Blancon, A. J. Neukirch, K. Appavoo, H. Tsai, M. Chhowalla, M. A. Alam, M. Y. Sfeir, C. Katan, J. Even, S. Tretiak, J. J. Crochet, G. Gupta, and A. D. Mohite, *Light-activated photocurrent degradation and self-healing in perovskite solar cells*, Nature Communications **7**, 11574 (2016).

[103] W. Tress, *Metal Halide Perovskites as Mixed Electronic-Ionic Conductors: Challenges and Opportunities-From Hysteresis to Memristivity*, The Journal of Physical Chemistry Letters **8**, 3106 (2017).

[104] J.-H. Choy, S.-H. Jeong, M.-H. Park, Y.-H. Kim, C. Wolf, C.-L. Lee, J. H. Heo, A. Sadhanala, N. Myoung, S. Yoo, S. H. Im, R. H. Friend, and T.-W. Lee, *Overcoming the electroluminescence efficiency limitations of perovskite light-emitting diodes*, Science **350**, 1222 (2015).

[105] X. Y. Chin, D. Cortecchia, J. Yin, A. Bruno, and C. Soci, *Lead Iodide Perovskite Light-Emitting Field-Effect Transistor*, Arxiv **6**, Advance (2015).

[106] W. Shockley and H. J. Queisser, *Detailed Balance Limit of Efficiency of p-n Junction Solar Cells*, Journal of Applied Physics **32**, 510 (1961).

[107] A. Sadhanala, S. Ahmad, B. Zhao, N. Giesbrecht, P. Pearce, F. Deschler, R. L. Hoye, K. C. Goedel, T. Bein, P. Docampo, S. E. Dutton, M. De Volder, and R. H. Friend, *Blue-Green Colour Tunable Solution Processable Organolead Chloride-Bromide Mixed Halide Perovskites for Optoelectronic Applications*, Nano Letters , 150803110321002 (2015).

[108] S. D. Stranks and H. J. Snaith, *Metal-halide perovskites for photovoltaic and light-emitting devices*, Nature Nanotechnology **10**, 391 (2015).

[109] S. A. Veldhuis, P. P. Boix, N. Yantara, M. Li, T. C. Sum, N. Mathews, and S. G. Mhaisalkar, *Perovskite Materials for Light-Emitting Diodes and Lasers*, Advanced Materials , 6804 (2016).

[110] X. Hong, T. Ishihara, and A. Nurmikko, *Photoconductivity and electroluminescence in lead iodide based natural quantum well structures*, Solid State Communications **84**, 657 (1992).

[111] M. Era, S. Morimoto, T. Tsutsui, and S. Saito, *Organic-inorganic heterostructure electroluminescent device using a layered perovskite semiconductor*, Applied Physics Letters **65**, 676 (1994).

[112] T. Hattori, T. Taira, M. Era, T. Tsutsui, and S. Saito, *Highly efficient electroluminescence from a heterostructure device combined with emissive layered-perovskite and an electron-transporting organic compound*, Chemical Physics Letters **254**, 103 (1996).

[113] A. Kojima, M. Ikegami, K. Teshima, and T. Miyasaka, *Highly Luminescent Lead Bromide Perovskite Nanoparticles Synthesized with Porous Alumina Media*, Chemistry Letters **41**, 397 (2012).

[114] Z.-K. Tan, R. S. Moghaddam, M. L. Lai, P. Docampo, R. Higler, F. Deschler, M. Price, A. Sadhanala, L. M. Pazos, D. Credgington, F. Hanusch, T. Bein, H. J. Snaith, and R. H. Friend, *Bright light-emitting diodes based on organometal halide perovskite*, Nature Nanotechnology **9**, 1 (2014).

[115] S. Pathak, N. Sakai, F. Wisnivesky Rocca Rivarola, S. D. Stranks, J. Liu, G. Eperon, C. Ducati, K. Wojciechowski, J. T. Griffiths, A. A. Haghighirad, A. Pellaroque, R. H. Friend, and H. J. Snaith, *Perovskite Crystals for Tuneable White Light Emission*, Chemistry of Materials , acs.chemmater.5b03769 (2015).

[116] H. Huang, H. Lin, S. V. Kershaw, A. S. Susha, W. C. H. Choy, and A. L. Rogach, *Polyhedral Oligomeric Silsesquioxane Enhances the Brightness of Perovskite Nanocrystal-Based Green Light-Emitting Devices*, The Journal of Physical Chemistry Letters **7**, 4398 (2016).

[117] J. Wang, N. Wang, Y. Jin, J. Si, Z.-K. Tan, H. Du, L. Cheng, X. Dai, S. Bai, H. He, Z. Ye, M. L. Lai, R. H. Friend, and W. Huang, *Interfacial Control Toward Efficient and Low-Voltage Perovskite Light-Emitting Diodes*, Advanced Materials **27**, 2311 (2015).

[118] Y.-H. Kim, H. Cho, J. H. Heo, T.-S. Kim, N. Myoung, C.-L. Lee, S. H. Im, and T.-W. Lee, *Multicolored Organic/Inorganic Hybrid Perovskite Light-Emitting Diodes*, Advanced Materials **27**, 1248 (2015).

[119] R. L. Z. Hoye, M. R. Chua, K. P. Musselman, G. Li, M.-L. Lai, Z.-K. Tan, N. C. Greenham,

J. L. MacManus-Driscoll, R. H. Friend, and D. Credgington, *Enhanced Performance in Fluorene-Free Organometal Halide Perovskite Light-Emitting Diodes using Tunable, Low Electron Affinity Oxide Electron Injectors*, Advanced Materials **27**, 1414 (2015).

[120] J. C. Yu, D. B. Kim, G. Baek, B. R. Lee, E. D. Jung, S. Lee, J. H. Chu, D.-K. Lee, K. J. Choi, S. Cho, and M. H. Song, *High-Performance Planar Perovskite Optoelectronic Devices: A Morphological and Interfacial Control by Polar Solvent Treatment*, Advanced Materials , n/a (2015).

[121] Z.-F. Shi, X.-G. Sun, D. Wu, T.-T. Xu, S.-W. Zhuang, Y.-T. Tian, X.-J. Li, and G.-T. Du, *High-performance planar green light-emitting diodes based on a PEDOT:PSS/CH 3 NH 3 PbBr 3 /ZnO sandwich structure*, Nanoscale **8**, 10035 (2016).

[122] J. C. Yu, D. B. Kim, E. D. Jung, B. R. Lee, and M. H. Song, *High-performance perovskite light-emitting diodes via morphological control of perovskite films*, Nanoscale **8**, 7036 (2016).

[123] H. Zhu, Y. Fu, F. Meng, X. Wu, Z. Gong, Q. Ding, M. V. Gustafsson, M. T. Trinh, S. Jin, and X.-Y. Zhu, *Lead halide perovskite nanowire lasers with low lasing thresholds and high quality factors*, Nature Materials **14**, 636 (2015).

[124] X. Liu, L. Niu, C. Wu, C. Cong, H. Wang, Q. Zeng, H. He, Q. Fu, W. Fu, T. Yu, C. Jin, Z. Liu, and T. C. Sum, *Periodic Organic-Inorganic Halide Perovskite Microplatelet Arrays on Silicon Substrates for Room-Temperature Lasing*, Advanced Science **3**, 1600137 (2016).

[125] Q. Zhang, S. T. Ha, X. Liu, T. C. Sum, and Q. Xiong, *Room-Temperature Near-Infrared High-Q Perovskite Whispering-Gallery Planar Nanolasers*, Nano Letters **14**, 5995 (2014).

[126] D. Kang, S. R. Pae, J. Shim, G. Yoo, J. Jeon, J. W. Leem, J. S. Yu, S. Lee, B. Shin, and J. Park, *An Ultrahigh-Performance Photodetector based on a Perovskite–Transition-Metal-Dichalcogenide Hybrid Structure*, Advanced Materials (2016).

[127] W. Deng, L. Huang, X. Xu, X. Zhang, X. Jin, S.-T. Lee, and J. Jie, *Ultrahigh-Responsivity Photodetectors from Perovskite Nanowire Arrays for Sequentially Tunable Spectral Measurement*, Nano Letters **17**, 2482 (2017).

[128] L. Dou, Y. M. Yang, J. You, Z. Hong, W.-H. Chang, G. Li, and Y. Yang, *Solution-processed hybrid perovskite photodetectors with high detectivity*, Nature communications **5**, 5404 (2014).

[129] J. Yu, X. Chen, Y. Wang, H. Zhou, M. Xue, Y. Xu, Z. Li, C. Ye, J. Zhang, P. A. van Aken, P. D. Lund, and H. Wang, *A high-performance self-powered broadband photodetector based on a CH 3 NH 3 PbI 3 perovskite/ZnO nanorod array heterostructure*, Journal of Materials Chemistry C **4**, 7302 (2016).

[130] Q. Lin, A. Armin, P. L. Burn, and P. Meredith, *Filterless narrowband visible photodetectors*, Nature Photonics **9**, 687 (2015).

[131] L. Gao, K. Zeng, J. Guo, C. Ge, J. Du, Y. Zhao, C. Chen, H. Deng, Y. He, H. Song, G. Niu, and J. Tang, *Passivated Single-Crystalline CH 3 NH 3 PbI 3 Nanowire Photodetector with High Detectivity and Polarization Sensitivity*, Nano Letters **16**, 7446 (2016).

[132] Y. Fang, Q. Dong, Y. Shao, Y. Yuan, and J. Huang, *Highly narrowband perovskite single-crystal photodetectors enabled by surface-charge recombination*, Nature Photonics **advance on** (2015).

[133] S. Yakunin, M. Sytnyk, D. Kriegner, S. Shrestha, M. Richter, G. J. Matt, H. Azimi, C. J. Brabec, J. Stangl, M. V. Kovalenko, and W. Heiss, *Detection of X-ray photons by solution-processed lead halide perovskites*, Nature Photonics (2015).

[134] L. Shen, Y. Fang, D. Wang, Y. Bai, Y. Deng, M. Wang, Y. Lu, and J. Huang, *A Self-Powered, Sub-nanosecond-Response Solution-Processed Hybrid Perovskite Photodetector for*

Time-Resolved Photoluminescence-Lifetime Detection, Advanced Materials **28**, 10794 (2016).

[135] B. R. Sutherland, A. K. Johnston, A. H. Ip, J. Xu, V. Adinolfi, P. Kanjanaboos, and E. H. Sargent, *Sensitive, Fast, and Stable Perovskite Photodetectors Exploiting Interface Engineering*, ACS Photonics **2**, 1117 (2015).

[136] Y. Fang and J. Huang, *Resolving Weak Light of Sub-picowatt per Square Centimeter by Hybrid Perovskite Photodetectors Enabled by Noise Reduction*, Advanced Materials **27**, 2804 (2015).

[137] Y. Lee, J. Kwon, E. Hwang, C.-H. Ra, W. J. Yoo, J.-H. Ahn, J. H. Park, and J. H. Cho, *High-Performance Perovskite-Graphene Hybrid Photodetector*, Advanced Materials **27**, 41 (2015).

[138] J. Ding and Q. Yan, *Progress in organic-inorganic hybrid halide perovskite single crystal: growth techniques and applications*, Science China Materials **60**, 1063 (2017).

[139] Y. Dang, D. Ju, L. Wang, and X. Tao, *Recent progress in the synthesis of hybrid halide perovskite single crystals*, CrystEngComm **18**, 4476 (2016).

[140] Q. Dong, Y. Fang, Y. Shao, P. Mulligan, J. Qiu, L. Cao, and J. Huang, *Electron-hole diffusion lengths > 175 m in solution-grown CH3NH3PbI3 single crystals*, Science **347**, 967 (2015).

[141] H.-H. Fang, R. Raissa, M. Abdu-Aguye, S. Adjokatse, G. R. Blake, J. Even, and M. A. Loi, *Photophysics of Organic-Inorganic Hybrid Lead Iodide Perovskite Single Crystals*, Advanced Functional Materials **25**, n/a (2015).

[142] D. Valverde-Chavez, C. S. Ponseca, C. Stoumpos, A. Yartsev, M. Kanatzidis, V. Sundstrom, and D. G. Cooke, *Intrinsic femtosecond charge generation dynamics in single crystal CH3NH3PbI3*, Energy Environ. Sci. (2015).

[143] A. A. Zhumekenov, M. I. Saidaminov, M. A. Haque, E. Alarousu, S. P. Sarmah, B. Murali, I. Dursun, X.-H. Miao, A. L. Abdelhady, T. Wu, O. F. Mohammed, and O. M. Bakr, *Formamidinium Lead Halide Perovskite Crystals with Unprecedented Long Carrier Dynamics and Diffusion Length*, ACS Energy Letters **1**, 32 (2016).

[144] Y. Yang, Y. Yan, M. Yang, S. Choi, K. Zhu, J. M. Luther, and M. C. Beard, *Low surface recombination velocity in solution-grown CH3NH3PbBr3 perovskite single crystal*, Nature Communications **6**, 7961 (2015).

[145] Q. Lv, W. He, Z. Lian, J. Ding, Q. Li, and Q. Yan, *Anisotropic moisture erosion of CH 3 NH 3 PbI 3 single crystals*, CrystEngComm **19**, 901 (2017).

[146] Z. Lian, Q. Yan, Q. Lv, Y. Wang, L. Liu, L. Zhang, S. Pan, Q. Li, L. Wang, and J.-L. Sun, *High-Performance Planar-Type Photodetector on (100) Facet of MAPbI 3 Single Crystal*, Scientific Reports **5**, 16563 (2015).

[147] Y. Dang, Y. Liu, Y. Sun, D. Yuan, X. Liu, W. Lu, G. Liu, H. Xia, and X. Tao, *Bulk crystal growth of hybrid perovskite material CH 3 NH 3 PbI 3*, CrystEngComm **17**, 665 (2015).

[148] M. I. Saidaminov, A. L. Abdelhady, G. Maculan, and O. M. Bakr, *Retrograde solubility of formamidinium and methylammonium lead halide perovskites enabling rapid single crystal growth*, Chemical Communications **51**, 17658 (2015).

[149] M. I. Saidaminov, A. L. Abdelhady, B. Murali, E. Alarousu, V. M. Burlakov, W. Peng, I. Dursun, L. Wang, Y. He, G. Maculan, A. Goriely, T. Wu, O. F. Mohammed, and O. M. Bakr, *High-quality bulk hybrid perovskite single crystals within minutes by inverse temperature crystallization*, Nature Communications **6**, 7586 (2015).

[150] G. Maculan, A. D. Sheikh, A. L. Abdelhady, M. I. Saidaminov, M. A. Haque, B. Murali, E. Alarousu, O. F. Mohammed, T. Wu, and O. M. Bakr, *CH 3 NH 3 PbCl 3 Single Crystals: Inverse Temperature Crystallization and Visible-Blind UV-Photodetector*, The Journal

of Physical Chemistry Letters **6**, 3781 (2015).

[151] Q. Han, S.-H. Bae, P. Sun, Y.-T. Hsieh, Y. M. Yang, Y. S. Rim, H. Zhao, Q. Chen, W. Shi, G. Li, and Y. Yang, *Single Crystal Formamidinium Lead Iodide (FAPbI 3): Insight into the Structural, Optical, and Electrical Properties*, Advanced Materials , n/a (2016).

[152] D. N. Dirin, I. Cherniukh, S. Yakunin, Y. Shynkarenko, and M. V. Kovalenko, *Solution-Grown CsPbBr 3 Perovskite Single Crystals for Photon Detection*, Chemistry of Materials **28**, 8470 (2016).

[153] H. Zhou, Z. Nie, J. Yin, Y. Sun, H. Zhuo, D. Wang, D. Li, J. Dou, X. Zhang, and T. Ma, *Antisolvent diffusion-induced growth, equilibrium behaviours in aqueous solution and optical properties of CH 3 NH 3 PbI 3 single crystals for photovoltaic applications*, RSC Advances **5**, 85344 (2015).

[154] N. Sarukura, T. Nawata, H. Ishibashi, M. Ishii, and T. Fukuda, *Czochralski Growth of Oxides and Fluorides*, in *Handbook of Crystal Growth*, pages 131–168, Elsevier, 2015.

[155] M. Jurisch, S. Eichler, and M. Bruder, *Vertical Bridgman Growth of Binary Compound Semiconductors*, in *Handbook of Crystal Growth*, pages 331–372, Elsevier, 2015.

[156] C. C. Stoumpos, C. D. Malliakas, J. A. Peters, Z. Liu, M. Sebastian, J. Im, T. C. Chasapis, A. C. Wibowo, D. Y. Chung, A. J. Freeman, B. W. Wessels, and M. G. Kanatzidis, *Crystal Growth of the Perovskite Semiconductor CsPbBr 3 : A New Material for High-Energy Radiation Detection*, Crystal Growth & Design **13**, 2722 (2013).

[157] W. Peng, L. Wang, B. Murali, K.-T. Ho, A. Bera, N. Cho, C.-F. Kang, V. M. Burlakov, J. Pan, L. Sinatra, C. Ma, W. Xu, D. Shi, E. Alarousu, A. Goriely, J.-H. He, O. F. Mohammed, T. Wu, and O. M. Bakr, *Solution-Grown Monocrystalline Hybrid Perovskite Films for Hole-Transporter-Free Solar Cells*, Advanced Materials **28**, 3383 (2016).

[158] Y. Liu, Y. Zhang, Z. Yang, D. Yang, X. Ren, L. Pang, and S. F. Liu, *Thinness- and Shape-Controlled Growth for Ultrathin Single-Crystalline Perovskite Wafers for Mass Production of Superior Photoelectronic Devices*, Advanced Materials **28**, 9204 (2016).

[159] H.-S. Rao, W.-G. Li, B.-X. Chen, D.-B. Kuang, and C.-Y. Su, *In Situ Growth of 120 cm 2 CH 3 NH 3 PbBr 3 Perovskite Crystal Film on FTO Glass for Narrowband-Photodetectors*, Advanced Materials **29**, 1602639 (2017).

[160] Q. Chen, C. Zhang, M. Zhu, S. Liu, M. E. Siemens, S. Gu, J. Zhu, J. Shen, X. Wu, C. Liao, J. Zhang, X. Wang, and M. Xiao, *Efficient thermal conductance in organometallic perovskite CH3NH3PbI3 films*, Applied Physics Letters **108**, 081902 (2016).

[161] L. Lee, J. Baek, K. S. Park, Y. E. K. Lee, N. K. Shrestha, and M. M. Sung, *Wafer-scale single-crystal perovskite patterned thin films based on geometrically-confined lateral crystal growth*, Nature Communications **8**, 1 (2017).

[162] Y. Zhang, J. Liu, Z. Wang, Y. Xue, Q. Ou, L. Polavarapu, J. Zheng, X. Qi, and Q. Bao, *Synthesis, properties, and optical applications of low-dimensional perovskites*, Chem. Commun. **52**, 13637 (2016).

[163] L. C. Schmidt, A. Pertegás, S. González-Carrero, O. Malinkiewicz, S. Agouram, G. Mínguez Espallargas, H. J. Bolink, R. E. Galian, and J. Pérez-Prieto, *Nontemplate synthesis of CH3NH3PbBr3 perovskite nanoparticles*, Journal of the American Chemical Society **136**, 850 (2014).

[164] S. Gonzalez-Carrero, R. E. Galian, and J. Pérez-Prieto, *Maximizing the emissive properties of CH 3 NH 3 PbBr 3 perovskite nanoparticles*, Journal of Materials Chemistry A **3**, 9187 (2015).

[165] Y. Hassan, Y. Song, R. D. Pensack, A. I. Abdelrahman, Y. Kobayashi, M. A. Winnik, and G. D. Scholes, *Structure-Tuned Lead Halide Perovskite Nanocrystals*, Advanced Materials **28**, 566 (2016).

[166] S. Sun, D. Yuan, Y. Xu, A. Wang, and Z. Deng, *Ligand-Mediated Synthesis of Shape-Controlled Cesium Lead Halide Perovskite Nanocrystals via Reprecipitation Process at Room Temperature*, ACS Nano **10**, 3648 (2016).

[167] M. Spina, E. Bonvin, A. Sienkiewicz, B. Náfrádi, L. Forró, and E. Horváth, *Controlled growth of CH3NH3PbI3 nanowires in arrays of open nanofluidic channels*, Scientific Reports **6**, 19834 (2016).

[168] E. Horváth, M. Spina, Z. Szekrényes, K. Kamarás, R. Gaal, D. Gachet, and L. Forró, *Nanowires of Methylammonium Lead Iodide (CH 3 NH 3 PbI 3) Prepared by Low Temperature Solution-Mediated Crystallization*, Nano Letters **14**, 6761 (2014).

[169] Q. Hu, H. Wu, J. Sun, D. Yan, Y. Gao, and J. Yang, *Large-area perovskite nanowire arrays fabricated by large-scale roll-to-roll micro-gravure printing and doctor blading*, Nanoscale **8**, 5350 (2016).

[170] J.-H. Im, J. Luo, M. Franckevičius, N. Pellet, P. Gao, T. Moehl, S. M. Zakeeruddin, M. K. Nazeeruddin, M. Grätzel, and N.-G. Park, *Nanowire Perovskite Solar Cell*, Nano Letters **15**, 2120 (2015).

[171] A. B. Wong, M. Lai, S. W. Eaton, Y. Yu, E. Lin, L. Dou, A. Fu, and P. Yang, *Growth and Anion Exchange Conversion of CH 3 NH 3 PbX 3 Nanorod Arrays for Light-Emitting Diodes*, Nano Letters **15**, 5519 (2015).

[172] Y. Fu, F. Meng, M. B. Rowley, B. J. Thompson, M. J. Shearer, D. Ma, R. J. Hamers, J. C. Wright, and S. Jin, *Solution Growth of Single Crystal Methylammonium Lead Halide Perovskite Nanostructures for Optoelectronic and Photovoltaic Applications*, Journal of the American Chemical Society (2015).

[173] F. Fu, L. Kranz, S. Yoon, J. Löckinger, T. Jäger, J. Perrenoud, T. Feurer, C. Gretener, S. Bücheler, and A. N. Tiwari, *Controlled growth of PbI 2 nanoplates for rapid preparation of CH3NH3PbI3 in planar perovskite solar cells*, physica status solidi (a) , n/a (2015).

[174] P. Tyagi, S. M. Arveson, and W. A. Tisdale, *Colloidal Organohalide Perovskite Nanoplatelets Exhibiting Quantum Confinement*, The Journal of Physical Chemistry Letters , 150504165839001 (2015).

[175] L. Dou, A. B. Wong, Y. Yu, M. Lai, N. Kornienko, N. S. Ginsberg, L.-w. Wang, A. P. Alivisatos, and P. Yang, *Atomically thin two-dimensional organic-inorganic hybrid perovskites*, Science **349**, 1518 (2015).

[176] Y. Wang, Y. Shi, G. Xin, J. Lian, and J. Shi, *Two-Dimensional van der Waals Epitaxy Kinetics in a Three-Dimensional Perovskite Halide*, Crystal Growth & Design , 150923162617005 (2015).

[177] Q. A. Akkerman, S. G. Motti, A. R. Srimath Kandada, E. Mosconi, V. D'Innocenzo, G. Bertoni, S. Marras, B. A. Kamino, L. Miranda, F. De Angelis, A. Petrozza, M. Prato, and L. Manna, *Solution Synthesis Approach to Colloidal Cesium Lead Halide Perovskite Nanoplatelets with Monolayer-Level Thickness Control*, Journal of the American Chemical Society **138**, 1010 (2016).

[178] S. W. Eaton, M. Lai, N. A. Gibson, A. B. Wong, L. Dou, J. Ma, L.-W. Wang, S. R. Leone, and P. Yang, *Lasing in robust cesium lead halide perovskite nanowires*, Proceedings of the National Academy of Sciences **113**, 1993 (2016).

[179] Q. Liao, K. Hu, H. Zhang, X. Wang, J. Yao, and H. Fu, *Perovskite Microdisk Microlasers Self-Assembled from Solution*, Advanced Materials **27**, 3405 (2015).

[180] J. Xing, X. Liu, Q. Zhang, S. T. Ha, Y. Yuan, C. Shen, T. C. Sum, and Q. Xiong, *Vapor Phase Synthesis of Organometal Halide Perovskite Nanowires for Tunable Room-Temperature Nanolasers*, Nano letters (2015).

[181] Z. Wang, J. Liu, Z.-Q. Xu, Y. Xue, L. Jiang, J. Song, F. Huang, Y. Wang, Y. L. Zhong, Y. Zhang, Y.-B. Cheng, and Q. Bao, *Wavelength-tunable waveguides based on polycrystalline organic–inorganic perovskite microwires*, Nanoscale **8**, 6258 (2016).

[182] L. Gu, M. M. Tavakoli, D. Zhang, Q. Zhang, A. Waleed, Y. Xiao, K.-H. Tsui, Y. Lin, L. Liao, J. Wang, and Z. Fan, *3D Arrays of 1024-Pixel Image Sensors based on Lead Halide Perovskite Nanowires*, Advanced Materials **28**, 9713 (2016).

[183] D. H. Cao, C. C. Stoumpos, O. K. Farha, J. T. Hupp, and M. G. Kanatzidis, *2D Homologous Perovskites as Light-Absorbing Materials for Solar Cell Applications*, Journal of the American Chemical Society **137**, 7843 (2015).

[184] I. C. Smith, E. T. Hoke, D. Solis-Ibarra, M. D. McGehee, and H. I. Karunadasa, *A Layered Hybrid Perovskite Solar-Cell Absorber with Enhanced Moisture Stability*, Angewandte Chemie International Edition **53**, 11232 (2014).

[185] D. H. Cao, C. C. Stoumpos, O. K. Farha, J. T. Hupp, and M. G. Kanatzidis, *Two-dimensional homologous perovskites as light absorbing materials for solar cell applications*, Journal of American Chemical Society (2015).

[186] J. Song, J. Li, X. Li, L. Xu, Y. Dong, and H. Zeng, *Quantum Dot Light-Emitting Diodes Based on Inorganic Perovskite Cesium Lead Halides (\ce{CsPbX3})*, Advanced Materials **27**, 7162 (2015).

[187] W. Deng, X. Xu, X. Zhang, Y. Zhang, X. Jin, L. Wang, S.-T. Lee, and J. Jie, *Organometal Halide Perovskite Quantum Dot Light-Emitting Diodes*, Advanced Functional Materials (2016).

[188] G. Li, Z.-K. Tan, D. Di, M. L. Lai, L. Jiang, J. H.-W. Lim, R. H. Friend, and N. C. Greenham, *Efficient Light-Emitting Diodes Based on Nanocrystalline Perovskite in a Dielectric Polymer Matrix*, Nano Letters **15**, 2640 (2015).

[189] J. H. Noh, S. H. Im, J. H. Heo, T. N. Mandal, and S. I. Seok, *Chemical management for colorful, efficient, and stable inorganic-organic hybrid nanostructured solar cells*, Nano Letters **13**, 1764 (2013).

[190] J. H. Heo, D. H. Song, H. J. Han, S. Y. Kim, J. H. Kim, D. Kim, H. W. Shin, T. K. Ahn, C. Wolf, T.-W. Lee, and S. H. Im, *Planar CH3NH3PbI3 Perovskite Solar Cells with Constant 17.2% Average Power Conversion Efficiency Irrespective of the Scan Rate*, Advanced Materials **27**, 3464 (2015).

[191] S. Ryu, J. H. Noh, N. J. Jeon, Y. C. Kim, W. S. Yang, J. Seo, and S. I. Seok, *Voltage Output of Efficient Perovskite Solar Cells with high Open-Circuit Voltage and Fill Factor*, Energy & Environmental Science **7**, 2614 (2014).

[192] E. Edri, S. Kirmayer, D. Cahen, and G. Hodes, *High open-circuit voltage solar cells based on organic-inorganic lead bromide perovskite*, Journal of Physical Chemistry Letters **4**, 897 (2013).

[193] A. Dymshits, A. Rotem, and L. Etgar, *High voltage in hole conductor free organo metal halide perovskite solar cells*, J. Mater. Chem. A **2**, 20776 (2014).

[194] M. Kulbak, D. Cahen, and G. Hodes, *How Important Is the Organic Part of the Lead Halide Perovskite Photovoltaic Cells? Efficient CsPbBr3 Cells*, The Journal of Physical Chemistry Letters , 150610174239009 (2015).

[195] N. Yantara, S. Bhaumik, F. Yan, D. Sabba, H. A. Dewi, N. Mathews, P. P. Boix, H. V. Demir, and S. Mhaisalkar, *Inorganic Halide Perovskites for Efficient Light-Emitting Diodes*, The Journal of Physical Chemistry Letters **6**, 4360 (2015).

[196] G. Grancini, A. R. Srimath Kandada, J. M. Frost, A. J. Barker, M. De Bastiani, M. Gandini, S. Marras, G. Lanzani, A. Walsh, and A. Petrozza, *Role of microstructure in the electron–hole interaction of hybrid lead halide perovskites*, Nature Photonics **7**, 695

(2015).

[197] J. S. Yun, A. Ho-Baillie, S. Huang, S. Woo, Y. Heo, J. Seidel, F. Huang, Y.-B. Cheng, and M. A. Green, *The Benefit of Grain Boundaries in Organic-Inorganic Halide Planar Perovskite Solar Cells*, The Journal of Physical Chemistry Letters (2015).

[198] J. Huang, Y. Shao, and Q. Dong, *Organometal Trihalide Perovskite Single Crystals: A Next Wave of Materials for 25% Efficiency Photovoltaics and Applications Beyond?*, Journal of Physical Chemistry Letters **6**, 3218 (2015).

[199] P. Zhao, J. Xu, X. Dong, L. Wang, W. Ren, L. Bian, and A. Chang, *Large-size CH3NH3PbBr3 Single Crystal: Growth and In Situ Characterization of the Photophysics Properties*, The Journal of Physical Chemistry Letters (2015).

[200] H. Kunugita, T. Hashimoto, Y. Kiyota, Y. Udagawa, Y. Takeoka, Y. Nakamura, J. Sano, T. Matsushita, T. Kondo, T. Miyasaka, and K. Ema, *Excitonic Feature in Hybrid Perovskite CH3NH3PbBr3 Single Crystals*, Chemistry Letters **44**, 852 (2015).

[201] Y. Yamada, T. Yamada, L. Q. Phuong, N. Maruyama, H. Nishimura, A. Wakamiya, Y. Murata, and Y. Kanemitsu, *Dynamic Optical Properties of CH3NH3PbI3 Single Crystals as Revealed by One- and Two-photon Excited Photolumines-cence Measurements*, Journal of the American Chemical Society **137**, 10456 (2015).

[202] G. Grancini, V. D'Innocenzo, E. R. Dohner, N. Martino, A. R. Srimath Kandada, E. Mosconi, F. De Angelis, H. I. Karunadasa, E. T. Hoke, and A. Petrozza, *CH3NH3PbI3 Perovskite Single Crystals: Surface Photophysics and its Interaction with the Environment*, Chem. Sci. (2015).

[203] T. Zhang, M. Yang, E. E. Benson, Z. Li, J. van de Lagemaat, J. M. Luther, Y. Yan, K. Zhu, and Y. Zhao, *A facile solvothermal growth of single crystal mixed halide perovskite CH 3 NH 3 Pb(Br 1x Cl x) 3*, Chemical Communications **51**, 7820 (2015).

[204] S. Brittman and E. C. Garnett, *Measuring n and k at the Microscale in Single Crystals of CH 3 NH 3 PbBr 3 Perovskite*, The Journal of Physical Chemistry C **120**, 616 (2016).

[205] D. J. Dingley and V. Randle, *Microtexture determination by electron back-scatter diffraction*, Journal of Materials Science **27**, 4545 (1992).

[206] A. J. Schwartz, M. Kumar, B. L. Adams, and D. P. Field, editors, *Electron Backscatter Diffraction in Materials Science*, Springer US, Boston, MA, 2009.

[207] P. Schulz, E. Edri, S. Kirmayer, G. Hodes, D. Cahen, and A. Kahn, *Interface energetics in organo-metal halide perovskite-based photovoltaic cells*, Energy & Environmental Science **7**, 1377 (2014).

[208] C.-C. Chueh, C.-Z. Li, and A. K.-Y. Jen, *Recent Progress and Perspective in Solution-Processed Interfacial Materials for Efficient and Stable Polymer and Organometal Perovskite Solar Cells*, Energy Environ. Sci. **8**, 1160 (2015).

[209] T. Shi, W.-J. Yin, F. Hong, K. Zhu, and Y. Yan, *Unipolar self-doping behavior in perovskite CH3NH3PbBr3*, 2015.

[210] N. Kedem, T. M. Brenner, M. Kulbak, N. Schaefer, S. Levcenko, I. Levine, D. Abou-Ras, G. Hodes, and D. Cahen, *Light-Induced Increase of Electron Diffusion Length in a p-n Junction Type CH3NH3PbBr3 Perovskite Solar Cell*, The Journal of Physical Chemistry Letters , 150610174034007 (2015).

[211] O. Knop, R. E. Wasylishen, M. A. White, T. S. Cameron, and M. J. M. V. Oort, *Alkylammonium lead halides. Part 2. CH3NH3PbX3 (X = Cl, Br, I) perovskites: cuboctahedral halide cages with isotropic cation reorientation*, Canadian Journal of Chemistry **68**, 412 (1990).

[212] P. Khoram, S. Brittman, W. Dzik, J. Reek, and E. Garnett, *Growth and Characterization of PDMS-Stamped Halide Perovskite Single Microcrystals*, Journal of Physical

Chemistry C **120** (2016).
[213] *Bruker*, 2014.
[214] G. M. Sheldrick, *SADABS: Area-Detector Absorption Correction*, Universität Göttingen, Germany, 1999.
[215] G. M. Sheldrick, *SHELXT*, Universität Göttingen, Germany, 2012.
[216] A. Goldmann, editor, *Subvolume B*, volume 23b of *Landolt-Börnstein - Group III Condensed Matter*, Springer-Verlag, Berlin/Heidelberg, 1994.
[217] S. M. Sze and K. Kwok, *Physics of Semiconductor Devices*, Number 1, 2007.
[218] G. F. Burkhard, E. T. Hoke, and M. D. McGehee, *Accounting for Interference, Scattering, and Electrode Absorption to Make Accurate Internal Quantum Efficiency Measurements in Organic and Other Thin Solar Cells*, Advanced Materials **22**, 3293 (2010).
[219] D. W. Lynch, C. G. Olson, and J. H. Weaver, *Optical properties of Ti, Zr, and Hf from 0.15 to 30 eV*, Physical Review B **11**, 3617 (1975).
[220] D. W. de Quilettes et al., *Impact of microstructure on local carrier lifetime in perovskite solar cells*, Science **348**, 683 (2015).
[221] K. Wojciechowski, S. D. Stranks, A. Abate, G. Sadoughi, A. Sadhanala, N. Kopidakis, G. Rumbles, C.-Z. Li, R. H. Friend, A. K.-Y. Jen, and H. J. Snaith, *Heterojunction Modification for Highly Efficient Organic–Inorganic Perovskite Solar Cells*, ACS Nano **8**, 12701 (2014).
[222] B. Conings, J. Drijkoningen, N. Gauquelin, A. Babayigit, J. D'Haen, L. D'Olieslaeger, A. Ethirajan, J. Verbeeck, J. Manca, E. Mosconi, F. De Angelis, and H. G. Boyen, *Intrinsic Thermal Instability of Methylammonium Lead Trihalide Perovskite*, Advanced Energy Materials **5**, 1 (2015).
[223] G. E. Eperon, S. N. Habisreutinger, T. Leijtens, B. J. Bruijnaers, J. J. Van Franeker, D. W. Dequilettes, S. Pathak, R. J. Sutton, G. Grancini, D. S. Ginger, R. A. J. Janssen, A. Petrozza, and H. J. Snaith, *The Importance of Moisture in Hybrid Lead Halide Perovskite Thin Film Fabrication*, ACS Nano **9**, 9380 (2015).
[224] E. T. Hoke, D. J. Slotcavage, E. R. Dohner, A. R. Bowring, H. I. Karunadasa, and M. D. McGehee, *Reversible photo-induced trap formation in mixed-halide hybrid perovskites for photovoltaics*, Chemical Science **6**, 613 (2015).
[225] T. Leijtens, G. E. Eperon, N. K. Noel, S. N. Habisreutinger, A. Petrozza, and H. J. Snaith, *Stability of metal halide perovskite solar cells*, Advanced Energy Materials **5**, 1500963 (2015).
[226] C. Eames, J. M. Frost, P. R. F. Barnes, B. C. O'Regan, A. Walsh, and M. S. Islam, *Ionic transport in hybrid lead iodide perovskite solar cells*, Nature Communications **6**, 7497 (2015).
[227] J. Yang, B. D. Siempelkamp, D. Liu, and T. L. Kelly, *An Investigation of CH3NH3PbI3 Degradation Rates and Mechanisms in Controlled Humidity Environments Using in situ Techniques.*, ACS nano , Advance (2015).
[228] S. Meloni, T. Moehl, W. Tress, M. Franckevičius, M. Saliba, Y. H. Lee, P. Gao, M. K. Nazeeruddin, S. M. Zakeeruddin, U. Rothlisberger, and M. Graetzel, *Ionic polarization-induced current–voltage hysteresis in CH3NH3PbX3 perovskite solar cells*, Nature Communications **7**, 1 (2016).
[229] W. Tress, N. Marinova, T. Moehl, S. M. Zakeeruddin, M. K. Nazeeruddin, and M. Grätzel, *Understanding the rate-dependent J–V hysteresis, slow time component, and aging in CH3NH3PbI3 perovskite solar cells: the role of a compensated electric field*, Energy Environ. Sci. **8**, 995 (2015).
[230] A. Walsh, D. O. Scanlon, S. Chen, X. G. Gong, and S. H. Wei, *Self-regulation*

mechanism for charged point defects in hybrid halide perovskites, Angewandte Chemie - International Edition **54**, 1791 (2015).

[231] M. Cherry, M. Islam, and C. Catlow, *Oxygen Ion Migration in Perovskite-Type Oxides*, 1995.

[232] J.-P. Correa-Baena, A. Abate, M. Saliba, W. Tress, T. Jesper Jacobsson, M. Grätzel, and A. Hagfeldt, *The rapid evolution of highly efficient perovskite solar cells*, Energy Environ. Sci. **10**, 710 (2017).

[233] J. Yan, X. Ke, Y. Chen, A. Zhang, and B. Zhang, *Effect of modulating the molar ratio of organic to inorganic content on morphology, optical absorption and photoluminescence of perovskite CH3NH3PbBr3 films*, Applied Surface Science **351**, 1191 (2015).

[234] Y. Yuan, J. Chae, Y. Shao, Q. Wang, Z. Xiao, A. Centrone, and J. Huang, *Photovoltaic Switching Mechanism in Lateral Structure Hybrid Perovskite Solar Cells*, Advanced Energy Materials **5**, 1 (2015).

[235] D. W. DeQuilettes, W. Zhang, V. M. Burlakov, D. J. Graham, T. Leijtens, A. Osherov, V. Bulović, H. J. Snaith, D. S. Ginger, and S. D. Stranks, *Photo-induced halide redistribution in organic–inorganic perovskite films*, Nature Communications **7**, 1 (2016).

[236] C. Li, S. Tscheuschner, F. Paulus, P. E. Hopkinson, J. Kieling, A. Khler, Y. Vaynzof, and S. Huettner, *Iodine Migration and its Effect on Hysteresis in Perovskite Solar Cells*, Advanced Materials **28**, 2446 (2016).

[237] A. Benninghoven, *Chemical Analysis of Inorganic and Organic Surfaces and Thin Films by Static Time-of-Flight Secondary Ion Mass Spectrometry (TOF-SIMS)*, Angewandte Chemie International Edition in English **33**, 1023 (1994).

[238] T. Glaser, C. Müller, M. Sendner, C. Krekeler, O. E. Semonin, T. D. Hull, O. Yaffe, J. S. Owen, W. Kowalsky, A. Pucci, and R. Lovrinčić, *Infrared Spectroscopic Study of Vibrational Modes in Methylammonium Lead Halide Perovskites*, The Journal of Physical Chemistry Letters **6**, 2913 (2015).

[239] N. Klein-Kedem, D. Cahen, and G. Hodes, *Effects of Light and Electron Beam Irradiation on Halide Perovskites and Their Solar Cells*, Accounts of Chemical Research **49**, 347 (2016).

[240] Y. Luo, S. Gamliel, S. Nijem, S. Aharon, M. Holt, B. Stripe, V. Rose, M. I. Bertoni, L. Etgar, and D. P. Fenning, *Spatially Heterogeneous Chlorine Incorporation in Organic-Inorganic Perovskite Solar Cells*, Chemistry of Materials **28**, 6536 (2016).

[241] R. P. Winarski, M. V. Holt, V. Rose, P. Fuesz, D. Carbaugh, C. Benson, D. Shu, D. Kline, G. B. Stephenson, I. McNulty, and J. Maser, *A hard X-ray nanoprobe beamline for nanoscale microscopy*, Journal of Synchrotron Radiation **19**, 1056 (2012).

[242] M. Stuckelberger, B. West, T. Nietzold, B. Lai, J. M. Maser, V. Rose, and M. I. Bertoni, *Review: Engineering Solar Cells Based on Correlative X-Ray Microscopy*, Journal of Materials Research **32**, 1825 (2017).

[243] S. Mastroianni, F. D. Heinz, J.-H. Im, W. Veurman, M. Padilla, M. C. Schubert, U. Würfel, M. Grätzel, N.-G. Park, and A. Hinsch, *Analysing the effect of crystal size and structure in highly efficient CH3NH3PbI3 perovskite solar cells by spatially resolved photo- and electroluminescence imaging*, Nanoscale , 19653 (2015).

[244] A. M. Soufiani, Z. Hameiri, S. Meyer, S. Lim, M. J. Y. Tayebjee, J. S. Yun, A. Ho-Baillie, G. J. Conibeer, L. Spiccia, and M. A. Green, *Lessons Learnt from Spatially Resolved Electro- and Photoluminescence Imaging: Interfacial Delamination in CH3NH3PbI3 Planar Perovskite Solar Cells upon Illumination*, Advanced Energy Materials , 1 (2016).

[245] A. M. Soufiani, M. J. Y. Tayebjee, S. Meyer, A. Ho-Baillie, J. Sung Yun, R. W. McQueen,

L. Spiccia, M. A. Green, and Z. Hameiri, *Electro- and photoluminescence imaging as fast screening technique of the layer uniformity and device degradation in planar perovskite solar cells*, Journal of Applied Physics **120** (2016).

[246] M. A. Green, *Radiative efficiency of state-of-the-art photovoltaic cells*, Prog. Photovolt: Res. Appl. **20**, 472 (2012).

[247] J. Li, Q. Dong, N. Li, and L. Wang, *Direct Evidence of Ion Diffusion for the Silver-Electrode-Induced Thermal Degradation of Inverted Perovskite Solar Cells*, Advanced Energy Materials , 1 (2017).

[248] K. Ando, A. Yamamoto, and M. Yamaguchi, *Surface Band Bending Effects on Photoluminescence Intensity in n-InP Schottky and MIS Diodes*, Japanese Journal of Applied Physics **20**, 1107 (1981).

[249] I. E. Beckers, U. Fiedeler, S. Siebentritt, and M. C. Lux-Steiner, *Voltage dependent electromodulated photoluminescence of chalcopyrite solar cells*, Journal of Physics and Chemistry of Solids **64**, 2031 (2003).

[250] N. N. Winogradoff, *Field Control of the Quantum Efficiency of Radiative Recombination in Semiconductors*, Physical Review **138**, A1562 (1965).

[251] J. Yan, B. Zhang, Y. Chen, A. Zhang, and X. Ke, *Improving the Photoluminescence Properties of Perovskite CH3NH3PbBr3-xClx Films by Modulating Organic Cation and Chlorine Concentrations*, ACS Applied Materials and Interfaces **8**, 12756 (2016).

[252] K. Zheng, M. Abdellah, Q. Zhu, Q. Kong, G. Jennings, C. A. Kurtz, M. E. Messing, Y. Niu, D. J. Gosztola, M. J. Al-Marri, X. Zhang, T. Pullerits, and S. E. Canton, *Direct Experimental Evidence for Photoinduced Strong-Coupling Polarons in Organolead Halide Perovskite Nanoparticles*, The Journal of Physical Chemistry Letters **7**, 4535 (2016).

[253] J. Haruyama, K. Sodeyama, L. Han, and Y. Tateyama, *First-principles study of ion diffusion in perovskite solar cell sensitizers*, Journal of the American Chemical Society **137**, 10048 (2015).

[254] J.-H. Yang, W.-J. Yin, J.-S. Park, and S.-H. Wei, *Fast self-diffusion of ions in CH ₃ NH ₃ PbI ₃ : the interstiticaly mechanism versus vacancy-assisted mechanism*, J. Mater. Chem. A **4**, 13105 (2016).

[255] Z. Deng, B. Radhakrishnan, and S. P. Ong, *Rational Composition Optimization of the Lithium-Rich Li ₃ OCl _{1– x} Br _x Anti-Perovskite Superionic Conductors*, Chemistry of Materials **27**, 3749 (2015).

[256] H. Mashiyama, Y. Kawamura, H. Kasano, T. Asahi, Y. Noda, and H. Kimura, *Disordered Configuration of Methylammonium of CH3NH3PbBr3 Determined by Single Crystal Neutron Diffractometry*, Ferroelectrics **348**, 182 (2007).

[257] T. J. Jacobsson, J.-P. Correa-Baena, E. Halvani Anaraki, B. Philippe, S. D. Stranks, M. E. F. Bouduban, W. Tress, K. Schenk, J. Teuscher, J.-E. Moser, H. Rensmo, and A. Hagfeldt, *Unreacted PbI 2 as a Double-Edged Sword for Enhancing the Performance of Perovskite Solar Cells*, Journal of the American Chemical Society **138**, 10331 (2016).

[258] G. Kresse and J. Furthmüller, *Efficient iterative schemes for ab initio total-energy calculations using a plane-wave basis set*, Physical Review B **54**, 11169 (1996).

[259] P. E. Blöchl, *Projector augmented-wave method*, Physical Review B **50**, 17953 (1994).

[260] J. P. Perdew, K. Burke, and M. Ernzerhof, *Generalized Gradient Approximation Made Simple*, Physical Review Letters **77**, 3865 (1996).

[261] S. P. Ong, W. D. Richards, A. Jain, G. Hautier, M. Kocher, S. Cholia, D. Gunter, V. L. Chevrier, K. A. Persson, and G. Ceder, *Python Materials Genomics (pymatgen): A robust, open-source python library for materials analysis*, Computational Materials

Science **68**, 314 (2013).

[262] T. M. Brenner, D. A. Egger, L. Kronik, G. Hodes, and D. Cahen, *Hybrid organic—inorganic perovskites: low-cost semiconductors with intriguing charge-transport properties*, Nature Reviews Materials **1**, 15007 (2016).

[263] S. A. Mann, R. R. Grote, R. M. Osgood, A. Alù, and E. C. Garnett, *Opportunities and Limitations for Nanophotonic Structures To Exceed the Shockley–Queisser Limit*, ACS Nano **10**, 8620 (2016).

[264] M. L. Brongersma, Y. Cui, and S. Fan, *Light management for photovoltaics using high-index nanostructures*, Nature Materials **13**, 451 (2014).

[265] V. E. Ferry, M. A. Verschuuren, H. B. T. Li, E. Verhagen, R. J. Walters, R. E. I. Schropp, H. A. Atwater, and A. Polman, *Light trapping in ultrathin plasmonic solar cells*, Optics Express **18**, A237 (2010).

[266] S. A. Mann and E. C. Garnett, *Extreme Light Absorption in Thin Semiconductor Films Wrapped around Metal Nanowires*, Nano Letters **13**, 3173 (2013).

[267] E. Garnett and P. Yang, *Light Trapping in Silicon Nanowire Solar Cells*, Nano Letters **10**, 1082 (2010).

[268] J. Wallentin, N. Anttu, D. Asoli, M. Huffman, I. rAberg, M. H. Magnusson, G. Siefer, P. Fuss-Kailuweit, F. Dimroth, B. Witzigmann, H. Q. Xu, L. Samuelson, K. Deppert, and M. T. Borgström, *InP nanowire array solar cells achieving 13.8% efficiency by exceeding the ray optics limit*, Science **339**, 1057 (2013).

[269] A. Polman and H. a. Atwater, *Photonic design principles for ultrahigh-efficiency photovoltaics*, 2012.

[270] Z. Yu, A. Raman, and S. Fan, *Fundamental limit of nanophotonic light trapping in solar cells*, Proceedings of the National Academy of Sciences **107**, 17491 (2010).

[271] S. A. Mann and E. C. Garnett, *Resonant nanophotonic spectrum splitting for ultrathin multijunction solar cells*, ACS Photonics **2**, 816 (2015).

[272] D. Zhang, Y. Yu, Y. Bekenstein, A. B. Wong, A. P. Alivisatos, and P. Yang, *Ultrathin Colloidal Cesium Lead Halide Perovskite Nanowires*, Journal of the American Chemical Society **138**, 13155 (2016).

[273] A. A. Petrov, N. Pellet, J. Y. Seo, N. A. Belich, D. Y. Kovalev, A. V. Shevelkov, E. A. Goodilin, S. M. Zakeeruddin, A. B. Tarasov, and M. Graetzel, *New Insight into the Formation of Hybrid Perovskite Nanowires via Structure Directing Adducts*, Chemistry of Materials **29**, 587 (2017).

[274] K. Park, J. W. Lee, J. D. Kim, N. S. Han, D. M. Jang, S. Jeong, J. Park, and J. K. Song, *Light–Matter Interactions in Cesium Lead Halide Perovskite Nanowire Lasers*, The Journal of Physical Chemistry Letters **7**, 3703 (2016).

[275] H. Deng, D. Dong, K. Qiao, L. Bu, B. Li, D. Yang, H.-E. Wang, Y. Cheng, Z. Zhao, J. Tang, and H. Song, *Growth, patterning and alignment of organolead iodide perovskite nanowires for optoelectronic devices*, Nanoscale **7**, 4163 (2015).

[276] M. J. Ashley, M. N. O'Brien, K. R. Hedderick, J. A. Mason, M. B. Ross, and C. A. Mirkin, *Templated Synthesis of Uniform Perovskite Nanowire Arrays*, Journal of the American Chemical Society **138**, 10096 (2016).

[277] A. Waleed, M. M. Tavakoli, L. Gu, Z. Wang, D. Zhang, A. Manikandan, Q. Zhang, R.-J. Zhang, Y.-L. Chueh, and Z. Fan, *Lead-Free Perovskite Nanowire Array Photodetectors with Drastically Improved Stability in Nanoengineering Templates*, Nano Letters **17**, 523 (2017).

[278] M. M. Tavakoli, A. Waleed, L. Gu, D. Zhang, R. Tavakoli, B. Lei, W. Su, F. Fang, and Z. Fan, *A non-catalytic vapor growth regime for organohalide perovskite nanowires*

using anodic aluminum oxide templates, Nanoscale **9**, 5828 (2017).

[279] E. Lafalce, C. Zhang, Y. Zhai, D. Sun, and Z. V. Vardeny, *Enhanced emissive and lasing characteristics of nano-crystalline MAPbBr3films grown via anti-solvent precipitation*, Journal of Applied Physics **120**, 143101 (2016).

[280] L. Wen, R. Xu, Y. Mi, and Y. Lei, *Multiple nanostructures based on anodized aluminium oxide templates*, Nature Nanotechnology **12**, 244 (2017).

[281] J. W. Elam, D. Routkevitch, P. P. Mardilovich, and S. M. George, *Conformal coating on ultrahigh-aspect-ratio nanopores of anodic alumina by atomic layer deposition*, Chemistry of Materials **15**, 3507 (2003).

[282] W. Lee and S.-J. Park, *Porous Anodic Aluminum Oxide: Anodization and Templated Synthesis of Functional Nanostructures*, Chemical Reviews **114**, 7487 (2014).

[283] H. Masuda, A. Abe, M. Nakao, A. Yokoo, T. Tamamura, and K. Nishio, *Ordered mosaic nanocomposites in anodic porous alumina*, Advanced Materials **15**, 161 (2003).

[284] T. Yanagishita, M. Sasaki, K. Nishio, and H. Masuda, *Carbon Nanotubes with a Triangular Cross-section, Fabricated Using Anodic Porous Alumina as the Template*, Advanced Materials **16**, 429 (2004).

[285] J. T. Smith, Q. Hang, A. D. Franklin, D. B. Janes, and T. D. Sands, *Highly ordered diamond and hybrid triangle-diamond patterns in porous anodic alumina thin films*, Applied Physics Letters **93**, 043108 (2008).

[286] H. Robatjazi, S. M. Bahauddin, L. H. Macfarlan, S. Fu, and I. Thomann, *Ultrathin AAO Membrane as a Generic Template for Sub-100 nm Nanostructure Fabrication*, Chemistry of Materials **28**, 4546 (2016).

[287] M. Tian, S. Xu, J. Wang, N. Kumar, E. Wertz, Q. Li, P. M. Campbell, M. H. Chan, and T. E. Mallouk, *Penetrating the oxide barrier in situ and separating freestanding porous anodic alumina films in one step*, Nano Letters **5**, 697 (2005).

[288] Y. Guo, K. Shoyama, W. Sato, Y. Matsuo, K. Inoue, K. Harano, C. Liu, H. Tanaka, and E. Nakamura, *Chemical Pathways Connecting Lead(II) Iodide and Perovskite via Polymeric Plumbate(II) Fiber*, Journal of the American Chemical Society **137**, 15907 (2015).

[289] N. J. Jeon, J. H. Noh, Y. C. Kim, W. S. Yang, S. Ryu, and S. I. Seok, *inorganic – organic hybrid perovskite solar cells*, **13**, 897 (2014).

[290] B. Jeong, I. Hwang, S. H. Cho, E. H. Kim, S. Cha, J. Lee, H. S. Kang, S. M. Cho, H. Choi, and C. Park, *Solvent-Assisted Gel Printing for Micropatterning Thin Organic–Inorganic Hybrid Perovskite Films*, ACS Nano **10**, 9026 (2016).

[291] S. T. Williams, C. C. Chueh, and A. K.-Y. Jen, *Navigating Organo-Lead Halide Perovskite Phase Space via Nucleation Kinetics toward a Deeper Understanding of Perovskite Phase Transformations and Structure-Property Relationships*, 2015.

[292] M. Ko, S. H. Baek, B. Song, J. W. Kang, S. A. Kim, and C. H. Cho, *Periodically Diameter-Modulated Semiconductor Nanowires for Enhanced Optical Absorption*, Advanced Materials **28**, 2504 (2016).

[293] L. Cao, J. S. White, J.-S. Park, J. A. Schuller, B. M. Clemens, and M. L. Brongersma, *Engineering light absorption in semiconductor nanowire devices*, Nature Materials **8**, 643 (2009).

[294] D. I. Woodward and I. M. Reaney, *Electron diffraction of tilted perovskites*, 2005.

[295] Y. Yu, D. Zhang, C. Kisielowski, L. Dou, N. Kornienko, Y. Bekenstein, A. B. Wong, A. P. Alivisatos, and P. Yang, *Atomic Resolution Imaging of Halide Perovskites*, Nano Letters **16**, 7530 (2016).

[296] S. A. Mann, B. Sciacca, Y. Zhang, J. Wang, E. Kontoleta, H. Liu, and E. C.

Garnett, *Integrating Sphere Microscopy for Direct Absorption Measurements of Single Nanostructures,* ACS Nano **11**, 1412 (2017).

[297] S. A. Mann, S. Z. Oener, A. Cavalli, J. E. Haverkort, E. P. Bakkers, and E. C. Garnett, *Quantifying losses and thermodynamic limits in nanophotonic solar cells*, Nature Nanotechnology **11**, 1071 (2016).

[298] Y. Luo, P. Khoram, S. Brittman, Z. Zhu, B. Lai, S. P. Ong, E. C. Garnett, and D. P. Fenning, *Direct Observation of Halide Migration and its Effect on the Photoluminescence of Methylammonium Lead Bromide Perovskite Single Crystals*, Advanced Materials **29**, 1703451 (2017).

[299] H. Tsai, W. Nie, Y.-H. Lin, J. C. Blancon, S. Tretiak, J. Even, G. Gupta, P. M. Ajayan, and A. D. Mohite, *Effect of Precursor Solution Aging on the Crystallinity and Photovoltaic Performance of Perovskite Solar Cells*, Advanced Energy Materials **7**, 1602159 (2017).

[300] G. Namkoong, A. A. Mamun, T. T. Ava, K. Zhang, and H. Baumgart, *Impact of perovskite precursor solution temperature on charge carrier dynamics and photovoltaic performance of perovskite based solar cells*, Organic Electronics: physics, materials, applications **42**, 228 (2017).

[301] B. E. Cohen and L. Etgar, *Parameters that control and influence the organo-metal halide perovskite crystallization and morphology*, Frontiers of Optoelectronics **9**, 44 (2016).

[302] J. Huang, X. Yu, J. Xie, D. Xu, Z. Tang, C. Cui, and D. Yang, *Ambient Engineering for High-Performance Organic-Inorganic Perovskite Hybrid Solar Cells*, ACS Applied Materials and Interfaces **8**, 21505 (2016).

[303] J. Shi, X. Xu, D. Li, and Q. Meng, *Interfaces in Perovskite Solar Cells*, Small (2015).

[304] N. K. Noel, A. Abate, S. D. Stranks, E. S. Parrott, V. M. Burlakov, A. Goriely, and H. J. Snaith, *Enhanced photoluminescence and solar cell performance via Lewis base passivation of organic-inorganic lead halide perovskites*, ACS Nano **8**, 9815 (2014).

[305] A. Abate, M. Saliba, D. J. Hollman, S. D. Stranks, K. Wojciechowski, R. Avolio, G. Grancini, A. Petrozza, and H. J. Snaith, *Supramolecular halogen bond passivation of organic-inorganic halide perovskite solar cells*, Nano Letters **14**, 3247 (2014).

[306] K. Oura, M. Katayama, A. V. Zotov, V. G. Lifshits, and A. A. Saranin, *Surface Science*, Advanced Texts in Physics, Springer Berlin Heidelberg, Berlin, Heidelberg, 2003.

[307] P. Cui, P. Fu, D. Wei, M. Li, D. Song, X. Yue, Y. Li, Z. Zhang, Y. Li, and J. M. Mbengue, *Reduced surface defects of organometallic perovskite by thermal annealing for highly efficient perovskite solar cells*, RSC Advances **5**, 75622 (2015).

[308] H.-H. Fang, S. Adjokatse, H. Wei, J. Yang, G. R. Blake, J. Huang, J. Even, and M. A. Loi, *Ultrahigh sensitivity of methylammonium lead tribromide perovskite single crystals to environmental gases*, Science Advances **2**, e1600534 (2016).

[309] R. S. Bonilla, C. Reichel, M. Hermle, and P. R. Wilshaw, *Electric Field Effect Surface Passivation for Silicon Solar Cells*, Solid State Phenomena **205-206**, 346 (2013).

[310] A. G. Aberle, *Surface passivation of crystalline silicon solar cells: a review*, Progress in Photovoltaics: Research and Applications **8**, 473 (2000).

[311] A. G. Aberle, *Overview on SiN surface passivation of crystalline silicon solar cells*, Solar Energy Materials and Solar Cells **65**, 239 (2001).

[312] W. Soppe, H. Rieffe, and A. Weeber, *Bulk and surface passivation of silicon solar cells accomplished by silicon nitride deposited on industrial scale by microwave PECVD*, Progress in Photovoltaics: Research and Applications **13**, 551 (2005).

[313] J. Schmidt, F. Werner, B. Veith, D. Zielke, S. Steingrube, P. Altermatt, S. Gatz, T. Dullweber, and R. Brendel, *Advances in the Surface Passivation of Silicon Solar Cells*,

Energy Procedia **15**, 30 (2012).

[314] M. L. Huang, Y. C. Chang, C. H. Chang, Y. J. Lee, P. Chang, J. Kwo, T. B. Wu, and M. Hong, *Surface passivation of III-V compound semiconductors using atomic-layer-deposition-grown Al2O3*, Applied Physics Letters **87**, 252104 (2005).

[315] J. Xu, A. Buin, A. H. Ip, W. Li, O. Voznyy, R. Comin, M. Yuan, S. Jeon, Z. Ning, J. J. McDowell, P. Kanjanaboos, J.-P. Sun, X. Lan, L. N. Quan, D. H. Kim, I. G. Hill, P. Maksymovych, and E. H. Sargent, *Perovskite–fullerene hybrid materials suppress hysteresis in planar diodes*, Nature Communications **6**, 7081 (2015).

[316] Y. Shao, Z. Xiao, C. Bi, Y. Yuan, and J. Huang, *Origin and elimination of photocurrent hysteresis by fullerene passivation in CH3NH3PbI3 planar heterojunction solar cells*, Nature Communications **5**, 5784 (2014).

[317] J. Peng, Y. Wu, W. Ye, D. A. Jacobs, H. Shen, X. Fu, Y. Wan, T. Duong, N. Wu, C. Barugkin, H. T. Nguyen, D. Zhong, J. Li, T. Lu, Y. Liu, M. N. Lockrey, K. J. Weber, K. R. Catchpole, and T. P. White, *Interface passivation using ultrathin polymer–fullerene films for high-efficiency perovskite solar cells with negligible hysteresis*, Energy & Environmental Science **10**, 1792 (2017).

[318] H. Li, L. Tao, F. Huang, Q. Sun, X. Zhao, J. Han, Y. Shen, and M. Wang, *Enhancing efficiency of perovskite solar cells via surface passivation with graphene oxide interlayer*, ACS Applied Materials & Interfaces , acsami.7b10773 (2017).

[319] L. Wang, C. McCleese, A. Kovalsky, Y. Zhao, and C. Burda, *Femtosecond Time-Resolved Transient Absorption Spectroscopy of CH 3 NH 3 PbI 3 Perovskite Films: Evidence for Passivation Effect of PbI 2*, Journal of the American Chemical Society **136**, 12205 (2014).

[320] Q. Chen, H. Zhou, T.-b. Song, S. Luo, and Z. Hong, *Controllable self-induced passivation of hybrid lead iodide perovskites toward high performance solar cells Controllable self-induced passivation of hybrid lead iodide perovskites toward high performance solar cells*, Nano Letters **14**, 4158 (2014).

[321] T. Supasai, N. Rujisamphan, K. Ullrich, A. Chemseddine, T. Dittrich, T. Supasai, N. Rujisamphan, K. Ullrich, A. Chemseddine, and T. Dittrich, *Formation of a passivating CH3NH3PbI3 / PbI2 interface during moderate heating of CH3NH3PbI3 layers Formation of a passivating CH 3 NH 3 PbI 3 / PbI 2 interface during moderate*, **183906**, 2013 (2014).

[322] Y. C. Kim, N. J. Jeon, J. H. Noh, W. S. Yang, J. Seo, J. S. Yun, A. Ho-Baillie, S. Huang, M. A. Green, J. Seidel, T. K. Ahn, and S. I. Seok, *Beneficial Effects of PbI 2 Incorporated in Organo-Lead Halide Perovskite Solar Cells*, Advanced Energy Materials **6**, 1502104 (2016).

[323] Z. Ren, A. Ng, Q. Shen, H. C. Gokkaya, J. Wang, L. Yang, W.-K. Yiu, G. Bai, A. B. Djurišić, W. W.-f. Leung, J. Hao, W. K. Chan, and C. Surya, *Thermal Assisted Oxygen Annealing for High Efficiency Planar CH3NH3PbI3 Perovskite Solar Cells*, Scientific Reports **4**, 6752 (2015).

[324] H. Wei, Y. Fang, P. Mulligan, W. Chuirazzi, H.-H. Fang, C. Wang, B. R. Ecker, Y. Gao, M. A. Loi, L. Cao, and J. Huang, *Sensitive X-ray detectors made of methylammonium lead tribromide perovskite single crystals*, Nature Photonics **advance on** (2016).

[325] R. Brenes, D. Guo, A. Osherov, N. K. Noel, C. Eames, E. M. Hutter, S. K. Pathak, F. Niroui, R. H. Friend, M. S. Islam, H. J. Snaith, V. Bulović, T. J. Savenije, and S. D. Stranks, *Metal Halide Perovskite Polycrystalline Films Exhibiting Properties of Single Crystals*, Joule **1**, 155 (2017).

[326] X. Dong, H. Hu, B. Lin, J. Ding, and N. Yuan, *The effect of ALD-Zno layers on the formation of CH 3 NH 3 PbI 3 with different perovskite precursors and sintering*

temperatures, Chem. Commun. **50**, 14405 (2014).

[327] C. Y. Chang, K. T. Lee, W. K. Huang, H. Y. Siao, and Y. C. Chang, *High-Performance, Air-Stable, Low-Temperature Processed Semitransparent Perovskite Solar Cells Enabled by Atomic Layer Deposition*, Chemistry of Materials **27**, 5122 (2015).

[328] A. Hultqvist, K. Aitola, K. Sveinbjörnsson, Z. Saki, F. Larsson, T. Törndahl, E. Johansson, G. Boschloo, and M. Edoff, *Atomic Layer Deposition of Electron Selective SnOxand ZnO Films on Mixed Halide Perovskite: Compatibility and Performance*, ACS Applied Materials and Interfaces **9**, 29707 (2017).

[329] H. Si, Q. Liao, Z. Zhang, Y. Li, X. Yang, G. Zhang, Z. Kang, and Y. Zhang, *An innovative design of perovskite solar cells with Al2O3 inserting at ZnO/perovskite interface for improving the performance and stability*, Nano Energy **22**, 223 (2016).

[330] D. Koushik, W. J. H. Verhees, Y. Kuang, S. Veenstra, D. Zhang, M. A. Verheijen, M. Creatore, and R. E. I. Schropp, *High-efficiency humidity-stable planar perovskite solar cells based on atomic layer architecture*, Energy Environ. Sci. **10**, 91 (2017).

[331] D. Koushik, W. J. Verhees, D. Zhang, Y. Kuang, S. Veenstra, M. Creatore, and R. E. Schropp, *Atomic Layer Deposition Enabled Perovskite/PEDOT Solar Cells in a Regular n–i–p Architectural Design*, Advanced Materials Interfaces **4** (2017).

[332] M. Kot, C. Das, Z. Wang, K. Henkel, Z. Rouissi, K. Wojciechowski, H. J. Snaith, and D. Schmeisser, *Room-Temperature Atomic Layer Deposition of Al2O3: Impact on Efficiency, Stability and Surface Properties in Perovskite Solar Cells*, ChemSusChem **9**, 3401 (2016).

[333] G. W. P. Adhyaksa, L. W. Veldhuizen, Y. Kuang, S. Brittman, R. E. I. Schropp, and E. C. Garnett, *Carrier Diffusion Lengths in Hybrid Perovskites: Processing, Composition, Aging, and Surface Passivation Effects*, Chemistry of Materials **28**, 5259 (2016).

[334] X. Dong, X. Fang, M. Lv, B. Lin, S. Zhang, J. Ding, and N. Yuan, *Improvement of the humidity stability of organic–inorganic perovskite solar cells using ultrathin Al 2 O 3 layers prepared by atomic layer deposition*, Journal of Materials Chemistry A **3**, 5360 (2015).

[335] V. Zardetto, B. L. Williams, A. Perrotta, F. Di Giacomo, M. A. Verheijen, R. Andriessen, W. M. M. Kessels, and M. Creatore, *Atomic layer deposition for perovskite solar cells: research status, opportunities and challenges*, Sustainable Energy Fuels **1**, 30 (2017).

[336] F. Léonard, A. A. Talin, B. S. Swartzentruber, and S. T. Picraux, *Diameter-Dependent Electronic Transport Properties of Au-Catalyst/Ge-Nanowire Schottky Diodes*, **106805**, 1 (2009).

[337] O. Demichel, V. Calvo, A. Besson, P. Noé, B. Salem, N. Pauc, F. Oehler, P. Gentile, and N. Magnea, *Surface recombination velocity measurements of efficiently passivated gold-catalyzed silicon nanowires by a new optical method*, Nano Letters **10**, 2323 (2010).

[338] Y. Dan, K. Seo, K. Takei, J. H. Meza, A. Javey, and K. B. Crozier, *Dramatic reduction of surface recombination by in situ surface passivation of silicon nanowires*, Nano Letters **11**, 2527 (2011).

[339] H. J. Joyce, J. Wong-Leung, C. K. Yong, C. J. Docherty, S. Paiman, Q. Gao, H. H. Tan, C. Jagadish, J. Lloyd-Hughes, L. M. Herz, and M. B. Johnston, *Ultralow surface recombination velocity in InP nanowires probed by terahertz spectroscopy*, Nano Letters **12**, 5325 (2012).

[340] Y. Li, F. Qian, J. Xiang, and C. M. Lieber, *Nanowire electronic and optoelectronic devices*, Materials Today **9**, 18 (2006).

[341] E. C. Garnett, M. L. Brongersma, Y. Cui, and M. D. McGehee, *Nanowire Solar Cells*,

Annual Review of Materials Research **41**, 269 (2011).

[342] T. Wang, B. Daiber, J. M. Frost, S. Mann, E. Garnett, A. Walsh, and B. Ehrler, *Indirect to direct bandgap transition in methylammonium lead halide perovskite*, Energy Environ. Sci. **10**, 509 (2016).

[343] S. Chen, X. Wen, S. Huang, F. Huang, Y.-B. Cheng, M. Green, and A. Ho-Baillie, *Light Illumination Induced Photoluminescence Enhancement and Quenching in Lead Halide Perovskite*, Solar RRL **1**, 1600001 (2017).

[344] Y. Yang, Y. Yan, M. Yang, S. Choi, K. Zhu, J. M. Luther, and M. C. Beard, *Low surface recombination velocity in solution-grown CH3NH3PbBr3 perovskite single crystal*, Nature Communications **6**, 7961 (2015).

[345] B. Wu, H. T. Nguyen, Z. Ku, G. Han, D. Giovanni, N. Mathews, H. J. Fan, and T. C. Sum, *Discerning the Surface and Bulk Recombination Kinetics of Organic–Inorganic Halide Perovskite Single Crystals*, Advanced Energy Materials **6**, 1 (2016).

[346] Y. Yang, M. Yang, Z. Li, R. Crisp, K. Zhu, and M. C. Beard, *Comparison of Recombination Dynamics in CH3NH3PbBr3 and CH3NH3PbI3 Perovskite Films: Influence of Exciton Binding Energy*, Journal of Physical Chemistry Letters **6**, 4688 (2015).

[347] J. C. de Mello, H. F. Wittmann, and R. H. Friend, *An improved experimental determination of external photoluminescence quantum efficiency*, Advanced Materials **9**, 230 (1997).

[348] A. R. Johnson, S.-J. Lee, J. Klein, and J. Kanicki, *Absolute photoluminescence quantum efficiency measurement of light-emitting thin films*, Review of Scientific Instruments **78**, 096101 (2007).

[349] S. Leyre, E. Coutino-Gonzalez, J. J. Joos, J. Ryckaert, Y. Meuret, D. Poelman, P. F. Smet, G. Durinck, J. Hofkens, G. Deconinck, and P. Hanselaer, *Absolute determination of photoluminescence quantum efficiency using an integrating sphere setup*, Review of Scientific Instruments **85**, 123115 (2014).

[350] W. Yang, Y. Yao, and C.-Q. Wu, *Mechanism of charge recombination in meso-structured organic-inorganic hybrid perovskite solar cells: A macroscopic perspective*, Journal of Applied Physics **117**, 155504 (2015).

[351] H. C. Kwon, A. Kim, H. Lee, D. Lee, S. Jeong, and J. Moon, *Parallelized Nanopillar Perovskites for Semitransparent Solar Cells Using an Anodized Aluminum Oxide Scaffold*, Advanced Energy Materials **6**, 1 (2016).

Summary

Optoelectronic devices have changed human life tremendously. Lighting, energy conversion and storage, communication and imaging are only a few examples of the applications that rely on optoelectronics. Further advances in low-cost, efficient devices requires investigating new materials and designs. Halide perovskites are a promising class of materials for incorporation in optoelectronics with higher efficiency and lower cost. The solution processability of these materials provides unique opportunities for simple nanostructure fabrication. Integration of micro and nanostructured perovskites will open up opportunities for approaching highly efficient devices. In this thesis we explore the fabrication and characterization of monocrystalline halide perovskite micro and nanostructures from solution.

Single crystals are the simplest form of a material and thus provide an ideal model system to study the most fundamental properties of the material in the absence of grain boundaries. Most previous work in this area involves perovskite single crystals grown using lengthy chemical methods, which yield large crystals that are far outside the range that is useful for most optoelectronic devices. In **Chapter 2** we present a method based on confining the solvent evaporation to fabricate thin halide perovskite single crystals that still have lateral dimensions large enough to make microscale devices. The single crystallinity is confirmed by electron backscatter diffraction (EBSD). Simple back-contacted $CH_3NH_3PbBr_3$ single crystal devices are made by deposition of the crystals on pre-fabricated metal electrodes. These devices show photovoltaic behaviour, and present a platform to study the fundamental properties of single crystal perovskites *in operando*.

To have perovskite optoelectronic devices commercially available their working principle and mechanisms, especially the ones that have led to performance instability and degradation, should be fully understood. One of the main causes presented for the short and long-term instability is ionic migration. Halide perovskites as ionic semiconductors are not only electronic but also ionic conductors. In **Chapter 3** we employ the back contacted $CH_3NH_3PbBr_3$ single crystal devices to study the ionic migration in the presence of applied electric field. The synchrotron-based nanoprobe X-ray fluorescence (nano-XRF) mapping with 250 nm resolution is used to quantify the changes of bromide distribution

at the nanoscale under applied electric fields. By systematically manipulating the halide concentration laterally with applied voltage bias we observe a quasi-reversible field-assisted halide migration. The photoluminescence mapping of the crystals under the same biasing conditions reveals the corresponding changes due to halide migration in the optical quality of $CH_3NH_3PbBr_3$ single crystals. Higher local bromide concentration is correlated with superior optoelectronic performance in $CH_3NH_3PbBr_3$, while regions with lower bromide concentration show decreased PL intensities. Density functional theory (DFT) computations indicate that bromide ions experience a low energy barrier to migration when the $CH_3NH_3^+$ ions are aligned in the presence of an electric field. In this scenario, the migration of halide ions is expected to change the local stoichiometry and therefore optoelectronic quality of perovskite devices during operation. This study clarifies that halide migration is a challenge that is intrinsic to the absorber and one that may play a determining role in the ultimate performance limits of perovskite devices.

In **Chapter 4** we present a method to fabricate free-standing solution-based vertical perovskite nanowires. In this method, the perovskite solution is extruded out of the pores of an anodized aluminum oxide (AAO) template by applying a pressure gradient. Free-standing nanowire arrays are formed upon subsequent evaporation of solvent during the annealing. Transmission electron microscopy (TEM) diffraction confirms the single crystallinity along the nanowire length. The photoluminescence quantum yields (PLQY) of single perovskite nanowires measured using an integrating sphere microscopy setup reach values up to ~29%. This technique can be generally used to form perovskite nanostructures with arbitrary dimensions and cross-sectional shape because the exit profile of the template is subsequently translated into the final semiconductor geometry. The concept of the fabrication process is very similar to macroscopic profile extrusion used extensively in the plastics industry, but now applied to a nanoscale optoelectronics material. The simplicity and fast speed of this technique make it as a promising approach for the large-scale industrial fabrication of optoelectronic devices based on perovskite nanostructured arrays.

Highly efficient perovskite nanostructured optoelectronic devices will depend critically on the density of defects at the surface and in the bulk. Passivating the surface defects with metal oxide such as Al_2O_3 has been introduced as a common strategy to decrease the charge carrier recombination at the surface of perovskites. In **Chapter 5** we study the surface passivation effect of alumina on perovskite nanowires embedded in AAO templates. A similar extrusion technique with shorter time of the applied pressure gradient is used to fill the AAO pores with perovskite nanowires. These perovskite/alumina nanowire arrays are used as a well-controlled platform to study the charge carrier dynamics and effect of surface passivation with alumina. A charge carrier lifetime of more than 20 ns is calculated from obtaining the recombination rate coefficients. We develop a model to relate the charge carrier lifetimes with the nanowire radii. Using this model, we extract a remarkably low surface recombination velocity (SRV) of 37.2±20 $cm.s^{-1}$ for the perovskite/alumina inter-

face which confirms the passivation role of alumina. Perovskite nanowire arrays in AAO templates have high potential for integration in highly efficient optoelectronic devices due to the ease of fabrication and excellent photophysical properties.
Overall, this thesis provides an insight into new solution-processed methods for fabrication of high quality single crystalline halide perovskite micro- and nanostructures. The fabricated perovskite microcrystals and nanowires are used as simple model systems to study the fundamental properties of halide perovskites by asking questions such as: Which ions are moving in halide perovskites under electric field? How does ionic migration affect the optoelectronic properties of halide perovskites? What is the potential for improving the surface properties of halide perovskites by alumina passivation? The answers to these questions expands our understanding of halide perovskite nanostructures and their potentials and limitations for incorporation into future optoelectronic devices.

Samenvatting

Opto-elektronische apparaten hebben de wereld om ons heen zeer ingrijpend beïnvloed. Verlichting, energieconversie en -opslag, communicatie en beeldvorming (imaging) zijn slechts enkele voorbeelden van toepassingen van de opto-elektronica. Om de vooruitgang in nieuwe, betaalbare, opto-elektronische apparaten met een hoge efficiëntie verder te stimuleren, is onderzoek naar nieuwe materialen en ontwerpen noodzakelijk. Halogenide perovskieten zijn een veelbelovende familie van materialen voor de incorporatie in opto-elektronische apparatuur, met hogere efficiëntie, en lagere kosten. De mogelijkheid om deze materialen te verwerken vanuit de oplossing biedt unieke mogelijkheden voor eenvoudige fabricatie van nanostructuren. Daarnaast zal integratie van micro- en nano-gestructureerde perovskieten mogelijkheden scheppen tot de fabricatie van zeer efficiënte apparaten met nieuwe toepassingen. Dit proefschrift richt zich op de fabricage, en karakterisatie, van deze monokristallijne, halogenide, perovskieten nanostructuren, gefabriceerd vanuit de oplossing.

Monokristallen zijn de meest eenvoudige soort materiaal, en zijn daarom bij uitstek geschikt om als modelsysteem te dienen voor het bestuderen van fundamentele eigenschappen van het materiaal, zonder effecten van korrelgrenzen (grain boundaries) te ondervinden. Het meeste voorafgaande onderzoek op dit onderwerp heeft zich gericht op monokristalperovskieten, die volgens lange (en vaak gecompliceerde) chemische methodes zijn gesynthetiseerd, waarbij lange kristalstructuren ontstaan, die niet bruikbaar zijn voor de voornaamste toepassingen in opto-elektronische apparaten. In **hoofdstuk 2** wordt een methode gepresenteerd waar door insluiten van vloeistofevaporatie dunne, halogenide, perovskieten monokristallen worden gefabriceerd, waarbij de laterale dimensies nog van een proportie zijn dat apparaten op microschaal kunnen worden verwezenlijkt. De monokristalliniteit wordt bevestigd met de elektronterugstrooidiffractietechniek (electron back-scatter diffraction, EBSD). Eenvoudige 'back-contact' zonnecellen op basis van $CH_3NH_3PbBr_3$ monokristallen zijn gemaakt door middel van depositie van deze kristallen op een netwerk van voorgefabriceerde metalen elektroden. Deze zonnecellen verdienen de naam, doordat zij fotovoltaïsch gedrag vertonen, en bieden daarmee een platform

voor onderzoek naar de fundamentele eigenschappen van monokristallijne perovskieten, *in operando*.
Om de commercialisatie van opto-elektronische apparaten van perovskiet te realiseren, moeten de werkingsprincipes -en mechanismen volledig worden begrepen, met inbegrip van de stabiliteit- en degradatieprocessen, als grootste invloeden op de efficiëntie, en prestaties over tijd, van deze apparaten. Ionenmigratie is een van de voornaamste oorzaken voor korte- en lange termijn instabiliteit. Halogenide perovskieten zijn zowel elektronische -en ionische geleiders, als ionische halfgeleiders. In **hoofdstuk 3** worden de 'back-contact' $CH_3NH_3PbBr_3$ monokristallen apparaten gebruikt om ionenmigratie te bestuderen onder invloed van een aangebracht elektrisch veld. Nanosonde X-ray fluorescentie metingen, gedaan in een synchrotron, worden gebruikt om een afbeelding met een resolutie van 250 nm te realiseren, om de veranderingen in bromidedistributie op de nanoschaal in kaart te brengen, onder invloed van een aangebracht elektrisch veld. Door systematisch de halogenideconcentratie lateraal aan te passen, door middel van een toegepaste voorspanning, wordt een quasi-reversibele, halogenide migratie gerealiseerd. De fotoluminescentie -afbeelding van de kristallen onder dezelfde toegepaste voorspanning toont de overeenstemmende veranderingen in de optische kwaliteit van de $CH_3NH_3PbBr_3$ monokristallen, ten gevolge van de halogenide migratie. Een hogere, plaatselijke, concentratie van bromide is gecorreleerd met superieure opto-elektronische prestaties, terwijl regio's met lagere bromide concentraties verlaagde fotoluminescentie-intensiteiten vertonen. Dichtheidsfunctionaaltheorieberekeningen (density function theory, DFT) bepalen dat bromide-ionen een lage energiebarriére ondervinden voor migratie, wanneer de $CH_3NH_3^+$ ionen worden gealigneerd door aanbrenging van een elektrisch veld. In dit scenario is de verwachting dat de migratie van halogenide ionen verandert door de plaatselijke stoichiometrie, en daarbij de opto-elektronische kwaliteit van de perovskieten apparaten tijdens gebruik. Deze studie verduidelijkt dat de halogenidemigratie een uitdaging is, die intrinsiek is aan het absorberend materiaal, en een bepalende rol kan spelen in de uiteindelijke prestatielimieten van perovskieten apparaten.
In **hoofdstuk 4** wordt een methode gepresenteerd om perovskieten verticaalvrijstaande nanodraden te fabriceren, vanuit de oplossingsfase. In deze methode worden de perovskieten in oplossingsfase uit een sjabloon met geanodiseerde aluminiumoxide (AAO) poriën geëxtrudeerd, door toepassing van een drukgradiënt. Reeksen van vrijstaande nanodraden worden gevormd door herhaaldelijke evaporatie van de oplossing, tijdens thermisch gloeien. Transmissie-elektronenmicroscopiediffractie bevestigt de monokristalliniteit van de nanodraden over hun gehele lengte. De fotoluminescentiekwantumopbrengsten (photoluminescence quantum yields, PLQY) van monokristallen perovskieten nanodraden, gemeten met behulp van een bol van Ulbricht microscoop, behalen waardes tot 29%. Deze techniek kan algemeen gebruikt worden om perovskieten nanostructuren te fabriceren met willekeurige dimensies en arbitraire transversale vorm, doordat het uitgangsprofiel van het sjabloon leidend is in de uiteindelijke geometrie van de vorm, die het halfgeleidermateriaal aanneemt. Het concept van

het fabricatieproces heeft grote gelijkenis met macroscopische sjabloonextrusie, zoals extensief gebruikt wordt in de plasticindustrie, maar nu toegepast op een opto-elektronisch materiaal op nanoschaal. De eenvoud en snelheid van deze methode maken dat het een veelbelovende methode is voor fabricatie van opto-elektronische apparaten op industriële schaal, gebaseerd op perovskieten nanogestructureerde reeksen en matrices.
Perovskieten nanogestructureerde opto-elektronische apparaten met hoge efficiëntie zijn sterk afhankelijk van de mate en dichtheid van deficiënties in het kristalrooster, zowel aan het oppervlak alsmede in de bulk van het materiaal. Oppervlaktepassivering met metaaloxide, zoals Al_2O_3, is een welbekende strategie om ladingdragerrecombinatie aan het oppervlak van perovskietstructuren tegen te gaan. In **hoofdstuk 5** wordt het oppervlaktepassiveringseffect van aluminiumoxide op perovskieten nanodraden, ingebed in AAO sjablonen, bestudeerd. Een vergelijkbare extrusietechniek wordt gebruikt om de AAO-poriën te vullen met perovskieten nanodraden, waarin voor een kortere tijd een drukgradiënt wordt aangebracht. Deze reeksen van perovskiet-aluminiumoxide nanodraden worden gebruikt als een podium om goed controleerbaar de ladingsdragerdynamiek te bestuderen, alsmede de uitwerking van oppervlaktepassivering met aluminiumoxide. Een ladingsdragerlevensduur van meer dan 20 ns wordt aangetoond, door middel van het verkrijgen van recombinatiesnelheidscoëfficienten, door fotoluminescentievervalsporen aan te passen aan een reactiesnelheidsmodel (rate equation model). De ladingsdragerlevensduur kan worden bepaald met behulp van informatie over de radii van de nanodraden, door middel van een zelfontwikkeld model. Met hetzelfde model wordt een opmerkelijk lage oppervlakterecombinatiesnelheid (surface recombination velocity, SRV) van 37.2 ±20cm/s bepaald voor het perovskiet-aluminiumoxide raakvlak, hetgeen de passiveringsrol van aluminiumoxide bevestigt. Perovskieten nanodraadreeksen in AAO sjablonen hebben een grote potentie voor integratie in opto-elektronische apparaten met hoge efficiëntie, doordat ze relatief makkelijk te fabriceren zijn, en excellente fotofysische eigenschappen vertonen.
Samenvattend biedt dit proefstuk inzicht in nieuwe technieken om uit de oplossingsfase verwerkte, hoge kwaliteit, monokristallijne, halogenide, perovskieten, micro- en nanostructuren te fabriceren. De gefabriceerde perovskieten microkristallen en nanodraden worden gebruikt als eenvoudige modelsystemen om de fundamentele eigenschappen van halogenide perovskieten te bestuderen, door vragen te stellen zoals: "Welke ionen migreren in halogenide perovskieten onder het aanbrengen van een elektrisch veld", "Hoe beïnvloedt ionenmigratie de opto-elektronische eigenschappen van halogenide perovskieten", en "Wat is de verbeterpotentie van oppervlakte-eigenschappen van halogenide perovskieten, met gebruik van aluminiumoxide-oppervlaktepassivering?"De antwoorden op deze vragen verbreden ons begrip van halogenide, perovskieten nanosctucturen, en de potenties en limitaties voor de incorporatie van deze materialen in toekomstige opto-elektronische apparaten.

List of publications

This thesis is based on the following publications:

- *Growth and characterization of PDMS-stamped halide perovskite single microcrystals*
  P. Khoram, S. Brittman, W.I. Dzik, J.N.H. Reek, E.C. Garnett
  J. Phys. Chem. C, 2016, 120 (12), 6475. **(Chapter 2)**

- *Direct observation of halide migration and its effect on the photoluminescence of methylammonium lead bromide perovskite single crystals*
  Y. Lou*, P. Khoram*, S. Brittman, Z. Zhu, B. Lai, S.P. Ong, E.C. Garnett, D. Fenning
  Adv. Mater., 2017, 29 (43), 1521. **(Chapter 3)**
  *equal contribution

- *Perovskite nanowire extrusion*
  S.Z. Oener*, P. Khoram*, S. Brittman, S.A. Mann, Q. Zhang, Z. Fan, S.W. Boettcher, E.C. Garnett
  Nano Lett., 2017, 17 (11), 6557. **(Chapter 4)**
  *equal contribution

- *Charge carrier dynamics at the perovskite/alumina interface*
  P. Khoram, S.Z. Oener, E.C. Garnett
  (in preparation) **(Chapter 5)**

Other publications by the author:

- *Organic ternary solar cells: A review*
  T. Ameri, P. Khoram, J. Min, C.J. Brabec
  Adv. Mater., 2013, 25 (31), 1521.

- *Morphology analysis of near IR sensitized polymer/fullerene organic solar cells by implementing low bandgap heteroanalogue C-/Si-PCPDTBT*
  T. Ameri, P. Khoram, T. Heumuller, D. Baran, F. Machui, A. Troeger, V. Sgobba, D.M. Guldi, M. Halik, S. Rathgeber, U. Scherf, C.J. Brabec
  J. Mater. Chem. A., 2014, 2 (45), 19461.

Acknowledgements

It was more than four years ago when I put my first step into Amolf, a green building which became my second home during the last years. At that moment I could not imagine the great adventure I was going to have ahead, which one of its results is this thesis. The significant impact of these years in my life is beyond this book, and here I would like to express my gratitude to all of those who directly and indirectly have contributed.

First of all, I would like to thank my supervisor, Erik Garnett, for giving me the opportunity to start this journey and do my PhD in his group. Erik is a great scientist that teaches his knowledge unconditionally to his students. He showed me that not only a good and truthful science matters, but also being creative is necessary to do successful research. Having a supervisor who can not be convinced easily taught me how to become truly persistent, as himself is. Erik, I am grateful for the invaluable support and feedbacks you provided, and your openness for discussing anything. I learned from you to be stubborn in research, not to give up and get disappointed by the failures too soon, and to look for a clever and creative solution to the challenges on our way. Then I would like to acknowledge the support from my co-promoter Albert Polman, thank you for providing a collaborative culture and supportive atmosphere not only at LMPV and nanophotonic department, but also for the whole Amolf.

A couple of months after I started at Amolf, a postdoc researcher joined our group whose presence changed my vision and ultimate goal entirely. Sarah, without you this work would not ended up as it is today, thank you for all the scientific knowledge and manners you taught me. Your humbleness showed me that it is not about who is doing the science, but the science itself. Your organized and calm way to approach the challenges, always stays as an example to me. I have very deep respect for you, and I learned much more from you than I can express here in a few lines.

Doing scientific work without cooperation and interaction of people is not possible. During my PhD I had the chance to do research with collaborators whom provided invaluable learning and team work opportunities. I would like to thank David Fenning and Grace Lou for the work that ended up as the third chapter of this thesis. David, thank you for giving insightful feedbacks and being supportive through the

project which did not seem easy at the beginning. Grace, thank you for the very active cooperation and all the useful discussions on this project. Sarah, also thank you for accepting to go and do the experiments in Argonne National Lab on behalf of me, despite the very short notice, when it turned out that it was impossible for me to go.
I would like to thank all the members of Nanoscale solar cells group for their contribution, and also for making a pleasant working atmosphere. Sebastian, thanks for the collaboration in the perovskite nanowire project. That was one of the most fun, and most efficient projects I have ever done. It would have not been possible to make the "pasta wires" without your creative contribution, and openly helping me. Sander, thanks for your training on integrating sphere setup, and all the insights to understand the theory behind. Also thanks for teaching me about directivity, escape probability and FDTD simulation. I did not continue on that project, but all I learned stayed useful. I would like to thank the members of our little perovskite team: Gede, Shanti, Haralds, Teo and Forrest, for all the discussions, meetings and projects. Niels, I would like to especially thank you for translating of the summary of this thesis to Dutch, and Julia thanks for re-checking it. Michiel, I always remember the first day that we started together and thank you for all the moments of fun and sports! And, thanks to the rest of current and former members of the group: Beniamino, Biplab, Eric, Harshal, Hongyu, Jia, Lai-Hung, Cristina, Mohamed, Jenny and Sven, for all the valuable discussions, and also fun moments.
This experimental work would have not been possible without the incredible and easy-to-reach support provided by the technicians. I would like to express my deep appreciation to all the support staff at Amolf. Henk-Jan, thank you for your wonderful graphic designs, including the first figure of this thesis and also the cover design for our paper. I'm also very grateful for your support during my writing phase (Also thanks Merel!) and your friendship which I hope it will continue. Marc, thank you for being the great technician of our group. Definitely without your always available support, none of us could do our research as smoothly and conveniently as we do today in the lab. Thanks for all the help with maintaining the dirty glovebox (and also all other equipment and chemicals), I still remember that night that you came at 12 a.m. for regenerating the glovebox! Dirk-Jan, thanks for your help with the schematics of my first and second papers. Jan, thanks for providing the electrical engineering support for our group. Thank you for training us on ESD, and helping with handling my very sensitive samples! Clyde, thanks for the fantastic facility support you provide. Your cheerful manner makes this building a better place to be. Hans, Dimitry, Andries and Bob, what you are doing at the nanocenter is simply amazing! Thanks for always coming up with a smart solution for fabricating complex structures, for keeping the clean room pleasant, and for patiently training and taking care of the equipments. Dion and Niels, thank you for your quick helps with my orders, which almost always happened to be last minute!
Our group is part of the program of Light management for Photovoltaics (LMPV). I would like to thank the group leaders: Albert Polman, Bruno Ehrler and Esther Alarcon Llado for organizing the meetings, symposia and outings, and also for the

high quality discussions and feedback. Thanks also to the LMPV group members, especially: Verena, Andrea, Mark Knight, Piero, Tianyi, Moritz, Benjamin (and especially thanks for the help in TCSPC setup), Lucie, Loreta, Christian, Nasim and Mark Aarts, for providing a collaborative atmosphere. Apart from LPMV, we are also part of nanophotonic department at Amolf, with weekly nanophotonic colloquia and poster sessions which provides an open and active atmosphere for learning, discussion and receiving feedbacks. I would like to thank the group leaders: Femius Koenderink, Ewold Verhagen and Said Rodriguez, and all the current and previous group members, especially: Sophie, Nick, Magda, Benjamin, Freek, Rick, Clara, Lutz, Annemarie, Kevin, Hugo, Isabelle, Ruslan, Christiaan, John, Juha, Robin, Giada, Nikhil, and Lorentzo. Thank you for making the working place pleasant, and all the good moments out of work.

Being at Amolf gave me the chance of having invaluable friendships which stays with me the rest of my life. My science girls: Agata, Cristina, Jenny and Giada, making our little gang was one of the best things happened to me in the past few years. I hope your company and friendship stays as a life lasting thing, and we repeat our adventurous travels and chillin home-stay nights together over and over again. Cristina, you are my first friend in Amsterdam, someone I know I can always count on her wisdom, and I was so lucky to share a lot of intimate moments with you. I am so happy you accepted to be my paranymph, thanks a lot! Tzeni, my dear neighbor, officemate, colleague and friend, I am so happy that I could have the chance of knowing you and sharing a lot of moments with you. Your golden heart shines wherever you go. Thanks for tolerating me on my talkative moods at the office, and for all the energetic chitchats and generous hugs. Also thank you for being my paranymph! Agata, you are one of those persons I always feel proud of having their friendship. Your strong character always spread good vibe around, thank you for your support and encouragement in hard moments. Giada, thanks for all the good moments and the hugs, exactly whenever needed!

In these years of living in Amsterdam a few people made it even more feels like home, with having the pleasure of talking in Persian and having the same roots. Parisa, you were the first Iranian I met here, and I am so happy that our friendship lasts so long. Thanks for all the long nights, good moments and your support in hard ones. Payam, I'm so grateful for having the opportunity to know you, and having a Mashhadi friend in this town! Thanks to you and Kim for having your door always open for me. Whenever something really bad happened in these years, I knew where is the first place I can go! I am also delighted that I had a few Iranian colleagues. Fatemeh and Abbas, thanks for your welcomeness and support when I just started. Nasim, thanks for all the scientific and non-scientific deep conversations I could have with you. I feel very lucky of having your friendship with such a positive vibe. It was a pleasant luxury for me to have a few of my cousins living in the same country: Sohrab, Marjaneh, Amirali and Saeideh, thank you for giving me the feeling of family during these years of being in the Netherlands.

I would like to thank all of those Amolfers whom we did not share much scientific collaborations, but the times we had together made the quality of these years much

higher: Federica, Yuval, Marco, Lukas, Hans, Iarik (also thanks for the preparation of precursors!), Augustin, Giorgio, Mathijs, Jacopo, Olga, Nicola, Mario, Michele, Giulia, Oleg, Aditya, Roberto (and also Katya), Alessandro, Simone, and Noreen. My office-mates: Amy, Jenny and (the regular visitor) Sven, thank you for the daily fun conversations, and for tolerating me during the writing phase, I know I was not very pleasant those days! I would also like to thank my climbing partners: Soraya and Maureen, thank you girls for those sportive and joyful moments. And my deep gratitude goes for my amazing friends, near or far, those who had a big impact on me, and were always cheerfully supportive: Juli, Alberto, Anastasia, Farbod, Farzaneh, Taees, Mona, Pardis, Parisa, and Negar.

When I was doing my master in Germany, I was very fortunate to have a very strong woman as my supervisor, someone who encouraged me to do PhD, and always remains as an example for me. Tayebeh, thank you for teaching me many things about science, research and life!

Moni and Laci, I am very thankful for your support and great hospitality, especially during our writing phase. It was tough but your kindness made it much easier to go through. Nagyon köszönöm szépen!

One of the most precious things that happened to me during these years was meeting you, Abel. Thank you for your endless care and love, for believing in me, and for all the fabulous moments that gave me energy to keep moving forward. Without you this work would have not been ended like this, and I am so excited to continue to the next adventurous steps with you!

Finally I would like to thank my beloved parents, Mitra and Masoud, and my little sister, Taraneh. Tari, I am so grateful for having the best sister in the world, someone I can always rely on, and the one who understands me the most! Thank you so much for the great support during my PhD, and especially for designing the cover of this thesis! Who and where I am today would not be in this way without the unconditional love and support of my parents. I would like to end this part by saying a few words to them:

مادر و پدر عزیزم، از حمایت ها و عشق بی دریغ شما بسیار سپاسگزارم. بدون شما هرگز به اینجا نمی رسیدم و تا همیشه برای داشتن شما قدردانم.

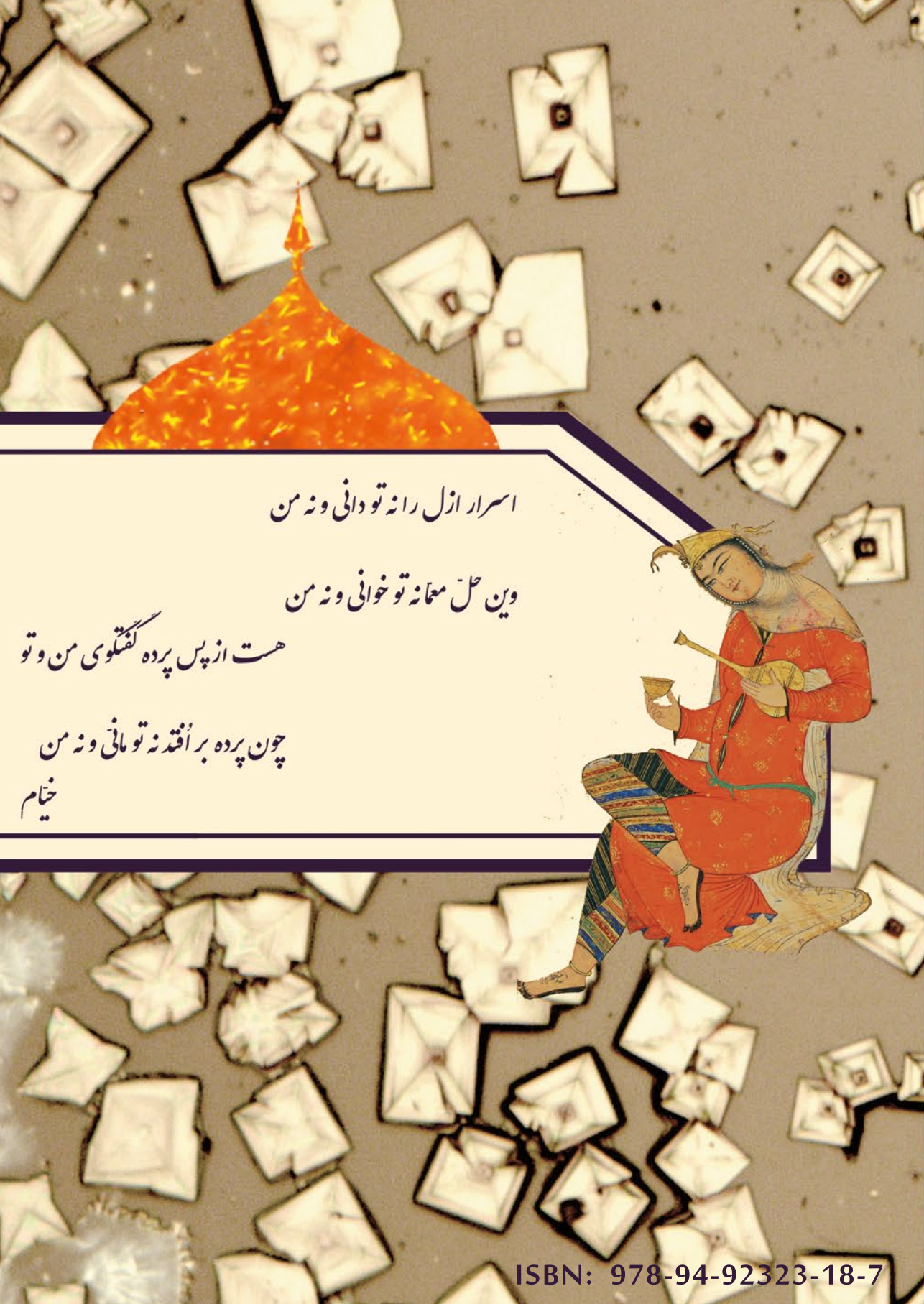

اسرار ازل را نه تو دانی و نه من

وین حلّ معما نه تو خوانی و نه من

هست از پس پرده گفتگوی من و تو

چون پرده بر افتد نه تو مانی و نه من

خیام

ISBN: 978-94-92323-18-7